AERODYNAMIC STABILITY CHARACTERISTICS OF THE APOLLO LAUNCH ESCAPE VEHICLE (LEV) WITH CANARD SURFACES DEPLOYED

by William C. Moseley, Jr., and Bass Redd

Manned Spacecraft Center
Houston, Texas

AERODYNAMIC STABILITY CHARACTERISTICS OF THE APOLLO LAUNCH ESCAPE VEHICLE (LEV) WITH CANARD SURFACES DEPLOYED

By William C. Moseley, Jr., and Bass Redd

Manned Spacecraft Center
Houston, Texas

NATIONAL AERONAUTICS AND SPACE ADMINISTRATION

ABSTRACT

A series of wind-tunnel studies was made to determine both static and dynamic stability characteristics of the Apollo launch escape vehicle, with canard surfaces in the deployed (open) position. This configuration is known as the post-abort vehicle. Results indicate that these canard surfaces are effective in producing a desired destabilizing increment in pitching moment. Positive damping was generally indicated.

CONTENTS

TABLES

FIGURES

AERODYNAMIC STABILITY CHARACTERISTICS OF

THE APOLLO LAUNCH ESCAPE VEHICLE (LEV)

WITH CANARD SURFACES DEPLOYED

By William C. Moseley, Jr., and Bass Redd
Manned Spacecraft Center

SUMMARY

A series of wind-tunnel studies was made to determine the stability characteristics, both static and dynamic, of the Apollo post-abort vehicle. Studies of the static stability characteristics were made at Mach numbers from 0.25 to 5.0, at angles of attack from 0° to 360° and at roll angles from 0° to -90°. Dynamic stability characteristics were determined at Mach numbers 0.50, 0.70, 0.80, 1.59, and 1.98 at a roll angle of 0° through the full 360° angle-of-attack range. Data obtained from the static stability studies indicated that the canard surfaces are effective in producing a desired destabilizing increment in pitching moment throughout the Mach number range tested. Data obtained from the dynamic stability studies indicated that the vehicle has positive damping for the Mach numbers investigated except for an angle-of-attack range from 145° to 190°. Magnitude and angle-of-attack range of the negative damping decreased with increasing Mach number and with decreasing oscillatory frequency.

INTRODUCTION

The effort of the United States to effect a manned landing on the surface of the moon has been designated Project Apollo. Responsibility for developing a vehicle capable of such a landing was given to the National Aeronautics and Space Administration. In order to determine vehicle flight characteristics within the atmosphere, an extensive wind-tunnel test program was established. (A detailed history of this program, and of the events leading to the establishment of the basic Apollo configurations, can be found in ref. 1.)

In general, the program is divided into several study areas, with each having as its individual purpose the examination of one major component, or component group, of the space-flight vehicle. These major components are the command module (CM), the launch escape vehicle (LEV), and the LEV with canard surfaces deployed. The aerodynamic stability characteristics of the Apollo CM can be found in reference 2. The aerodynamic stability characteristics of the LEV are discussed in reference 3.

In the event of a malfunction, the launch escape system will quickly transport the CM away from the launch boosters. While obtaining the necessary escape distance, flight of the LEV will be in a rocket-forward position. However, for proper deployment of the earth landing system, the flight attitude of the CM must be heat-shield- or blunt-face-forward. Simple separation of the launch escape system from the CM will not assure the heat-shield-forward attitude, since the CM alone has an apex-forward trim point.

In order to assure the necessary heat-shield-forward attitude, the LEV configuration is designed with deployable canard surfaces near the rocket nose. Deploying these canard surfaces after escape motor burnout provides a destabilizing moment which causes the LEV to rotate into the heat-shield-forward attitude. The canard surfaces also provide aerodynamic damping after the vehicle has attained this desired heat-shield-forward attitude. This damping reduces or eliminates the oscillation which results from the rotating maneuver.

The purpose of this paper is to present the results of a series of wind-tunnel tests made to determine the static and dynamic stability characteristics of the Apollo LEV, with canard surfaces in the deployed (open) position. This configuration is known as the post-abort vehicle.

Static stability characteristics were obtained at Mach numbers from 0.25 to 5.0, at angles of attack from 0° to 360°, and at roll angles from 0° to -90°. Dynamic stability characteristics were evaluated through the full 360° angle-of-attack range at a roll angle of 0° for subsonic Mach numbers of 0.5, 0.7, and 0.8 and for supersonic Mach numbers of 1.59 and 1.98.

The authors wish to acknowledge the assistance in the preparation of this paper of a writing team headed by Mr. Branch S. Phillips, a technical writer for the ITT-Federal Electric Corporation.

SYMBOLS

Many of the symbols defined below are illustrated in figure 1. The positive directions of the forces and moments, as well as the system of body axes, are also shown in figure 1.

C_A axial-force coefficient, $\dfrac{\text{axial force}}{q_\infty S}$

C_ℓ rolling-moment coefficient, $\dfrac{\text{rolling moment}}{q_\infty SD}$

$C_{m,a}$ pitching-moment coefficient about apex, $\dfrac{\text{pitching moment}}{q_\infty SD}$

$C_{m,c.g.}$ pitching-moment coefficient about center of gravity (c.g.), $\dfrac{\text{pitching moment}}{q_\infty SD}$, $\dfrac{X}{D} = -0.104$, $\dfrac{Z}{D} = 0$

$C_{m_q} + C_{m_{\dot{\alpha}}}$ damping-moment coefficient, $\dfrac{\partial C_m}{\partial \frac{qD}{2V}} + \dfrac{\partial C_m}{\partial \frac{\dot{\alpha}D}{2V}}$, rad^{-1}

C_N normal-force coefficient, $\dfrac{\text{normal force}}{q_\infty S}$

$C_{n,a}$ yawing-moment coefficient, $\dfrac{\text{yawing moment}}{q_\infty S D}$

C_Y side-force coefficient, $\dfrac{\text{lateral force}}{q_\infty S}$

D maximum body diameter (full scale), 154 in.

I moment of inertia, slug-ft^2

k reduced frequency parameter, $\dfrac{\omega D}{2V}$

M free-stream Mach number

q angular pitching velocity, rad/sec

q_∞ free-stream dynamic pressure, lb/ft^2

$\dfrac{q_\infty D^5}{I}$ scaling parameter, sec

R Reynolds number (based on maximum model diameter)

S maximum cross-sectional area perpendicular to body X-axis, ft^2

V free-stream velocity, ft/sec

$\dfrac{X}{D}$ longitudinal location of c.g. from theoretical command module apex

X, Y, Z body reference axes

$\dfrac{Z}{D}$ vertical location of c.g. from axis diameter of symmetry

α angle of attack, deg

β angle of sideslip, deg

θ	angular displacement, rad or deg
ϕ	angle of roll, deg
ω	circular frequency of oscillation, rad/sec

Subscripts:

a	command module apex
c.g.	center of gravity
m	model

Operators:

| $(\dot{\ })$ | time derivative |
| $(\ddot{\ })$ | second derivative (time) |

FACILITIES, MODELS, AND TESTS

Facilities

The tests were conducted in four separate wind-tunnel facilities. Static stability tests were made at facilities of the NASA Ames Aeronautical Laboratory and the Arnold Engineering Development Center (AEDC). The Ames 12-foot wind tunnel was used for subsonic evaluation of the post-abort vehicle. The Ames Unitary Plan Wind Tunnels (Ames UPWT) were used for Mach numbers from 0.70 to 3.4. Static stability tests at $M = 4$ and $M = 5$ were conducted at the AEDC tunnel A (AEDC-A). Dynamic tests were run at the North American Aviation Trisonic Wind Tunnel (NAA-TWT) and at the 8- by 6-foot supersonic wind tunnel of the NASA Lewis Research Laboratory (LeRC-SWT) at subsonic Mach numbers of 0.5, 0.7, and 0.8, and at supersonic Mach numbers of 1.59 and 1.98, respectively.

Table I is a listing of the wind-tunnel facilities used to test the post-abort vehicle models. The table indicates, for each tunnel, the Mach number range, the Reynolds number range, and the size of the test section.

Models and Tests

The scale of the models varied since the wind tunnels were of various sizes, and since it was recognized that the models should be as large as possible in order to minimize any scale effects. (General dimensions of the Apollo LEV with canard surfaces deployed are given in fig. 2.) Three models were used in this test series.

Model designations, scale, facilities, and test conditions for which each was tested are given in table II.

Different combinations of protuberances caused slight variations in the model configurations tested. These protuberances were attachments such as antennas, vents or any holes or recesses such as windows which would alter the otherwise smooth outer surface of the vehicle.

Initial static stability testing was accomplished in the Ames 12-foot pressure tunnel. A 0.105-scale model, sting-mounted from the CM in such a manner as to provide incremental coverage of attack angles between -10° and 320°, yielded six-component data. Runs were made at Mach numbers of 0.25, 0.50, and 0.70 and at roll angles of 0°, -30°, and -60°.

A second series of tests used the same 0.105-scale model but included special engineering changes for obtaining additional aerodynamic data. The model was re-worked to allow for dual-balance and heat-shield-forward mounting. The facility used was the Ames UPWT. (A typical installation is shown in fig. 3(a).) Mach numbers were transonic and supersonic and ranged from 0.70 to 3.4 at roll angles of 0°, -30°, and -60°. The angle-of-attack range, however, covered two quadrants from -15° to 155° and from 205° to 335°.

The third series of tests made in the Ames UPWT was quite similar to the second in all respects except protuberances and roll angles. Dual-balance, six-component data were taken for the same Mach number and angle-of-attack ranges. However, roll angles were taken to -90°, and the CM was reworked to simulate a modified umbilical fairing. The modification was mainly an increase in size, with the length increased by 0.7 inch, the height increased by 0.81 inch, and the width increased by 8.29 inches (full scale).

The fourth and last series of tests in the static stability group was made in the AEDC-A facility. A 0.045-scale model was used for this investigation. This model included a CM from which all protuberances had been removed. Mach numbers used were M = 4 and M = 5. Roll angles were taken to -90° and covered an angle-of-attack range between -50° and 235°.

Dynamic stability data were obtained in two series of tests, a subsonic series and a supersonic series. The subsonic test series was run in the NAA-TWT facility. This was an open-circuit, intermittent, blowdown wind tunnel with the capability of large variations in Reynolds number. In this facility the test-model oscillation frequency could be changed by varying the free-stream dynamic pressure q_∞. However, for this particular configuration, data were taken for only one free-stream dynamic pressure for each Mach number. The model was tested at Mach numbers of 0.50, 0.70, and 0.80. The supersonic phase was run in the LeRC-SWT facility. (This facility is an 8- by 6-foot, continuous-flow, closed-circuit, atmospheric wind tunnel.) Since this facility ran at an essentially constant, free-stream dynamic pressure q_∞ for a given Mach number, it was necessary to vary the model inertia to obtain a range of reduced frequency parameters. For the constant free-stream dynamic pressure condition, the scaling parameter reduces to $\frac{q_\infty D^5}{I}$. For simplicity, this parameter is given on each of the dynamic stability figures.

The 0.059-scale model was tested at Mach numbers of 1.59 and 1.98. Figure 3(b) shows the free-to-tumble dynamic stability model mounted in the LeRC-SWT.

TEST TECHNIQUES, DATA REDUCTION, AND ACCURACY

Test Techniques and Data Reduction

The test technique for static stability data was comprised of scale models of flight vehicle configurations mounted in various modes to provide $360°$ angle-of-attack coverage and roll angles of $0°$ to $-90°$ in selected wind tunnels which had the desired capabilities. For roll angles other than $0°$, the roll-angle data were simulated during the tests by varying the roll angle of the forward portion of the escape-rocket nose. This forward section included the canards in the deployed position. The rearward section of the model, including the rocket tower and CM with protuberances, remained in a roll attitude of $0°$ during measurement of the roll data. For roll angles other than $0°$ the model balance also remained in the $0°$ roll attitude, and the data were mathematically transferred to the rolled axis system.

For dynamic stability test data, a free-to-tumble scale model was mounted on a forked sting with a transverse rod which passed through the model at its center of gravity. The forked sting contained the equipment necessary to operate the model and obtain the required data. Two major design problems that became immediately apparent were (1) aerodynamic interference effects of the transverse-rod support and (2) friction introduced by the support system. Initially, the model was attached by a flexure link to a strain-gage beam inside the CM. The model was mounted on the transverse rod with ball bearings so that only the static pitching moment was transmitted through the strain-gage beam to the rod. All other aerodynamic forces and moments were transmitted from the model to the rod through the ball bearings. These ball bearings were bench-tested to determine the friction load, and it was found that the friction torque increased with the aerodynamic load. This friction value was used in the data reduction.

The output from the balance sources was recorded and reduced by a remote computer. This output was subject to real-time monitoring, where feasible, which afforded an opportunity to isolate and rerun questionable data. The data-reduction computer was programed to provide all standard aerodynamic force coefficients and moment coefficients about the body axes of the test models.

The dynamic motion of a body oscillating in a single plane about its center of gravity with a nonlinear restoring moment and viscous damping can be described by the following equation.

$$I\ddot{\theta} - \left[\left(C_{m_q} + C_{m_{\dot{\alpha}}}\right)\frac{q_{\infty}SD^2}{2V}\right]\dot{\theta} - C_m q_{\infty}SD = 0 \tag{1}$$

6

An angle-of-attack time history was then calculated by a digital computer using the dynamic stability derivatives $C_{m_q} + C_{m_{\dot{\alpha}}}$ and equation (1). The computed angle-of-attack time history was then compared to the angle-of-attack time history measured in the wind tunnel. As a result of this comparison, the $C_{m_q} + C_{m_{\dot{\alpha}}}$ curve was adjusted to achieve a closer match. After several trials, the value of $C_{m_q} + C_{m_{\dot{\alpha}}}$ as a function of angle of attack was closely approximated, as demonstrated by the quality of the match between the computed and measured time histories presented in figure 4. (More detailed discussions of the preceding technique, its mathematics, and its theory, can be found in refs. 1 and 3.)

Static Stability Accuracy

The balance and recording instruments were set up to provide maximum sensitivity within the capabilities of the instrumentation. The dynamic pressure could then be recorded within 2.839 lb/ft^2; the Mach number could be recorded within ± 0.01, or better; and the angle of attack could be recorded within $\pm 0.1°$, or better, for all angles.

Coefficient deviations were determined from load variations measured during the balance calibration check performed in the tunnels before testing. Deviations that could be expected in the presentation of the test results caused by measurement only were equal to, or better than, the deviations given in equation (2) as

$$
\left.
\begin{array}{lll}
C_N = \pm 0.0087 & C_{m,a} = \pm 0.0054 & C_{n,a} = \pm 0.0053 \\[2ex]
C_A = \pm 0.0087 & C_{m,c.g.} = \pm 0.0053 & C_{\ell} = \pm 0.0057 \\[2ex]
& C_Y = \pm 0.0105 &
\end{array}
\right\} \quad (2)
$$

Dynamic Stability Accuracy

The dynamic stability data presented in this report cannot be labeled with a discrete accuracy at discrete angles of attack. This is a result of the method used in obtaining and reducing the wind-tunnel data. The value of the dynamic stability derivative at any one angle directly influences the effective coefficients of all other angles. This is a result of the method employed in calculating the angle-of-attack time histories (eq. (1)).

An error in $C_{m_q} + C_{m_{\dot{\alpha}}}$ at an angle will introduce an error in the computed angular velocity which in turn will influence the effective $C_{m_q} + C_{m_{\dot{\alpha}}}$ at all other

angles. This occurs because the $C_{m_q} + C_{m_{\dot{\alpha}}}$ is multiplied by the angular velocity to obtain the damping force. Therefore, in this report, the accuracy will be demonstrated by how close the overall computed angle-of-attack time histories match the measured wind-tunnel angle-of-attack time histories (fig. 4). (The comparison shown in fig. 4 is considered typical of the match obtained with the measured and computed time histories.)

PRESENTATION OF RESULTS

The following table presents a summary of test data shown in the designated figures. These data describe the aerodynamic characteristics of the Apollo LEV with canard surfaces deployed (the post-abort vehicle).

Figure number	Mach number	Canard roll angle, ϕ	Type of data
5	0.25 to 0.70	0°	Static stability
6	0.5	-30° and -60°	Static stability
7	0.7 to 3.4	0°	Static stability
8	0.7 to 3.4	-30°	Static stability
9	0.7 to 3.4	-60°	Static stability
10	0.7 to 3.4	-90°	Static stability
11	4.0 to 5.0	0°	Static stability
12	5.0	0° to -90°	Static stability
13	0.25 to 5.0	0°	Comparison, with and without canards
14	5.0	0°	Schlieren photograph
15	0.5 to 1.98	0°	Comparison, pitching-moment coefficient for sting and transverse-rod mountings
16	0.5 to 1.98	0°	Dynamic stability

DISCUSSION

Static and dynamic stability data are used in computer programs to determine the operational sequence of, and to evaluate the performance of, the post-abort configuration for a range of initial conditions defined by the launch-vehicle flight envelope. Stability data, therefore, have been determined for a wide range of Mach numbers and angles of attack. Also, the effect of vehicle roll angle has been investigated. Data have been determined for roll angles in one quadrant ($\emptyset = 0°$ to $\emptyset = -90°$) and can be used to define data for the other quadrants with proper sign convention. (Cross plotting and interpolation will define data for any combination of Mach number M, angle of attack α, and angle of roll $\emptyset$ in the flight spectrum.)

Static Stability Characteristics

The static stability characteristics of the LEV with canard surfaces deployed are presented in figures 5, 7, and 11 for a canard roll angle $\emptyset = 0°$. Similar data at roll angles $\emptyset = -30°$, $\emptyset = -60°$, and $\emptyset = -90°$ are presented in figures 6, 8, 9, 10, and 12. These data cover a Mach number range from 0.25 to 5.0 and a large portion of the angle-of-attack range from 0° to 360°. The pitching-moment coefficient data (figs. 5, 7, and 11) indicate that the canard surfaces are effective in producing a destabilizing increment in pitching-moment coefficient throughout the Mach range tested. A comparison of the pitching-moment coefficient data with and without post-abort canard surfaces is given in figure 13 for Mach numbers from 0.25 to 5.0. These data indicate further that the canard surfaces provide a destabilizing increment of the pitching-moment coefficient. Although the pitching-moment coefficient data as presented show a range of neutral or slightly positive stability near $\alpha = 20°$ at supersonic speeds (M = 2.0 to M = 5.0), it must be remembered that the reference center of gravity for the data presented is the CM apex. This center of gravity was selected early in the Apollo wind-tunnel testing program as a data-reference center of gravity. The actual center of gravity for the Apollo post-abort configuration was rearward of the CM apex (toward the CM heat shield) and slightly below the axis of symmetry. The incremental effects were destabilizing when the center of gravity was moved rearward along the axis of symmetry and to a point below the axis.

The apparent decrease, with increasing Mach number, in effectiveness of the canard surfaces is caused primarily by an increase, with increasing Mach number, in the basic stability of the LEV. In addition, the destabilizing increment in pitching-moment coefficient is adversely affected by impingement of the shock wave on the lower surface of the CM (fig. 14).

Data are presented for the other five coefficients C_N, C_A, C_Y, $C_{n,a}$, and C_ℓ throughout the Mach number and angle-of-attack ranges tested. The primary effect of the addition of the canard surfaces to the LEV at $\emptyset = 0°$ is an increase in both the normal-force and axial-force coefficients. Data for the launch escape vehicle can be found in reference 3. The other three coefficients C_Y, $C_{n,a}$, and C_ℓ are essentially zero, as expected, for a roll angle $\emptyset = 0°$ (figs. 5, 7, and 11). As the roll angle is decreased from 0° toward -90°, there are progressive increases or decreases in the coefficient data, as expected.

Dynamic Stability Characteristics

The dynamic stability characteristics of the Apollo post-abort configuration were determined by a free-to-tumble technique, in which the model was mounted on a transverse-rod support system which passed through the center of gravity of the vehicle. Transverse-rod-support interference effects, as well as the support-bearing friction, are considered most critical in the determination of the dynamic stability characteristics. Static pitching-moment coefficient data were determined with the transverse-rod support system. A comparison of the pitching-moment coefficient data with data from the more conventional sting-support-system tests is given in figure 15. Although the agreement is not exceptionally good, the general trends and magnitudes are similar in most cases. The pitching-moment coefficient data determined with the transverse-rod support were used in the reduction of the dynamic stability data in order to account, as far as possible, for the interference effects. Calibrations of the tare damping were made to determine the input of the bearing friction and were used in the data reduction. (The dynamic stability derivatives are presented in fig. 16. The dashed-line portion of the curves in fig. 16(a) represents estimates obtained from an unpublished analytical method and are used, for the portion of the angle-of-attack range where test data were not obtained, to define the damping.) The data of figure 16(a) were used to predict successfully the dynamic motion of a full-scale Apollo vehicle. The data of figure 16 indicate that the vehicle has positive damping except for an angle-of-attack range from $\alpha = 145°$ to $\alpha = 190°$. The negative damping is most predominant in the subsonic Mach number range and tends to be reduced with an increase in Mach number and with a decrease in model oscillatory frequency.

CONCLUDING REMARKS

Wind-tunnel studies have been made to determine the static stability characteristics of the Apollo post-abort vehicle at Mach numbers from 0.25 to 5.0, at angles of attack from 0° to 360°, and at roll angles of 0° to -90°. Data for dynamic stability characteristics were taken at Mach numbers of 0.50, 0.70, 0.80, 1.59, and 1.98 for a roll angle of 0° through the full 360° angle-of-attack range. The static stability data indicate that the canard surfaces were effective in producing a destabilizing increment in pitching moment throughout the Mach number range tested. The dynamic stability data indicate that the vehicle has positive damping for the Mach numbers investigated, except for an angle-of-attack range from 145° to 190°. Increasing the Mach number or decreasing the model oscillatory frequency decreased the magnitude and the angle-of-attack range of the negative damping.

Manned Spacecraft Center
National Aeronautics and Space Administration
Houston, Texas, July 14, 1967
914-50-89-00-72

REFERENCES

1. Moseley, William C., Jr.; and Martino, Joseph C.: Apollo Wind Tunnel Testing Program — Historical Development of General Configurations. NASA TN D-3748, 1966.

2. Moseley, William C., Jr.; Moore, Robert H., Jr.; and Hughes, Jack E.: Stability Characteristics of the Apollo Command Module. NASA TN D-3890, 1967.

3. Moseley, William C., Jr.; and Hondros, James G.: Aerodynamic Stability Characteristics of the Apollo Launch Escape Vehicle. NASA TN D-3964, 1967.

TABLE I.- TEST FACILITIES AND CAPABILITIES

Test facility	Size of test section	Mach number range	Reynolds number range $\times 10^{-6}$/ft
Continuous tunnels			
Ames Unitary Plan Wind Tunnel (Ames UPWT)	8 by 7 ft	2.4 to 3.4	0.5 to 5
Ames Unitary Plan Wind Tunnel (Ames UPWT)	9 by 7 ft	1.5 to 2.6	1 to 7
Ames Unitary Plan Wind Tunnel (Ames UPWT)	11 by 11 ft	0.7 to 1.4	1 to 10
Ames 12-Foot Pressure Tunnel (Ames 12-ft)	12-ft diameter	0.0 to 0.95	0.5 to 9.0
Arnold Engineering Development Center, Tunnel A (AEDC-A)	40 by 40 in.	1.5 to 6.0	0.3 to 9
Lewis Research Center Supersonic Wind Tunnel (LeRC-SWT)	8 by 6 ft	0.4 to 2.1	2.5 to 5.05
Intermittent tunnel			
North American Aviation Trisonic Wind Tunnel (NAA-TWT)	7 by 7 ft	0.2 to 3.5	5 to 14

TABLE II.-- MODELS AND TEST RANGES

Model	Scale	Facility	Mach number range	Reynolds number range × 10^{-6} (a)	α range	Dynamic pressure, lb/ft^2
Force, static models						
FS-2	0.105	Ames 12-ft	0.25, 0.50, and 0.70	2.31 to 10.34	-10° to 320°	220, 500, and 400
		Ames UPWT	0.7 to 3.4	5.2 to 3.5	0° to 360°	425 and 540
		Ames UPWT	0.7 to 3.4	3.94 to 2.68	25° to 335°	425 and 540
				3.85 to 2.64		
FS-3	0.045	AEDC-A	1.5 to 6.0	1.73 to 4.37	0° to 360°	
Force, dynamic models						
FD-9	0.059	NAA-TWT	0.50	3.14 to 3.88	Free to tumble	640
			0.70			700
			0.80			830
		LeRC-SWT	1.59 and 1.98	3.57 to 3.88	Free to tumble	1180 and 1280

a Based on model maximum diameter.

13
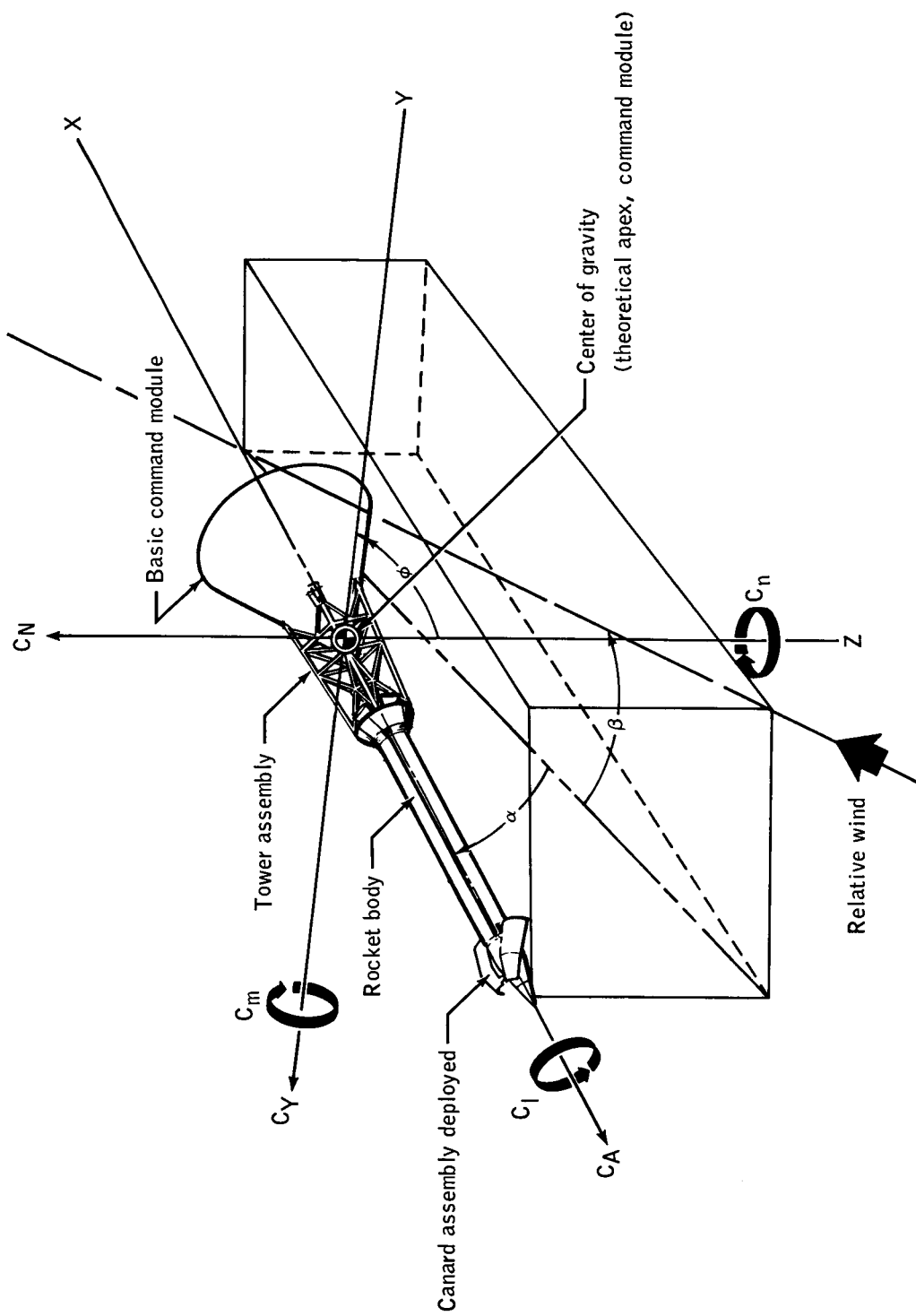
Figure 1.- Sketch showing system of body axes. Arrows indicate positive directions.
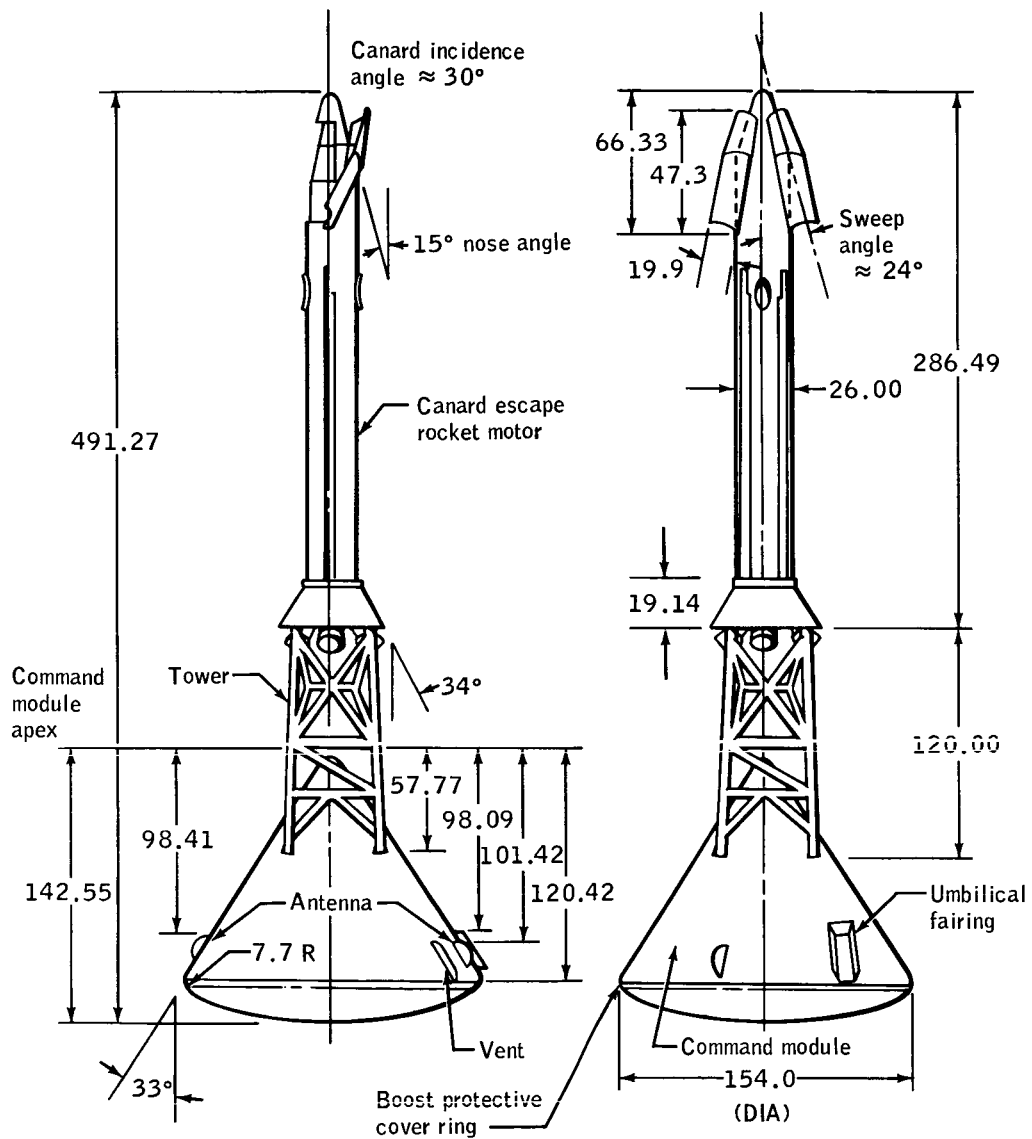
Figure 2. - Canard launch escape vehicle, showing full-scale dimensions in inches (drawing not to scale).

15
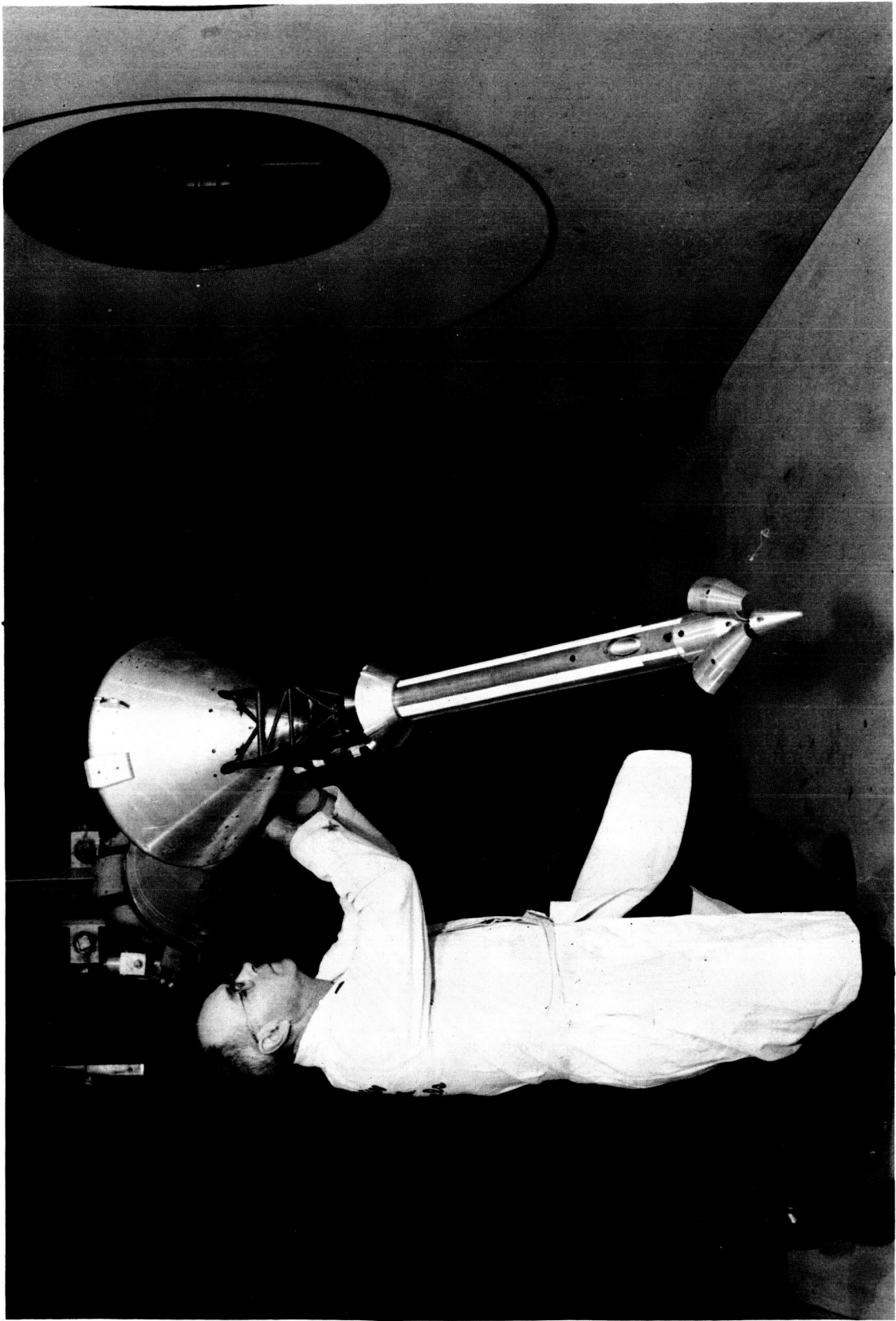
(a) Sting-mounted model, shown in the Ames UPWT.

Figure 3. – Photographs of test models.

(b) Free-to-tumble model, mounted in the LeRC-SWT.

Figure 3.- Concluded.
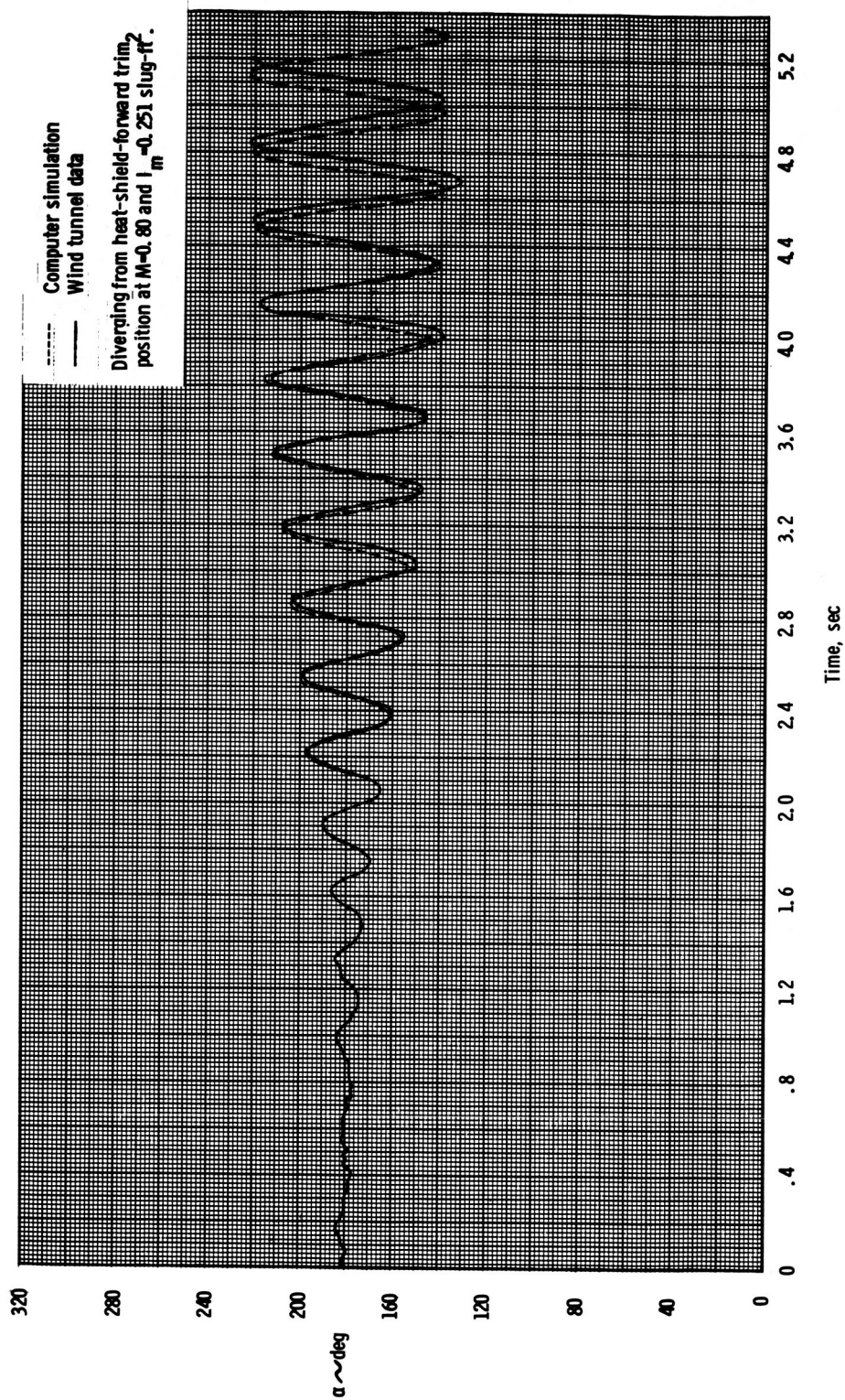
Figure 4. - Comparison of computer-simulated and wind-tunnel position-time histories.

18
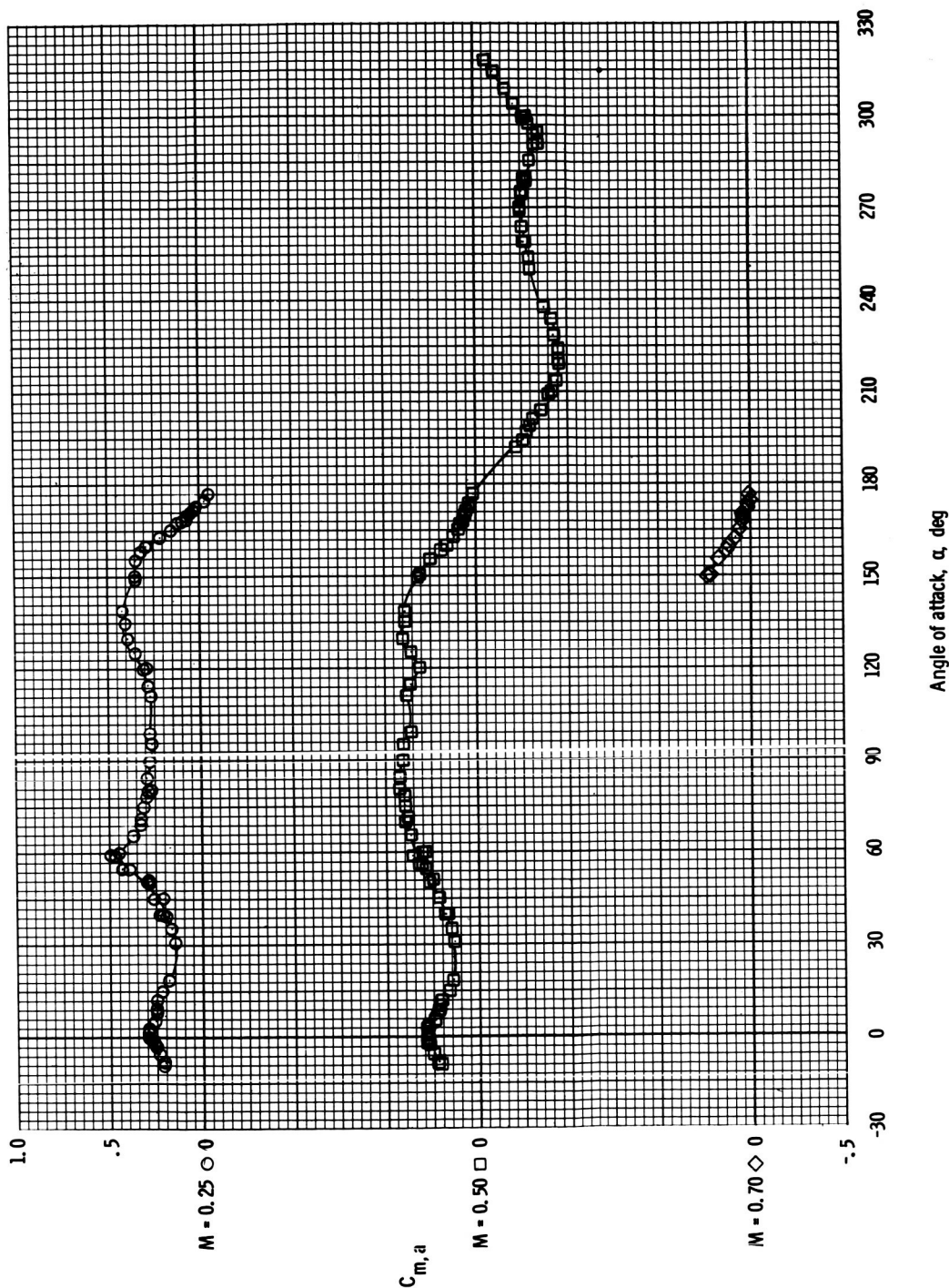
(a) Pitching-moment coefficient.

Figure 5. - Longitudinal aerodynamic characteristics of the Apollo launch escape vehicle with canard surfaces deployed, at M = 0.25, 0.50, and 0.70, with $\beta = 0°$.
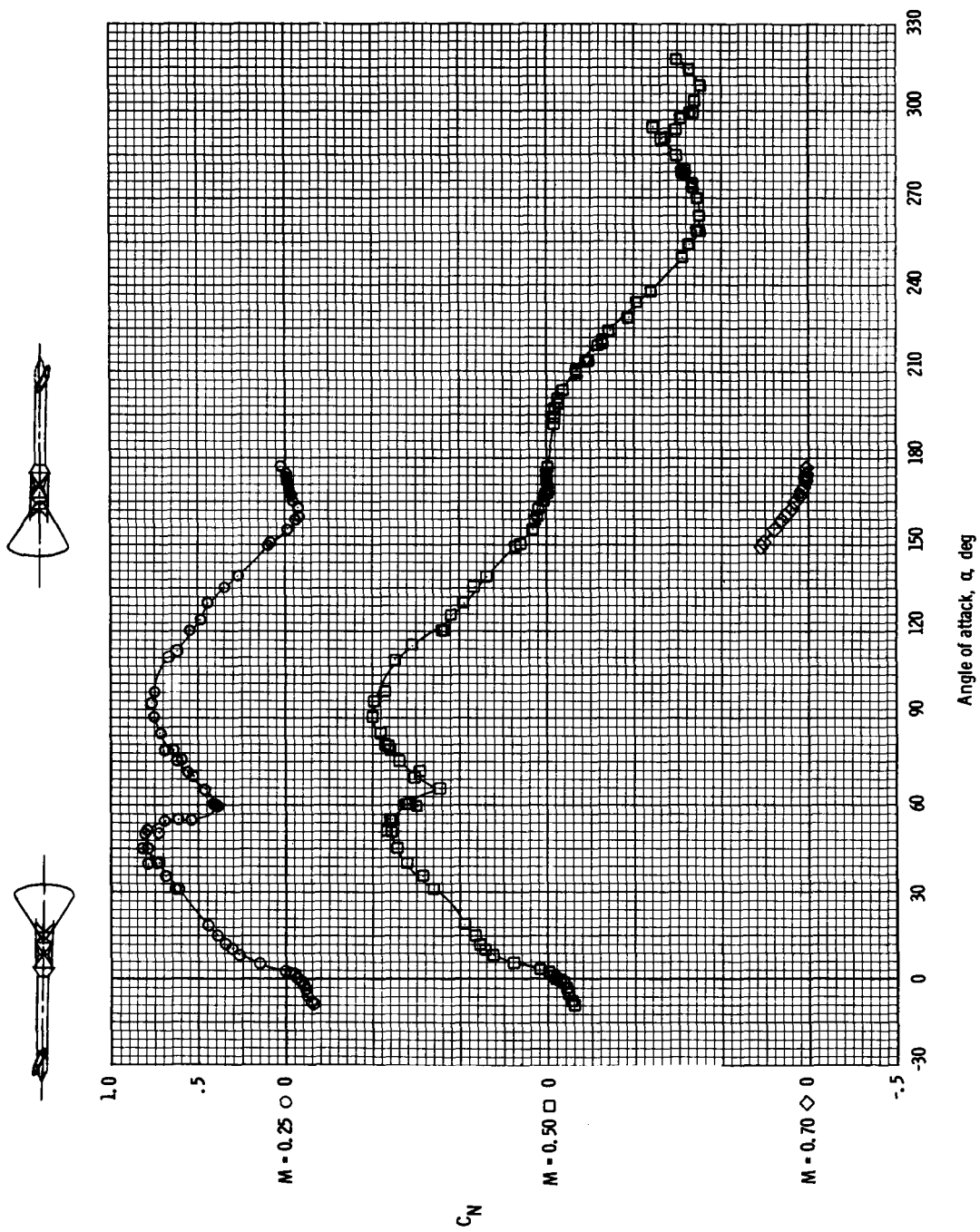
19

(b) Normal-force coefficient.

Figure 5. – Continued.

20
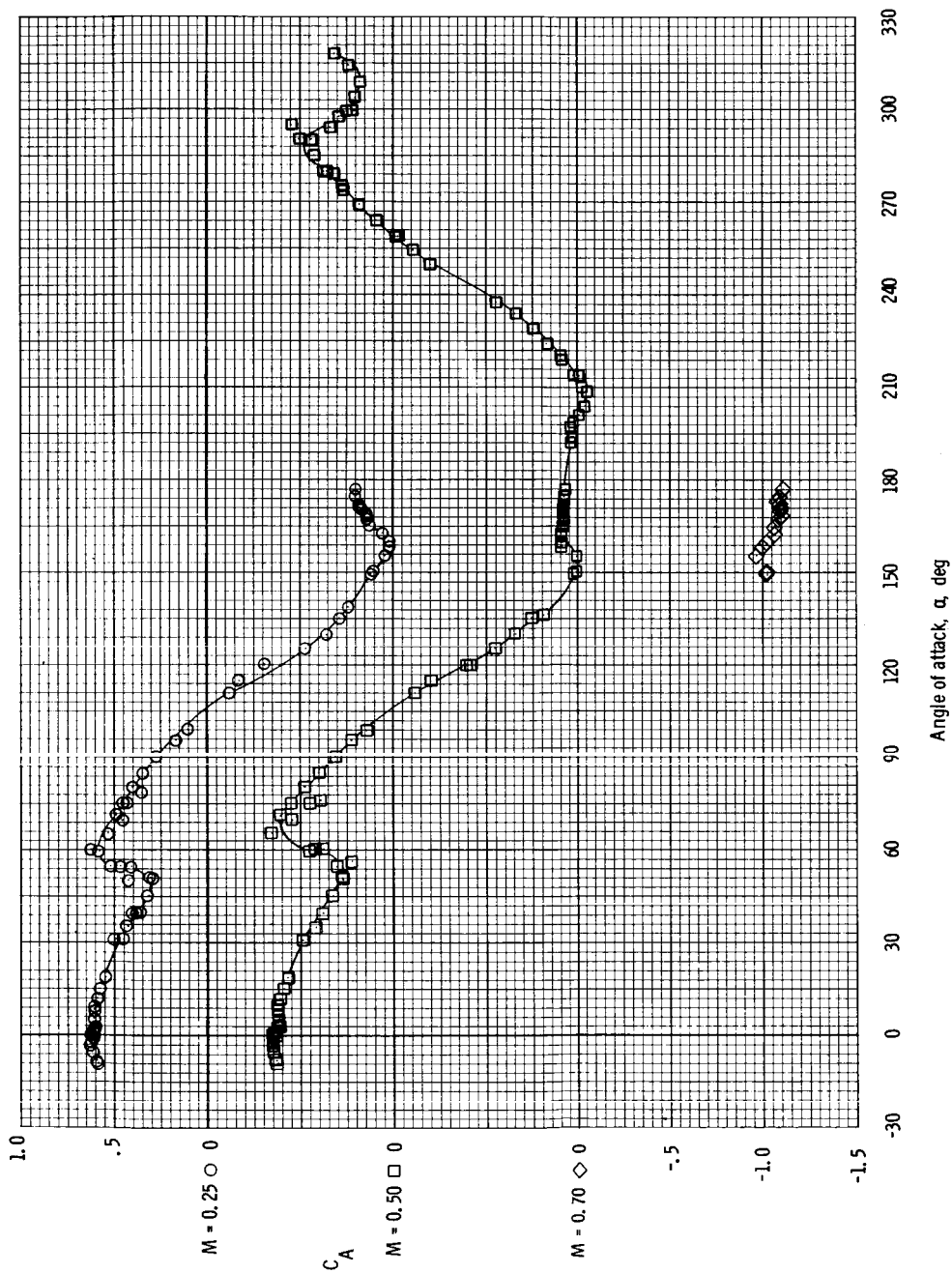
(c) Axial-force coefficient.

Figure 5. – Continued.

(d) Side-force coefficient.

Figure 5. - Continued.

Angle of attack, α, deg

$C_{n,a}$

(e) Yawing-moment coefficient.

Figure 5. - Continued.

23
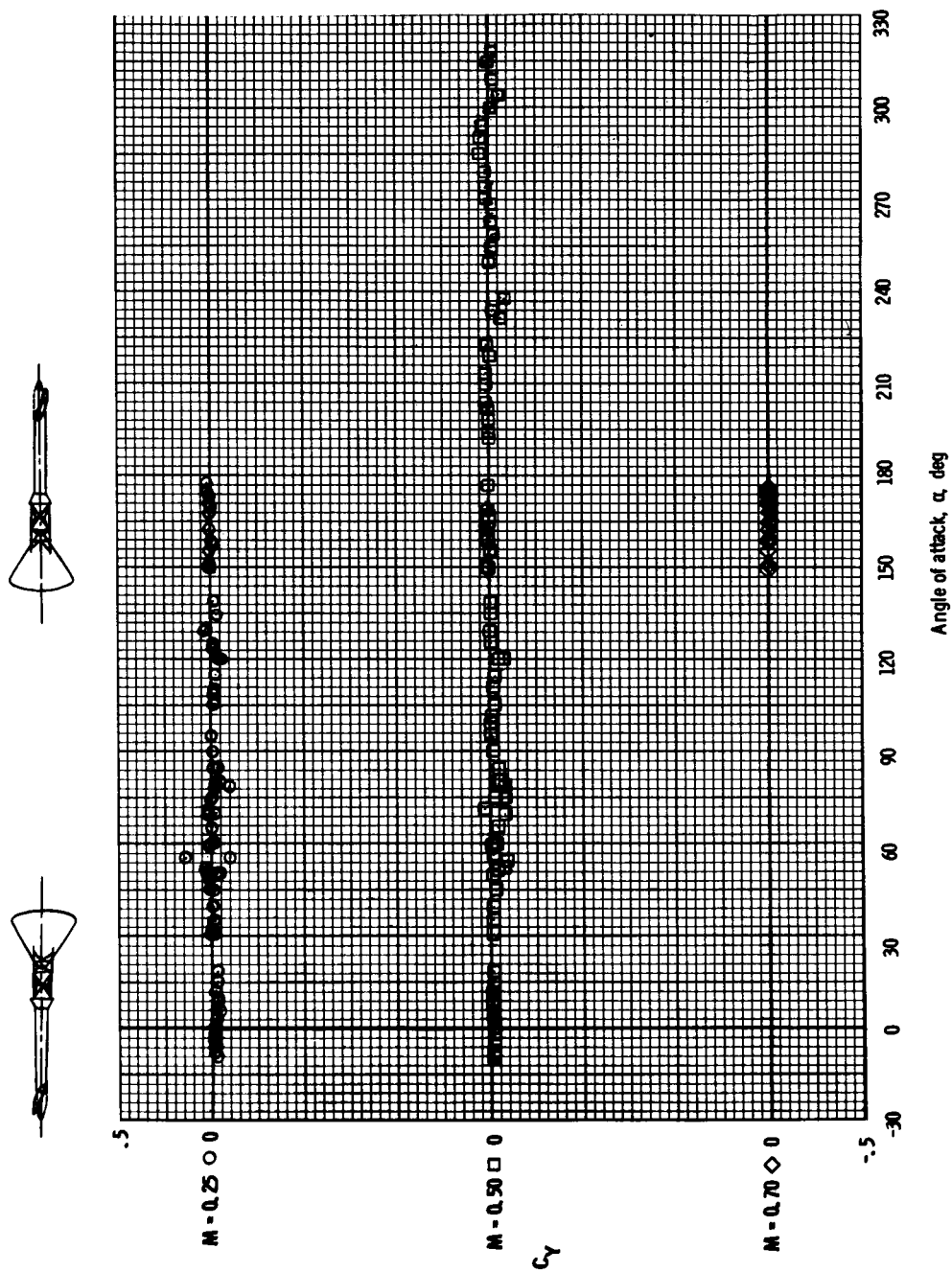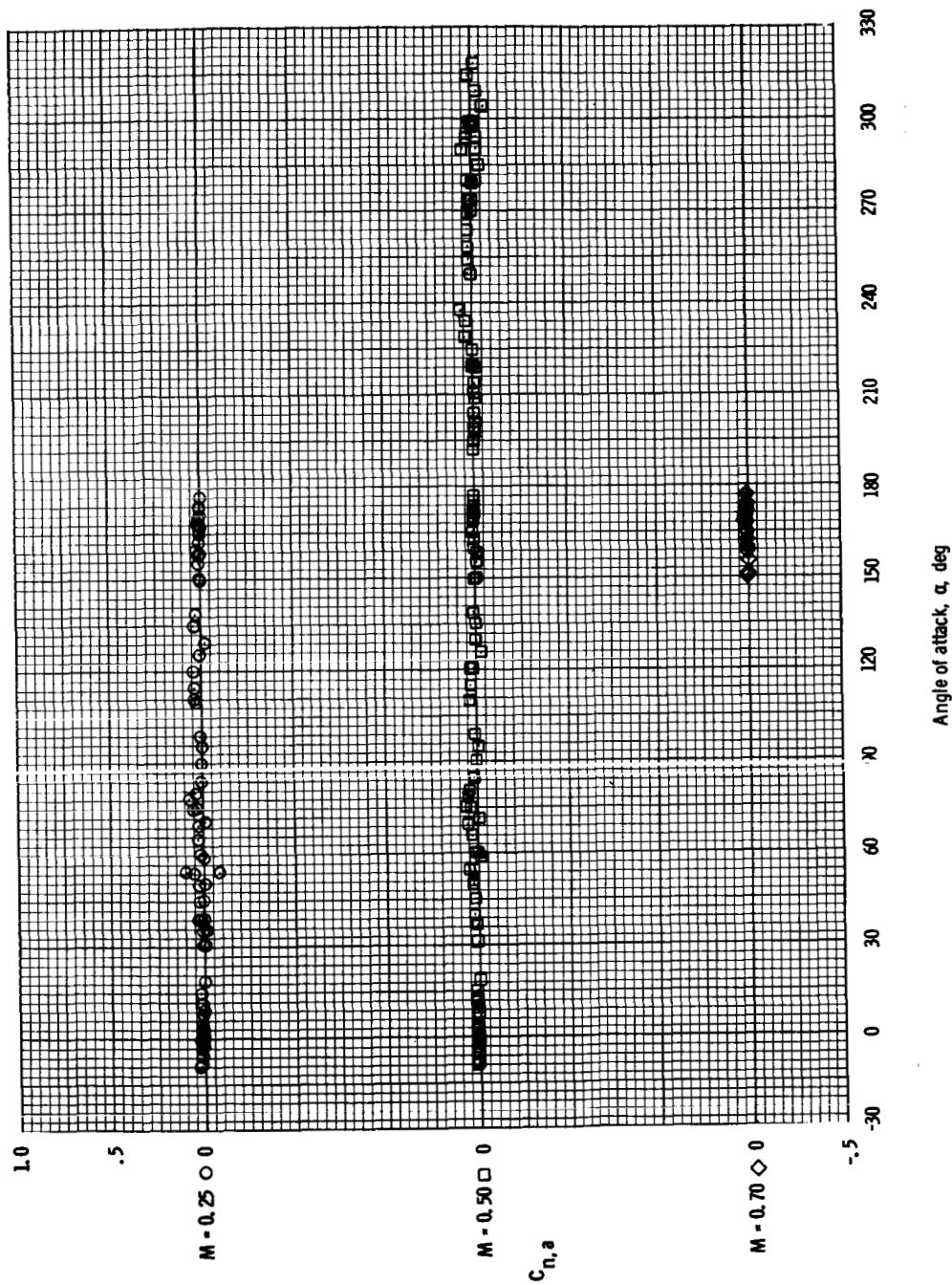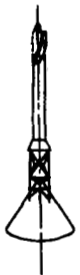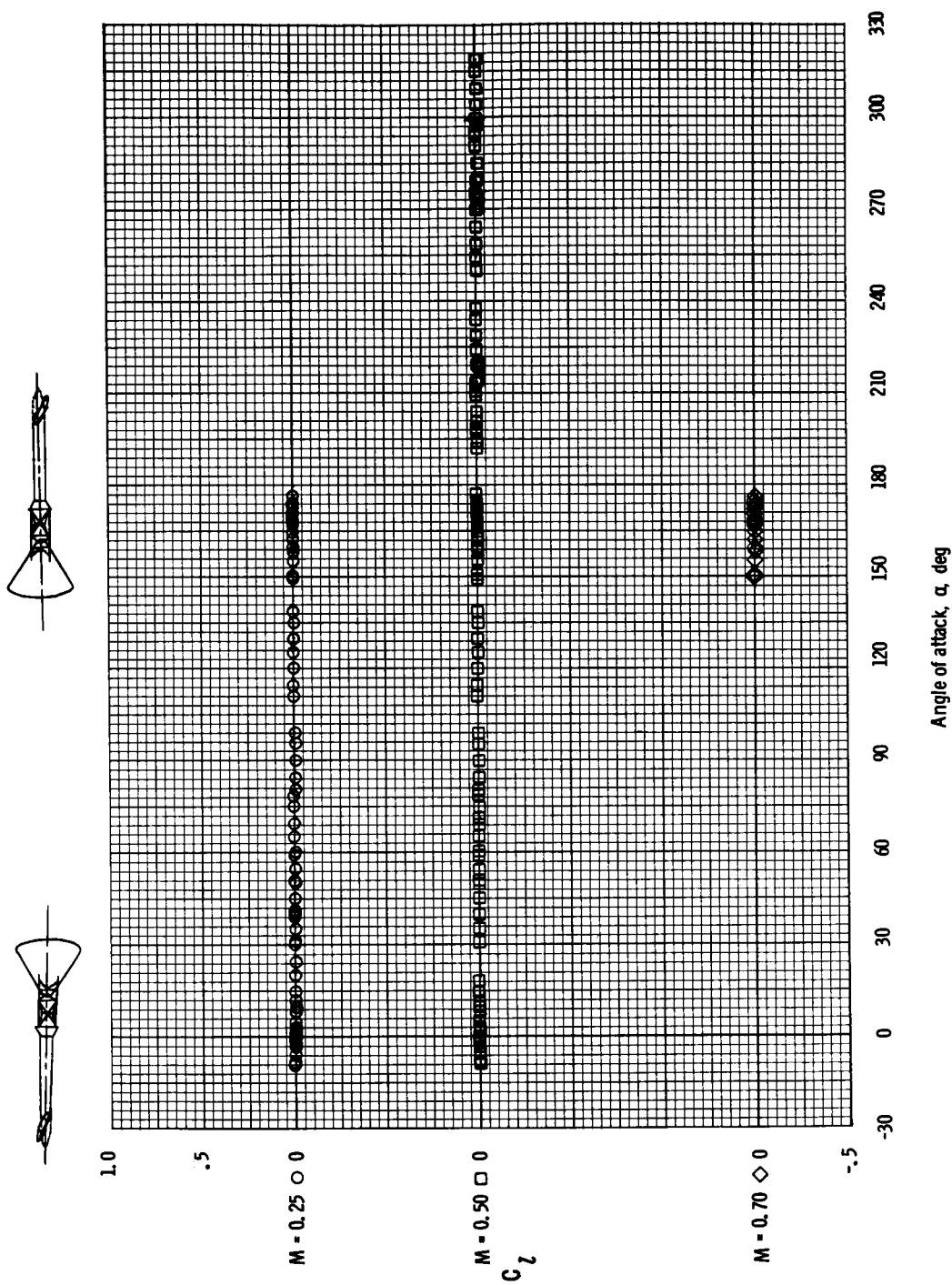
(f) Rolling-moment coeficient.

Figure 5. - Concluded.

24
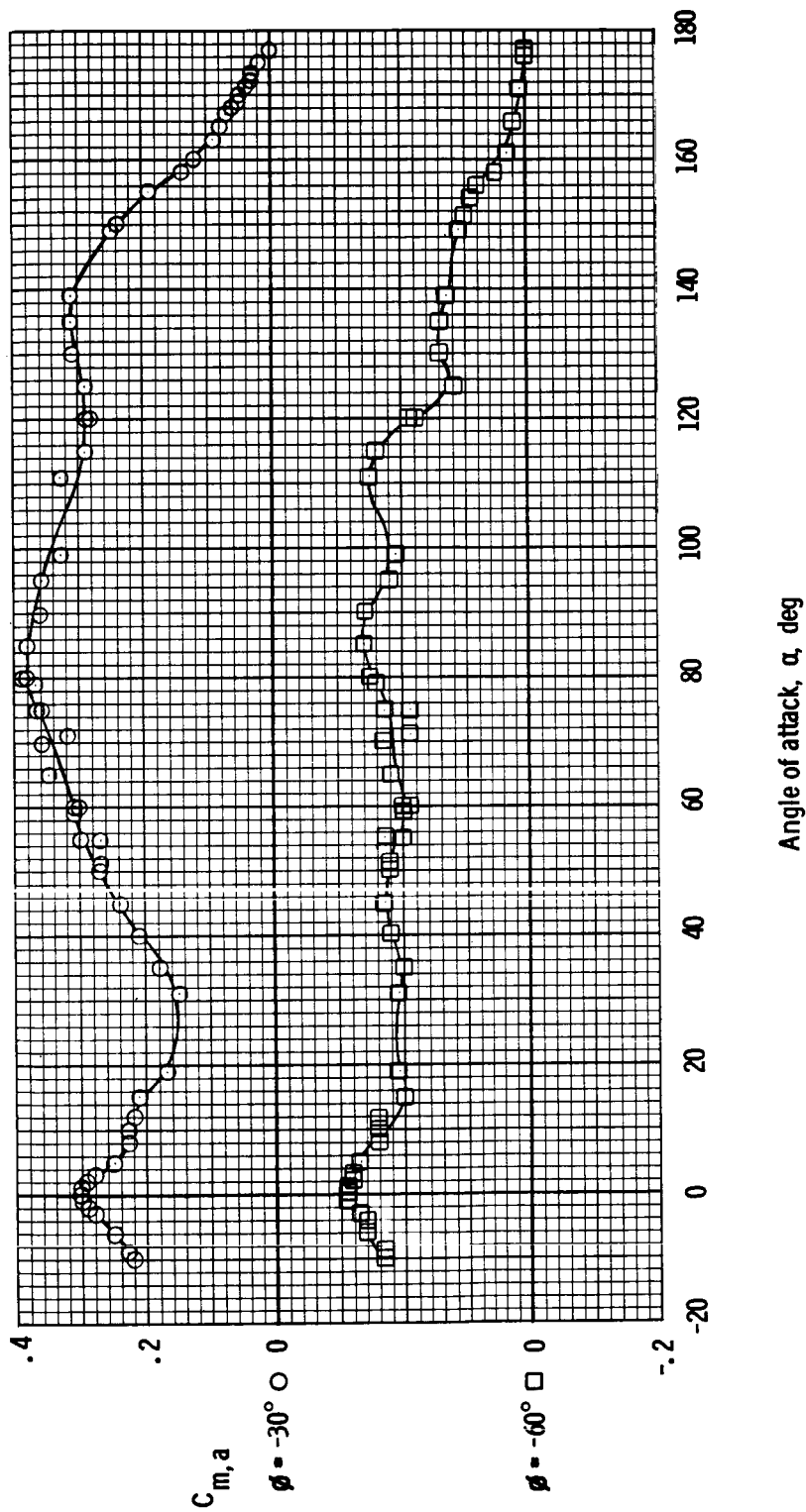
(a) Pitching-moment coefficient.

Figure 6. - Effect of canard roll angle ∅ on the longitudinal aerodynamic characteristics of the Apollo launch escape vehicle with canard surfaces deployed, at M = 0.50.
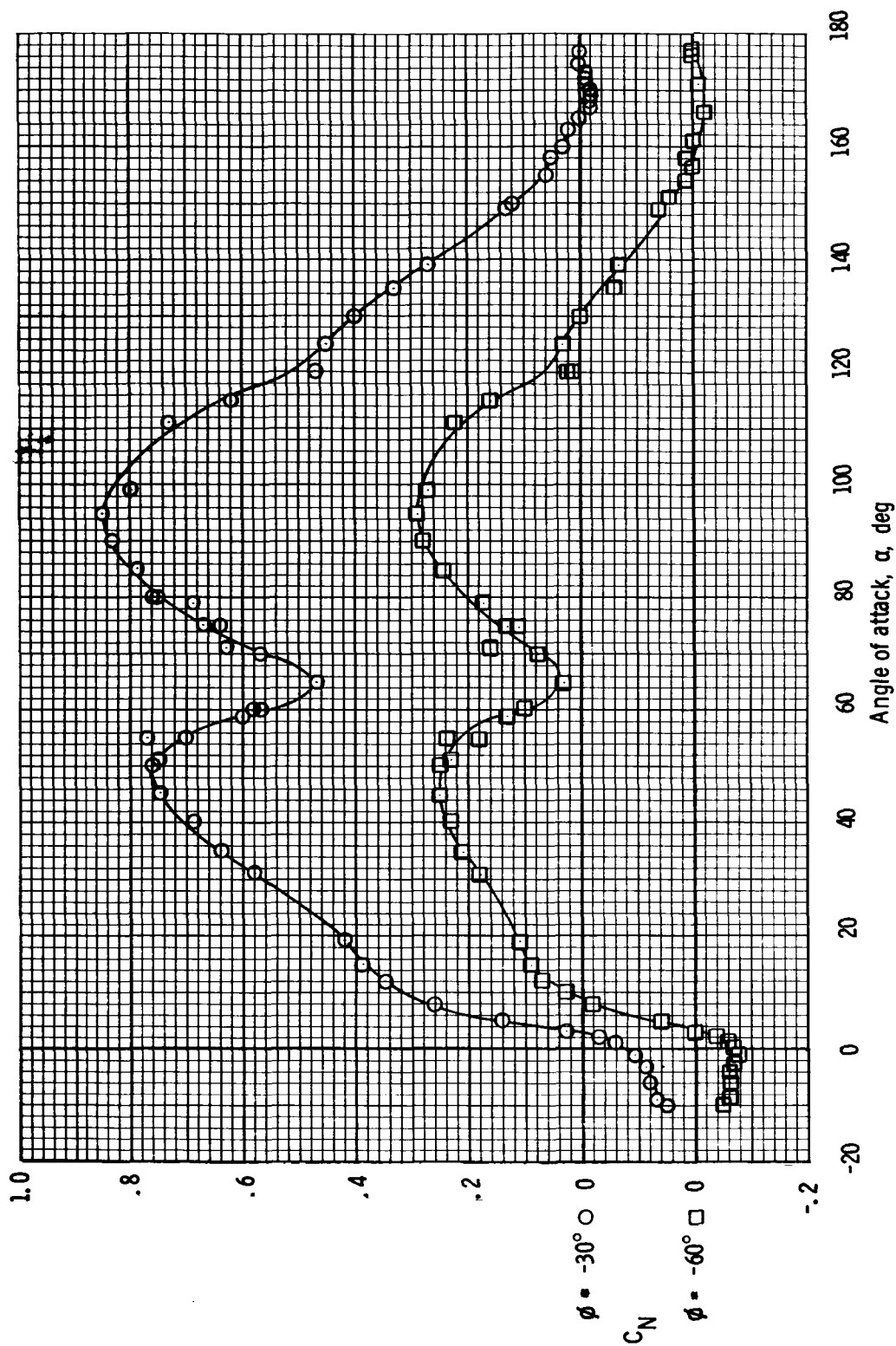
(b) Normal-force coefficient.
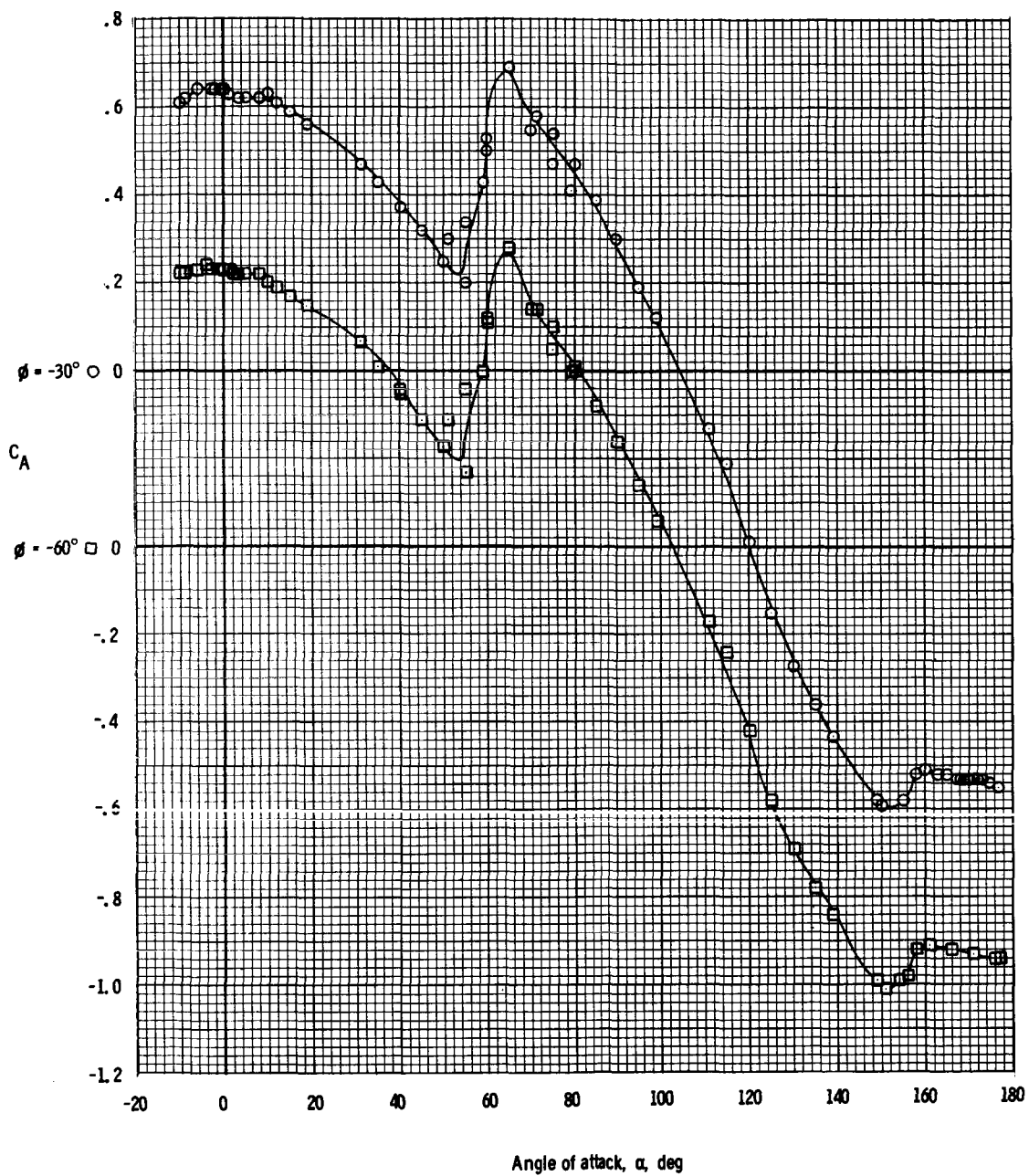
Figure 6. – Continued.

(c) Axial-force coefficient.
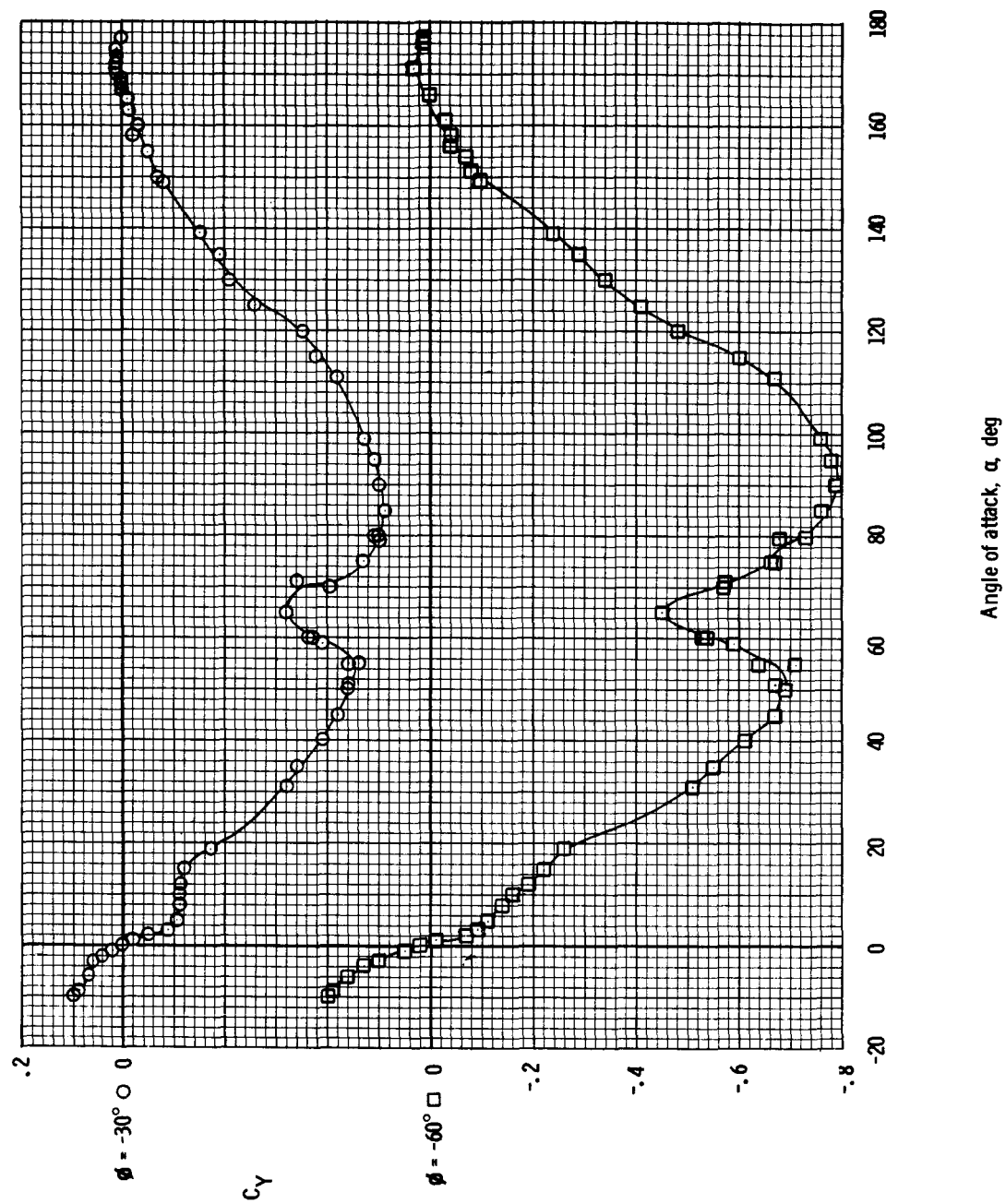
Figure 6. – Continued.

(d) Side-force coefficient.
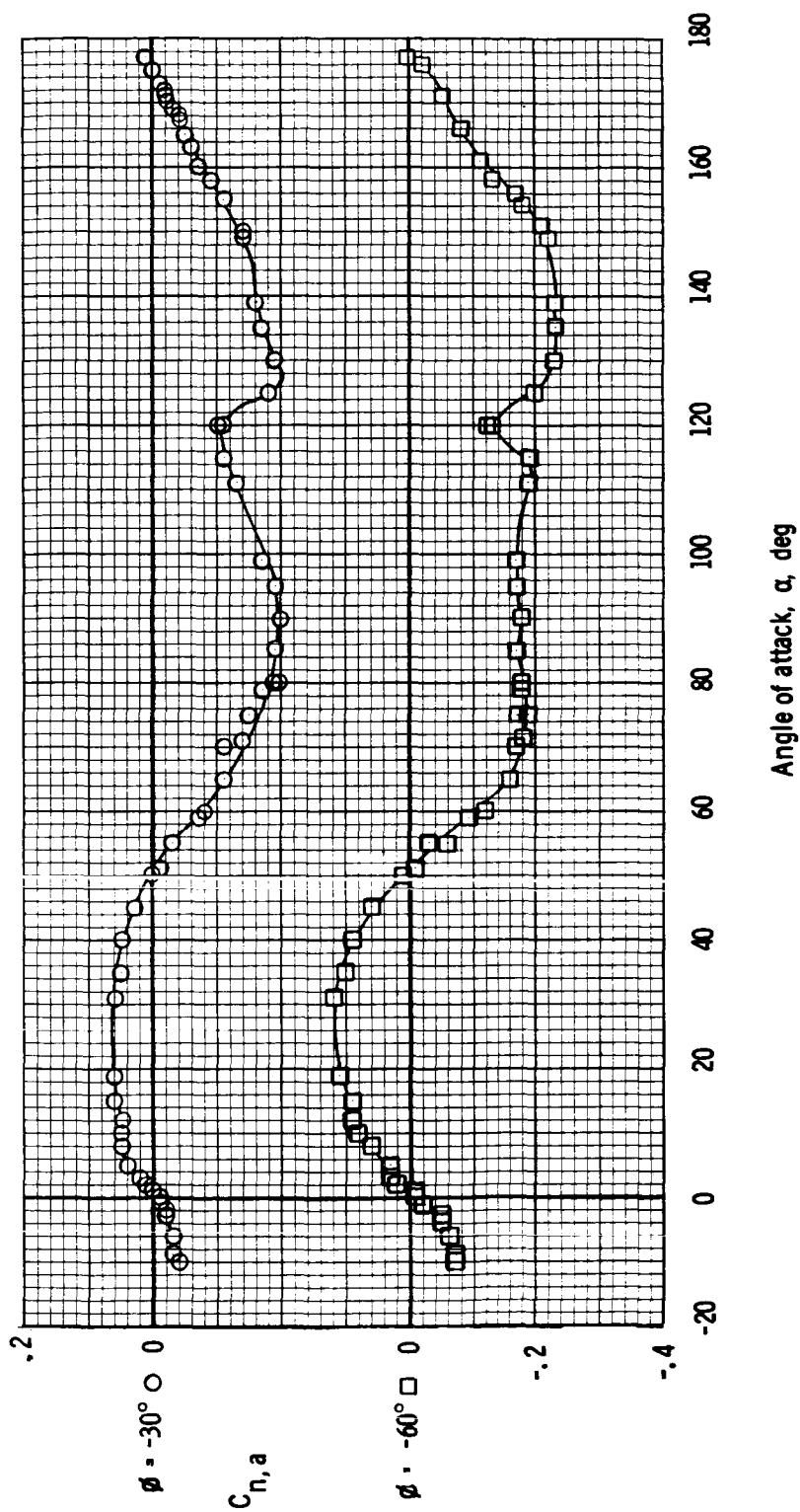
Figure 6. - Continued.

(e) Yawing-moment coefficient.

Figure 6. - Continued.
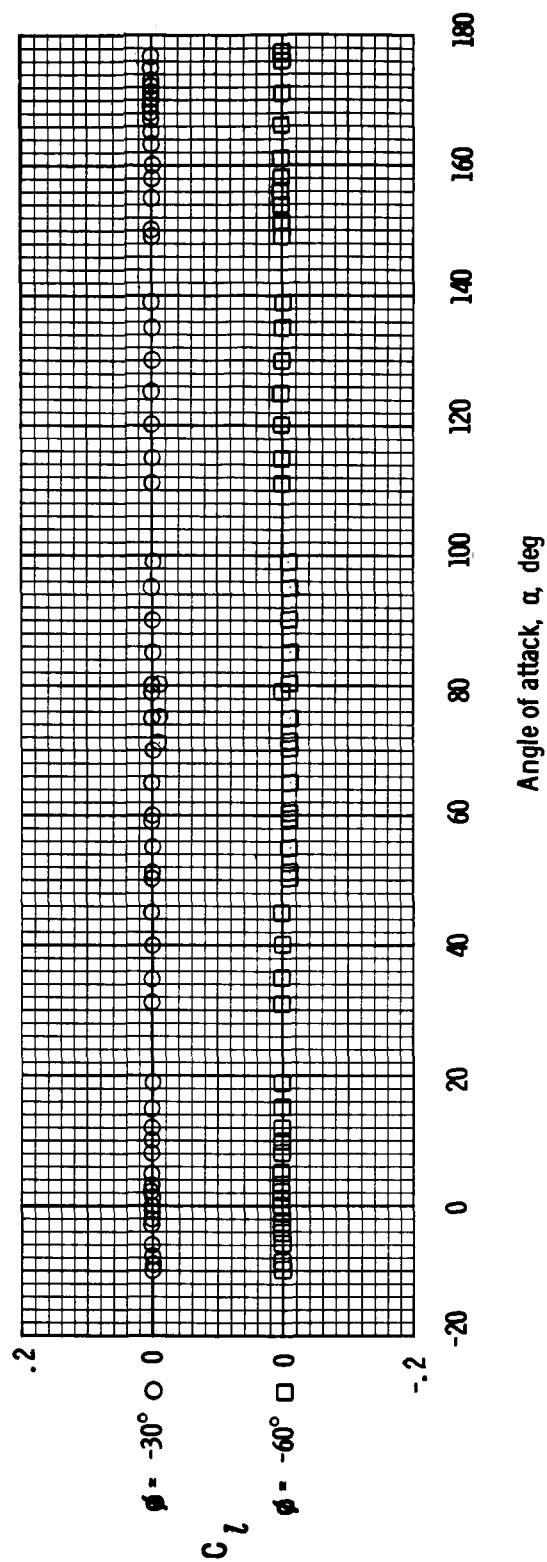
(f) Rolling-moment coefficient.

Figure 6. – Concluded.

30
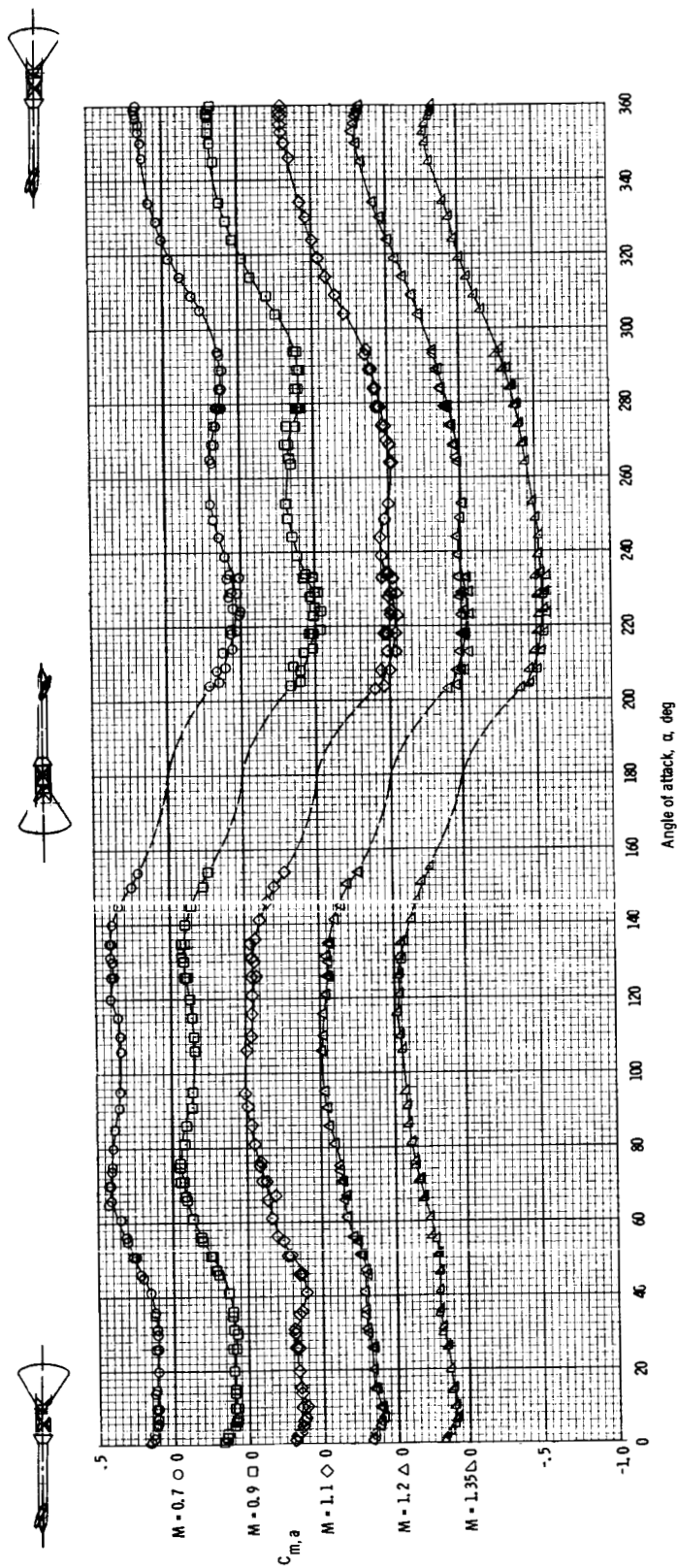
(a) Pitching-moment coefficient at M = 0.7 to 1.35.

Figure 7. – Aerodynamic characteristics of the Apollo launch escape vehicle with canard surfaces deployed, at M = 0.7 to 3.4, with $\phi = 0°$.
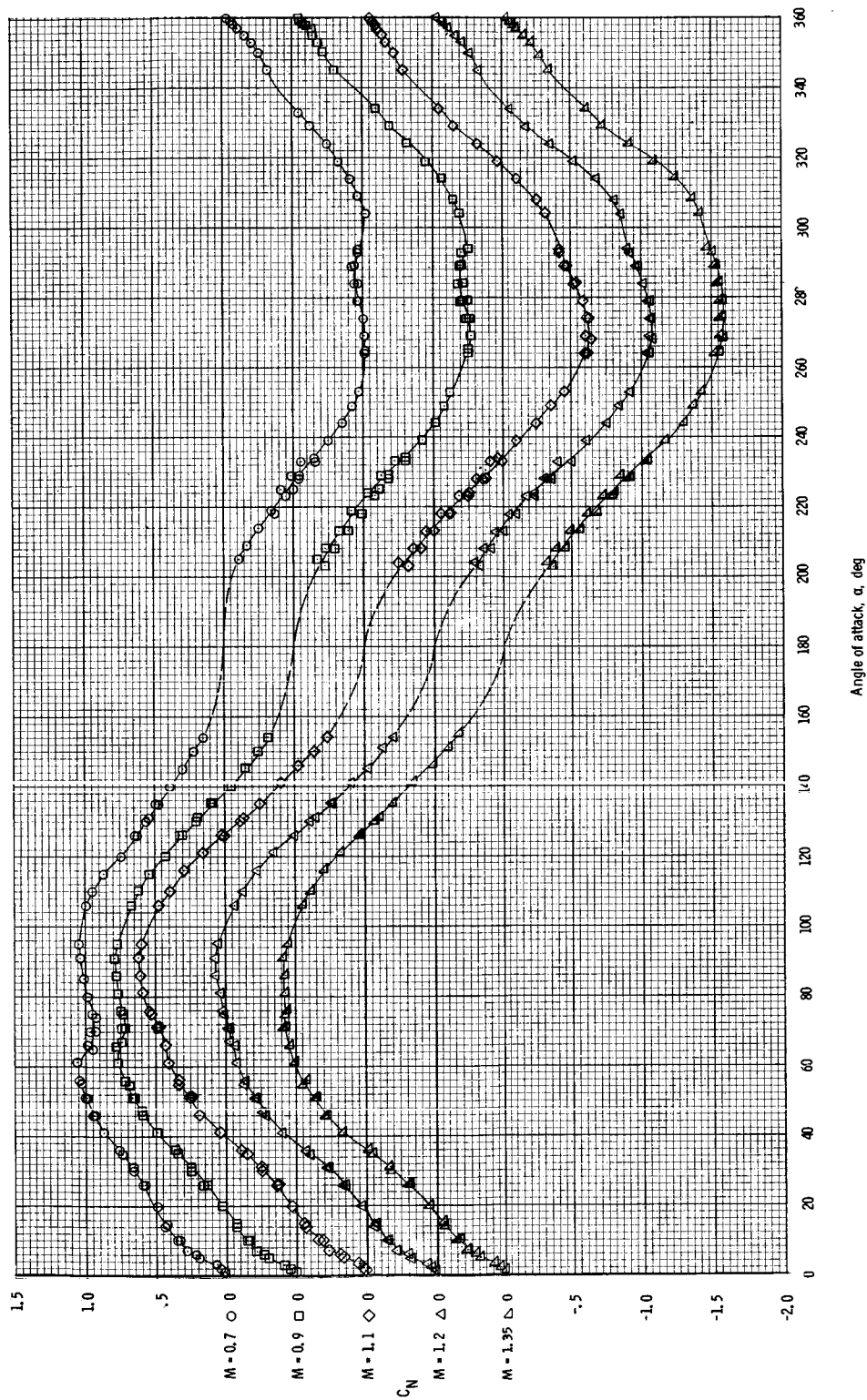
31

(b) Pitching-moment coefficient at M = 1.64 to 3.4.

Figure 7. - Continued.

(c) Normal-force coefficient at M = 0.7 to 1.35.
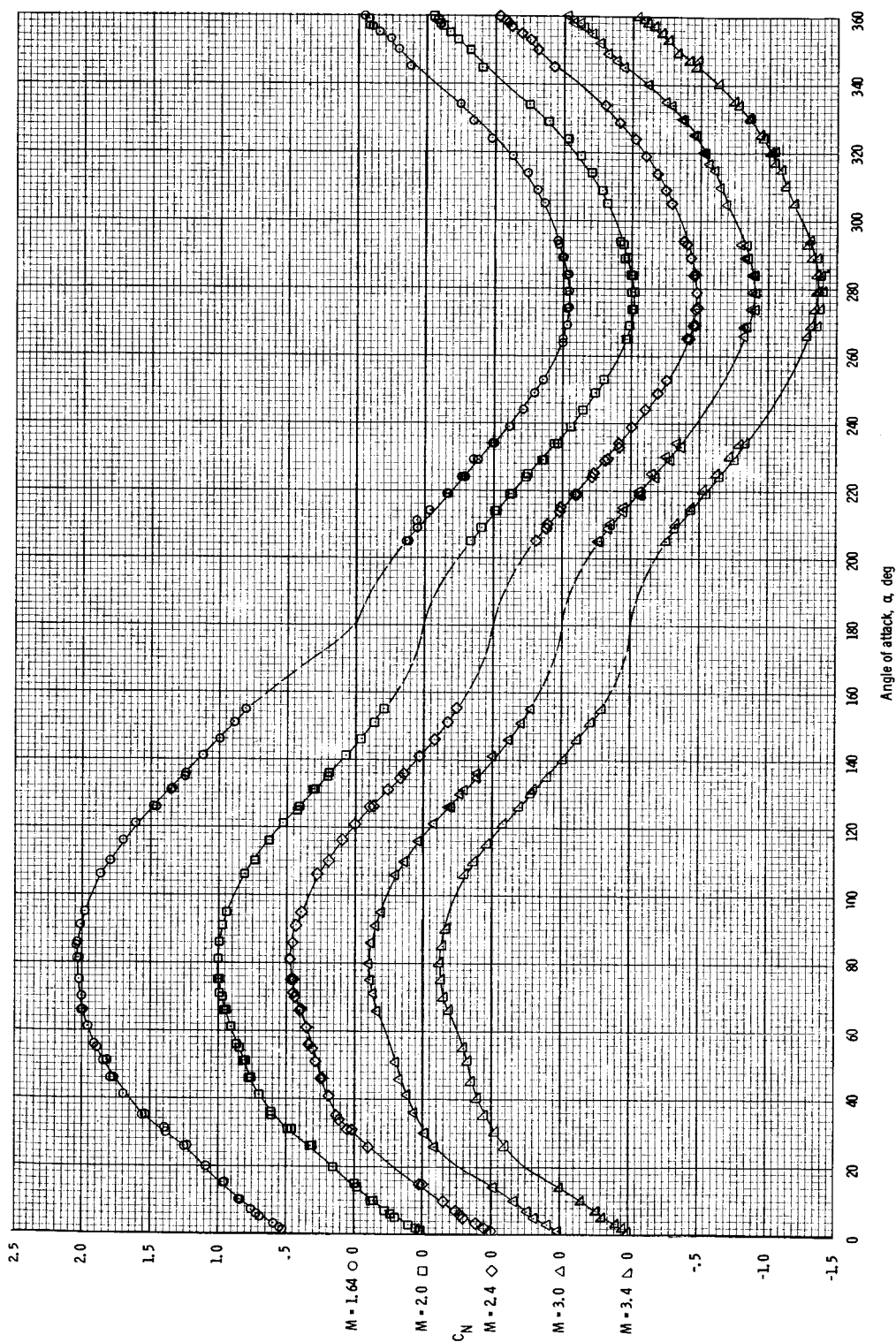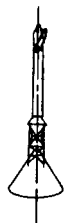
Figure 7. - Continued.

33

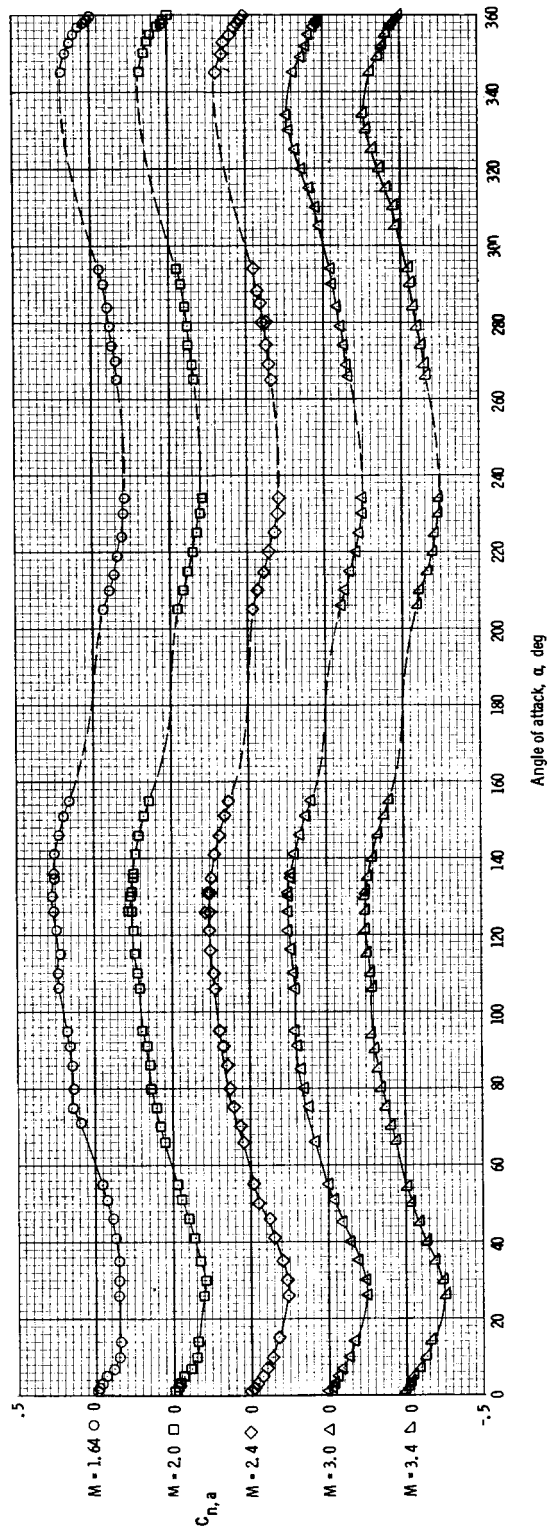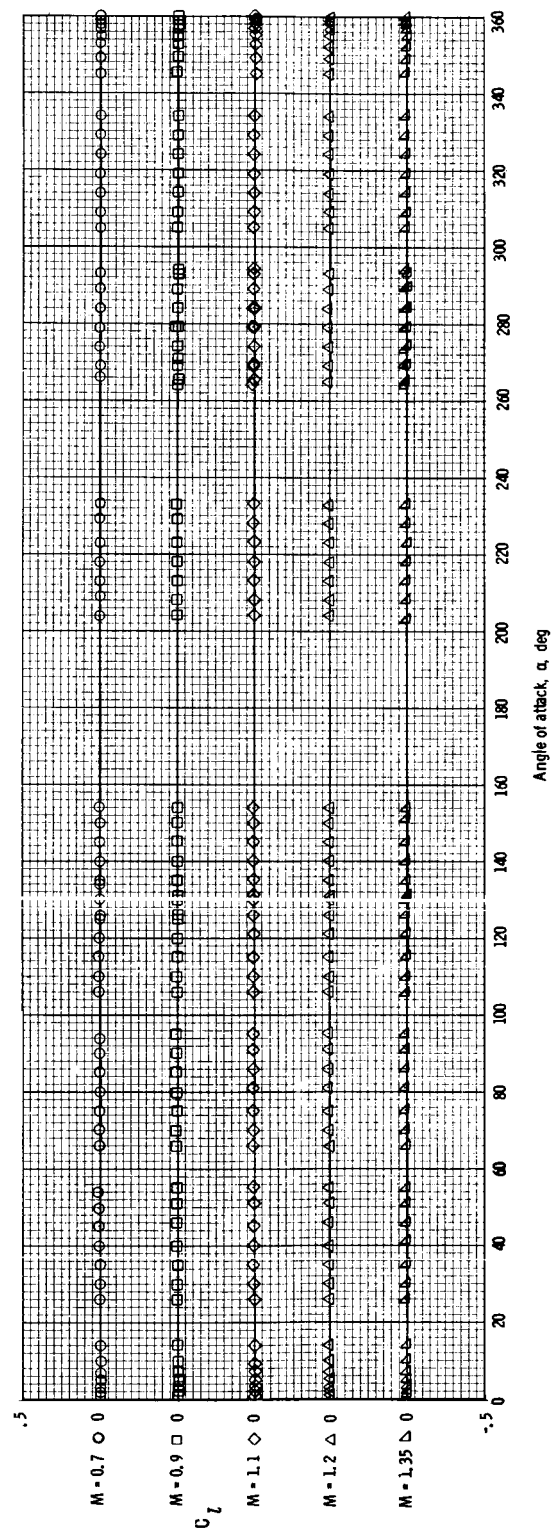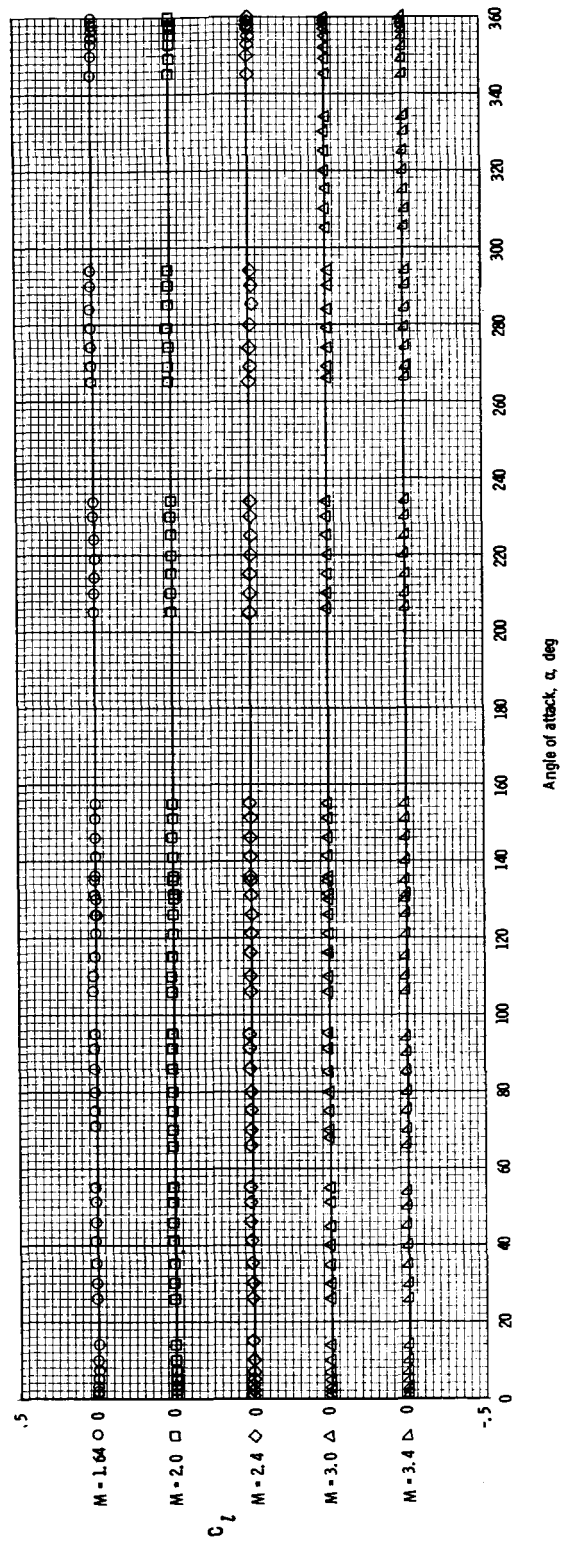(d) Normal-force coefficient at M = 1.64 to 3.4.

Figure 7. - Continued.

34

Angle of attack, α, deg

(e) Axial-force coefficient at M = 0.7 to 1.35.

Figure 7. - Continued.

35

Angle of attack, α, deg

(f) Axial-force coefficient at M = 1.64 to 3.4.

Figure 7. - Continued.

36

(g) Side-force coefficient at M = 0.7 to 1.35.

Figure 7. - Continued.

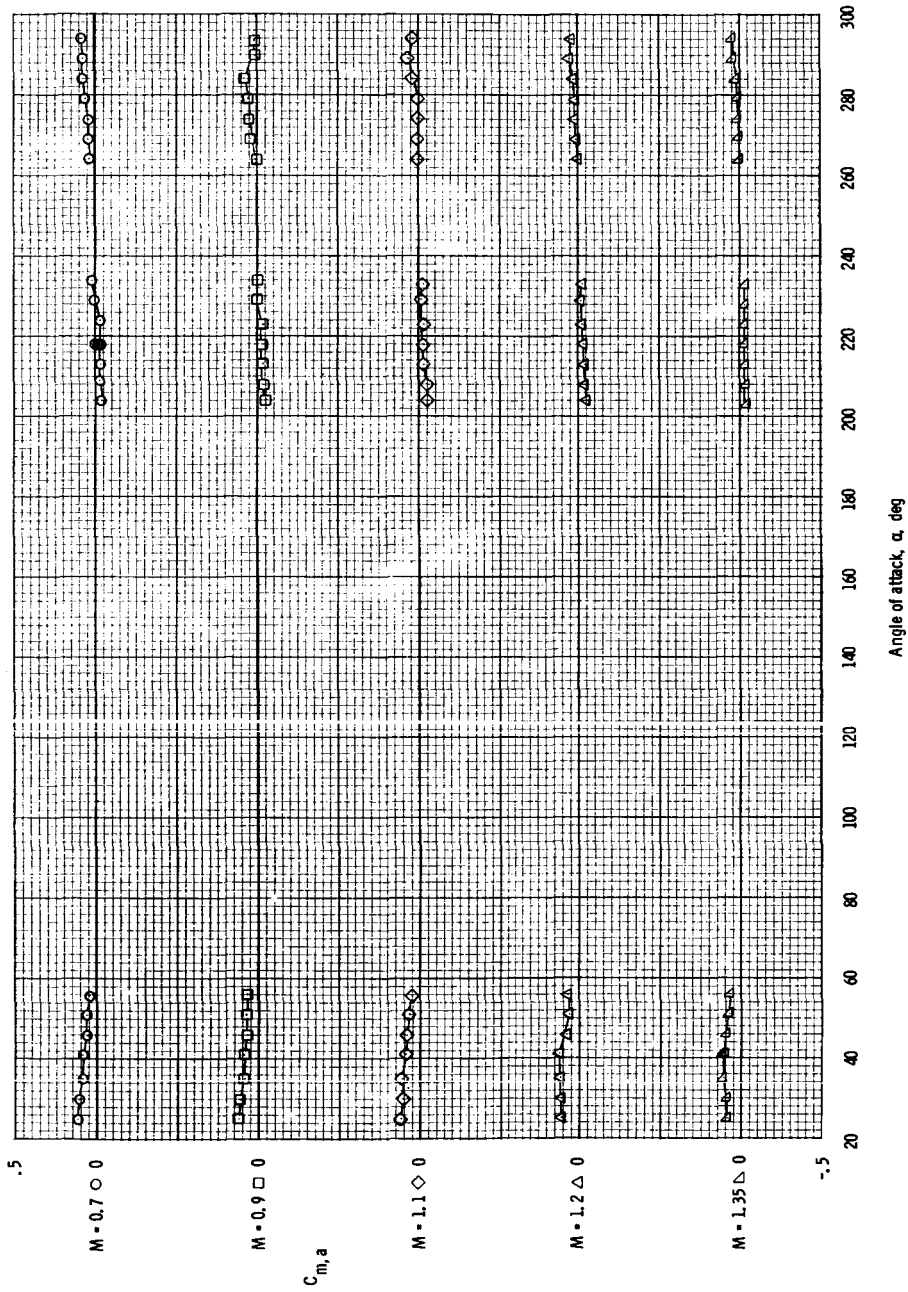(h) Side-force coefficient at M = 1.64 to 3.4.

Figure 7. - Continued.

(i) Yawing-moment coefficient at M = 0.7 to 1.35.
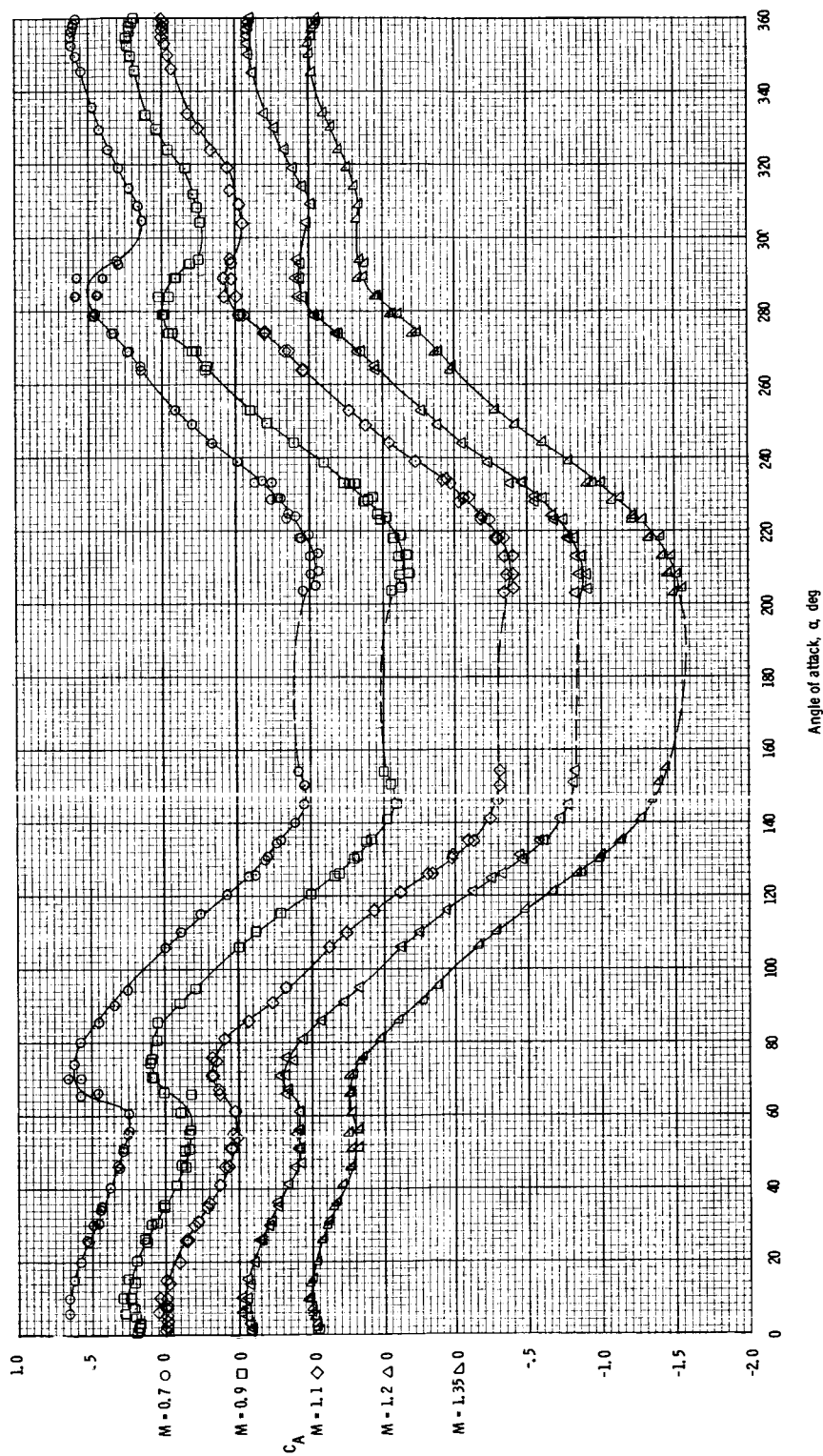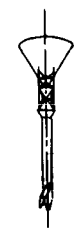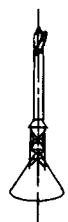
Figure 7.- Continued.

Angle of attack, α, deg

(j) Yawing-moment coefficient at M = 1.64 to 3.4.

Figure 7. - Continued.

40

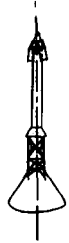(k) Rolling-moment coefficient at M = 0.7 to 1.35.
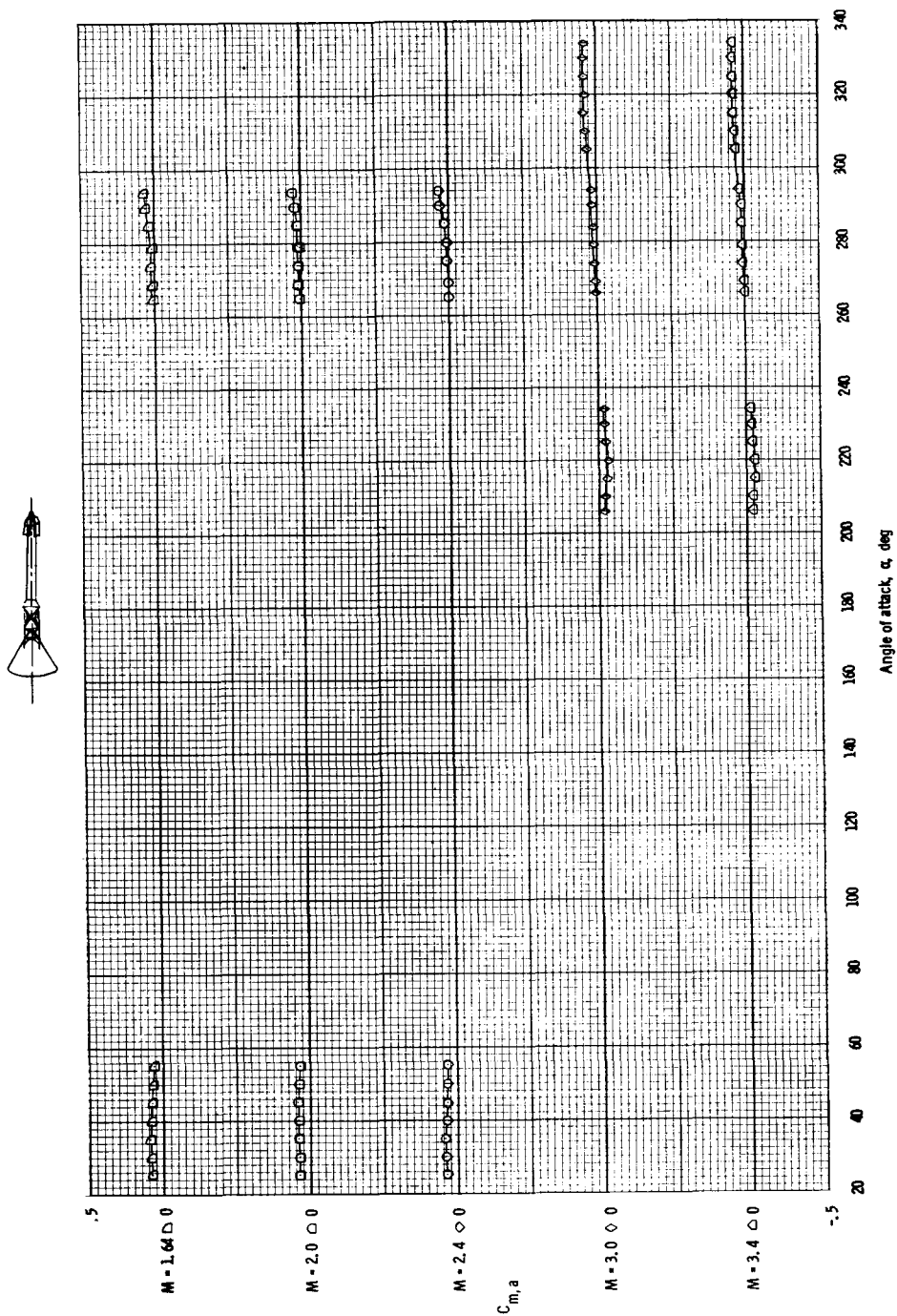
Figure 7. - Continued.

41

Angle of attack, α, deg
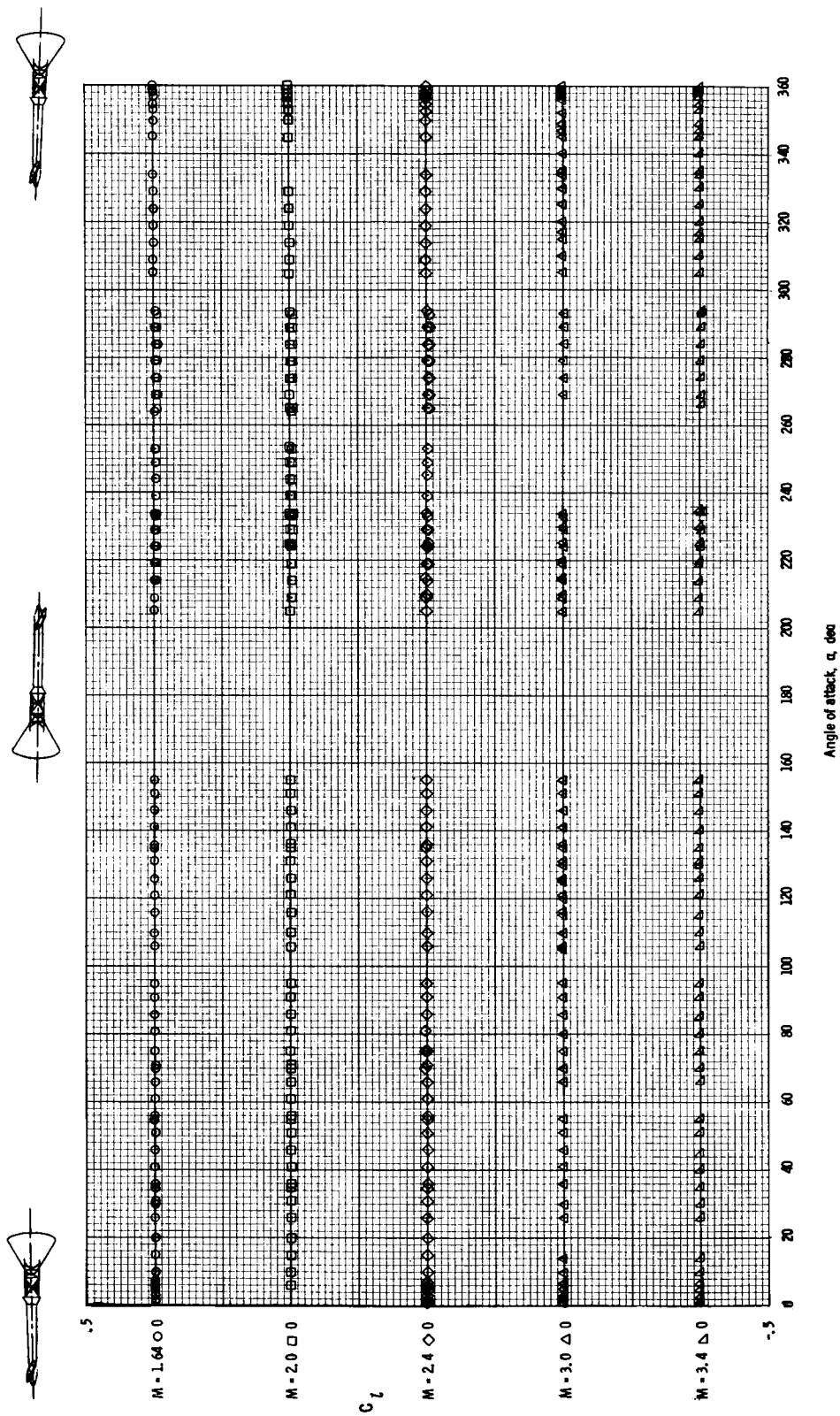
(1) Rolling-moment coefficient at M = 1.64 to 3.4.

Figure 7. - Concluded.
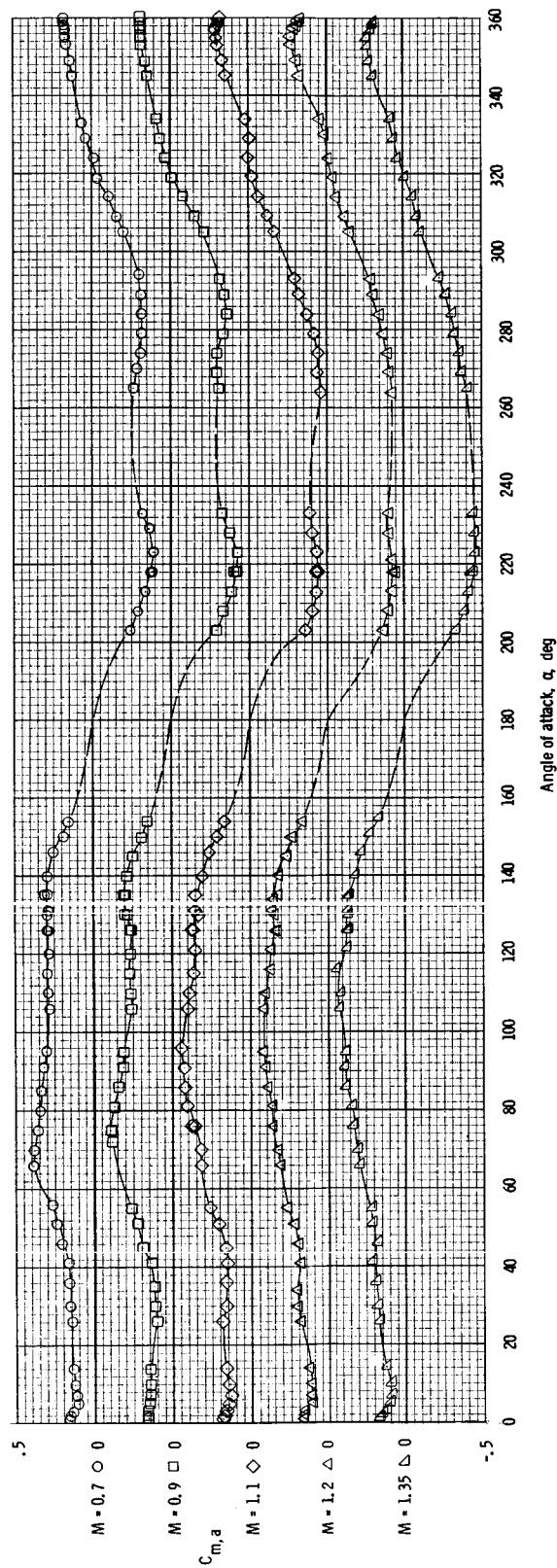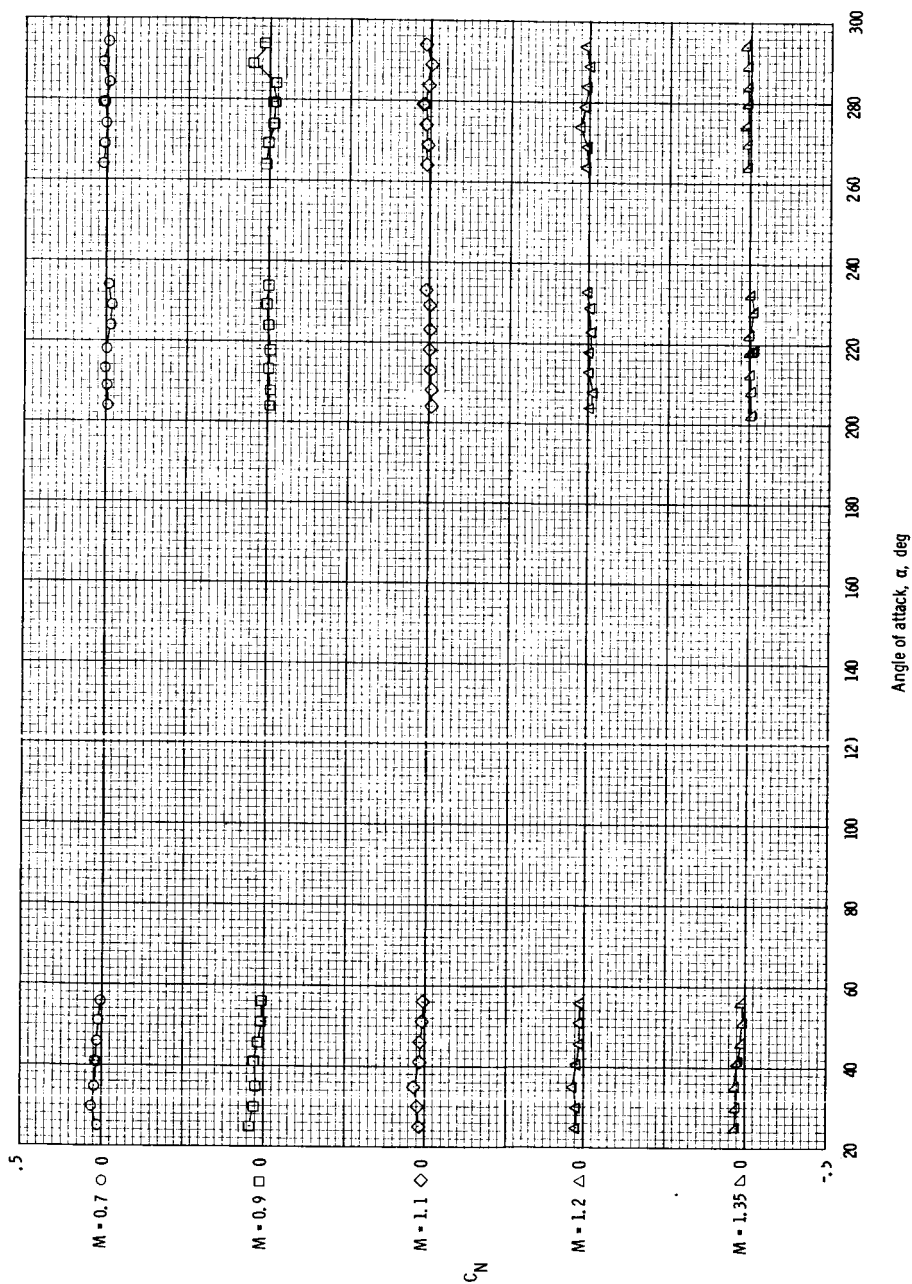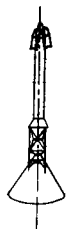
(a) Pitching-moment coefficient at M = 0.7 to 1.35.

Figure 8.- Aerodynamic characteristics of the Apollo launch escape vehicle with canard surfaces deployed, at M = 0.7 to 3.4, with ϕ = -30°.
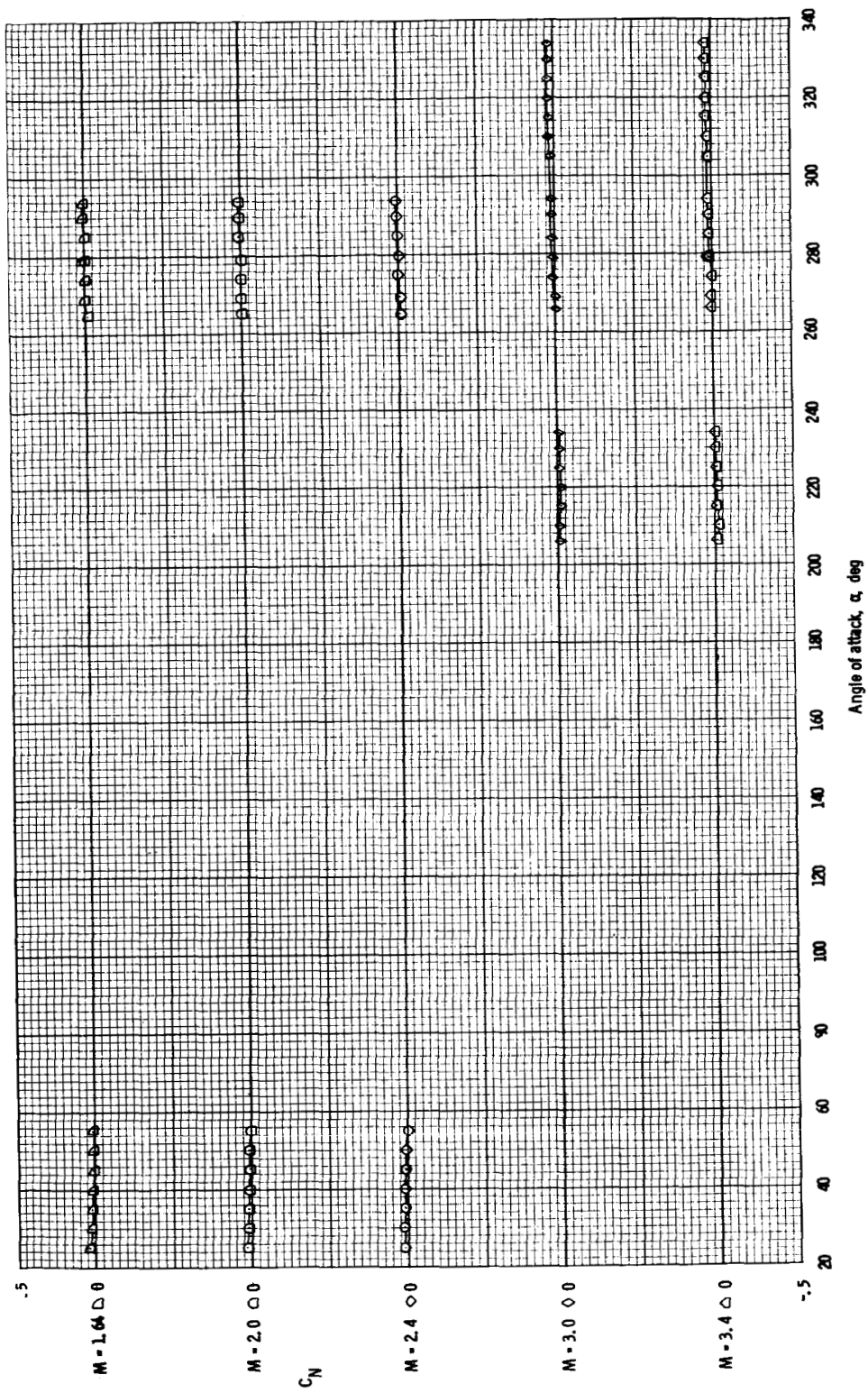
(b) Pitching-moment coefficient at M = 1.64 to 3.4.

Figure 8. – Continued.

44
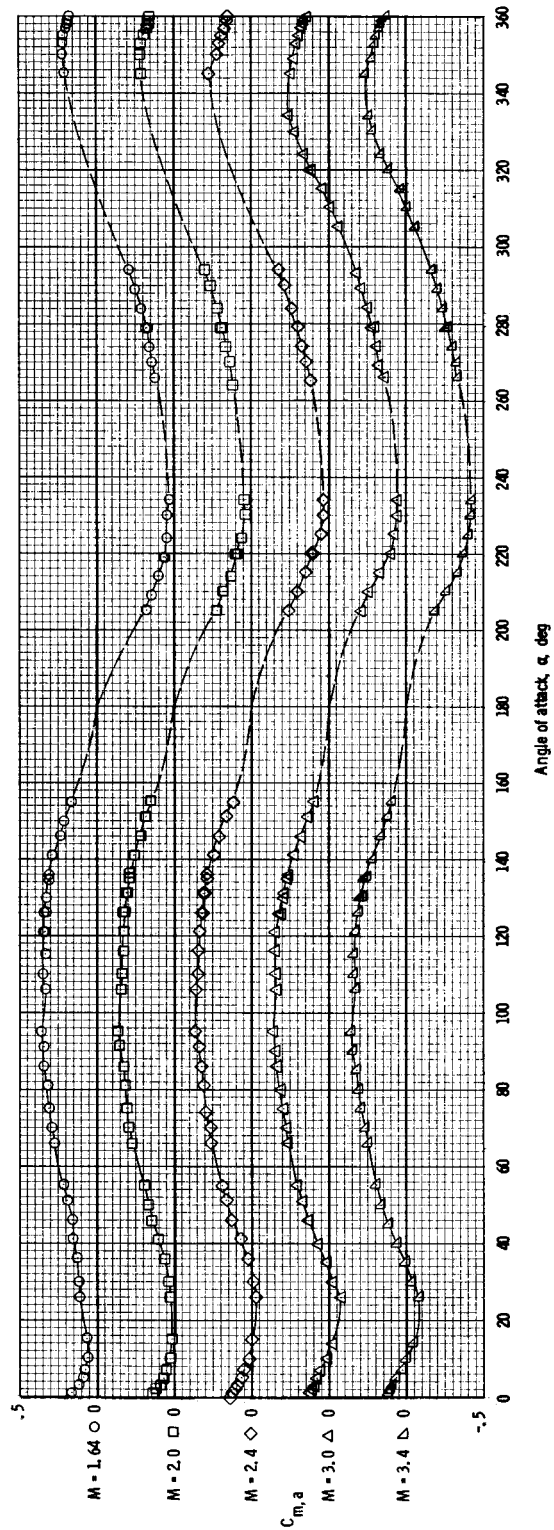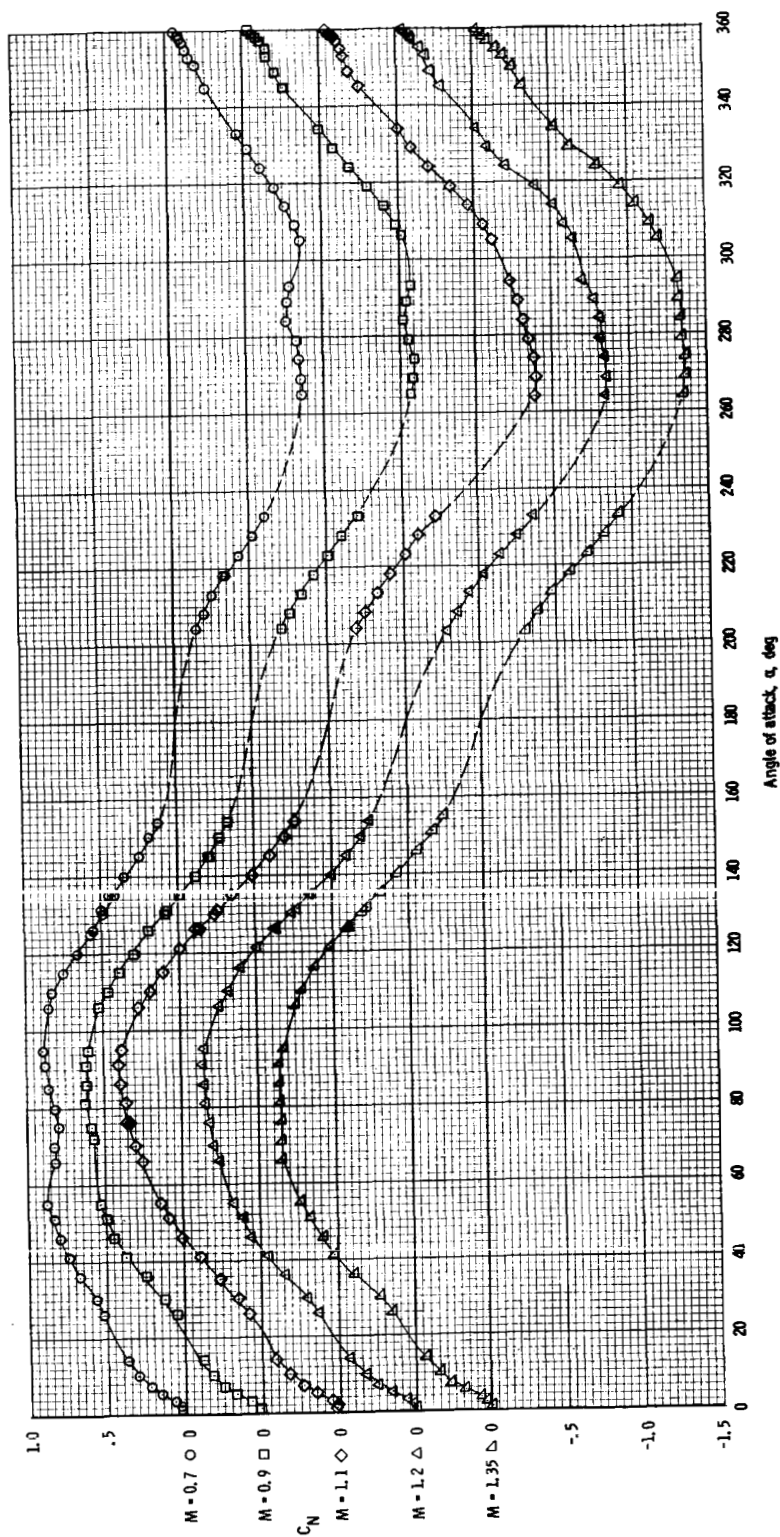
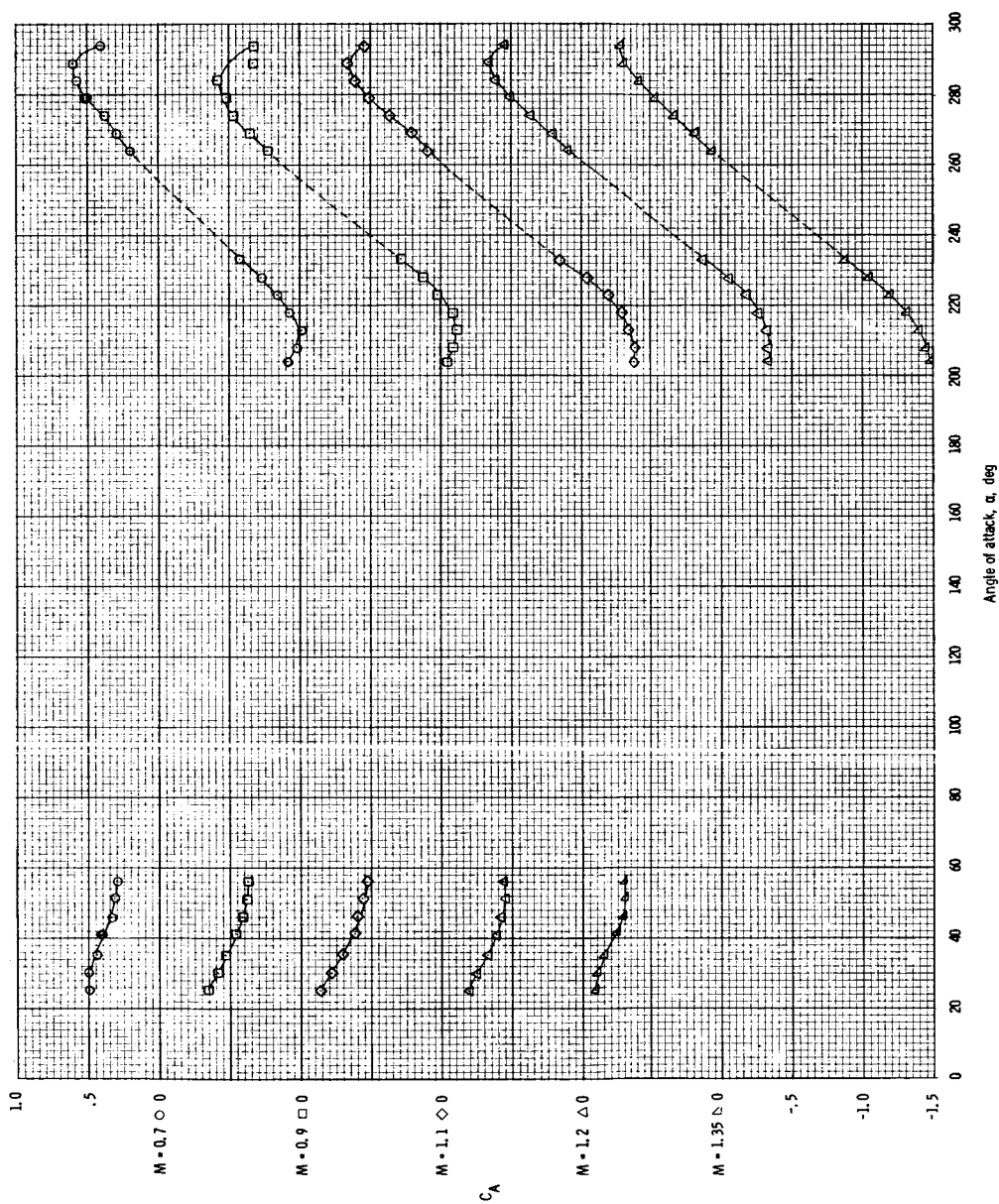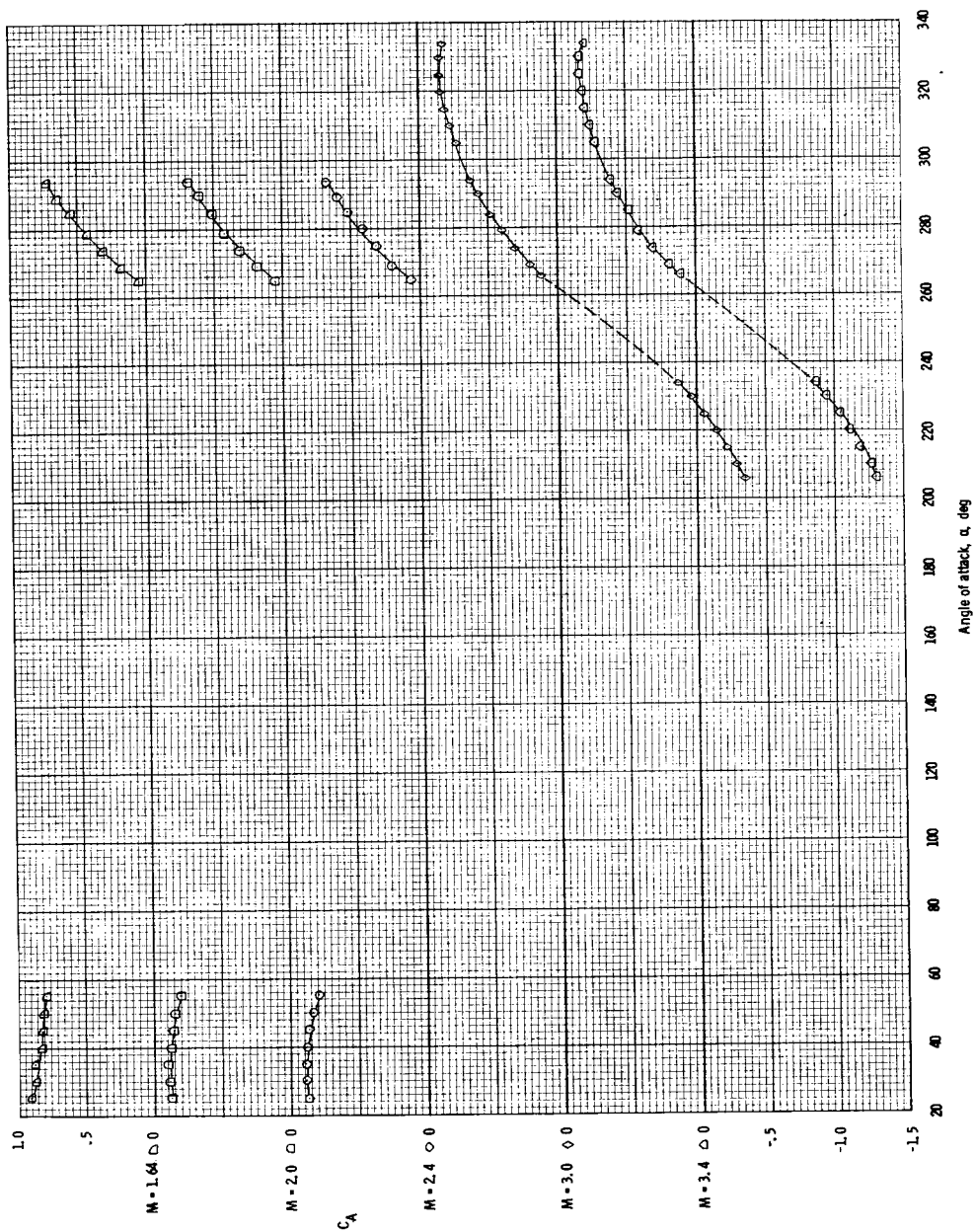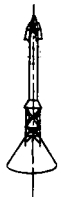(c) Normal-force coefficient at M = 0.7 to 1.35.
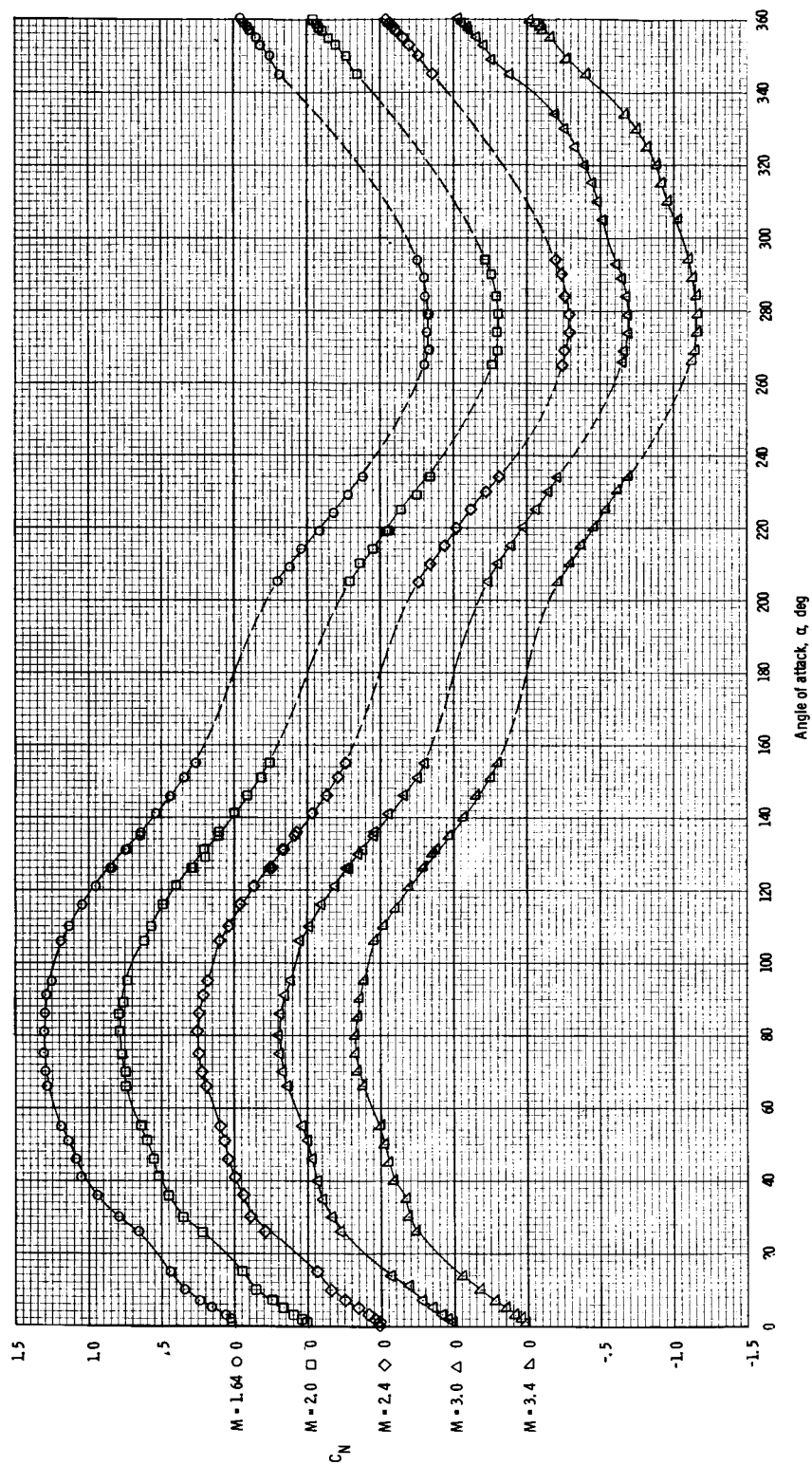
Figure 8. - Continued.

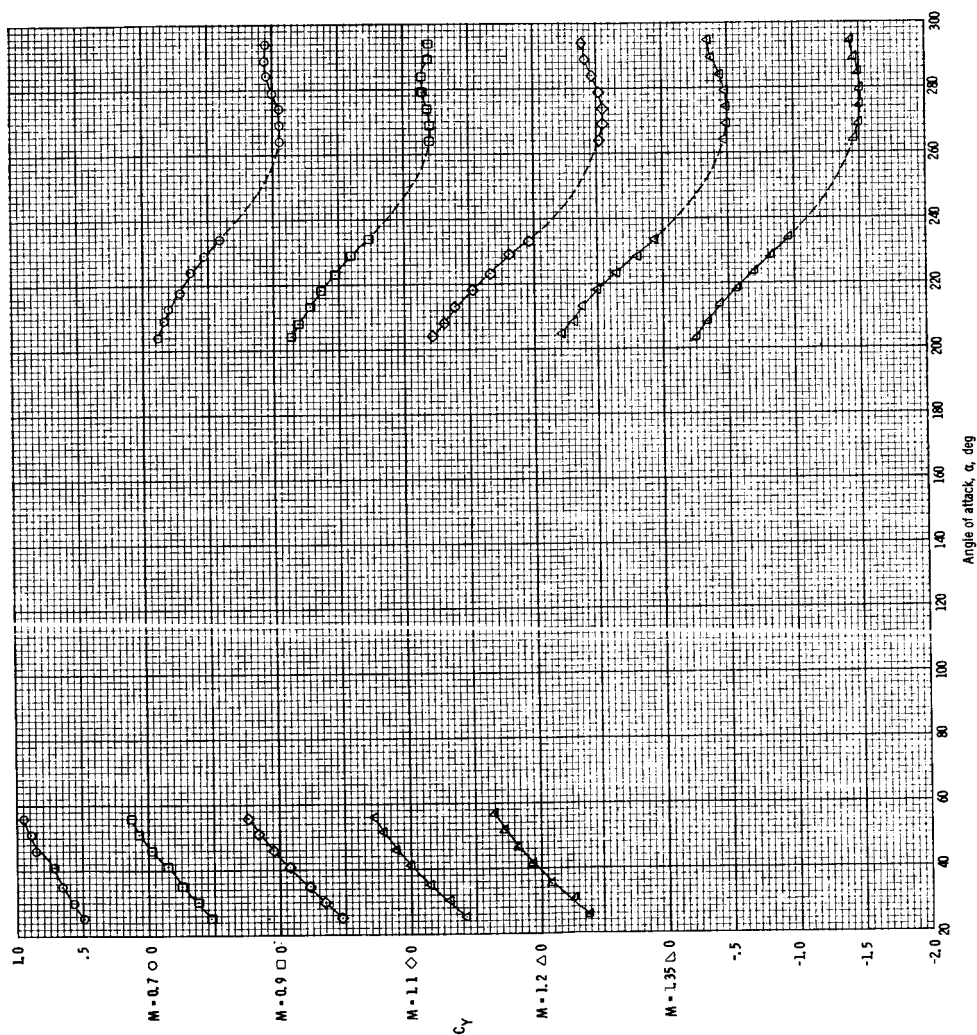(d) Normal-force coefficient at M = 1.64 to 3.4.
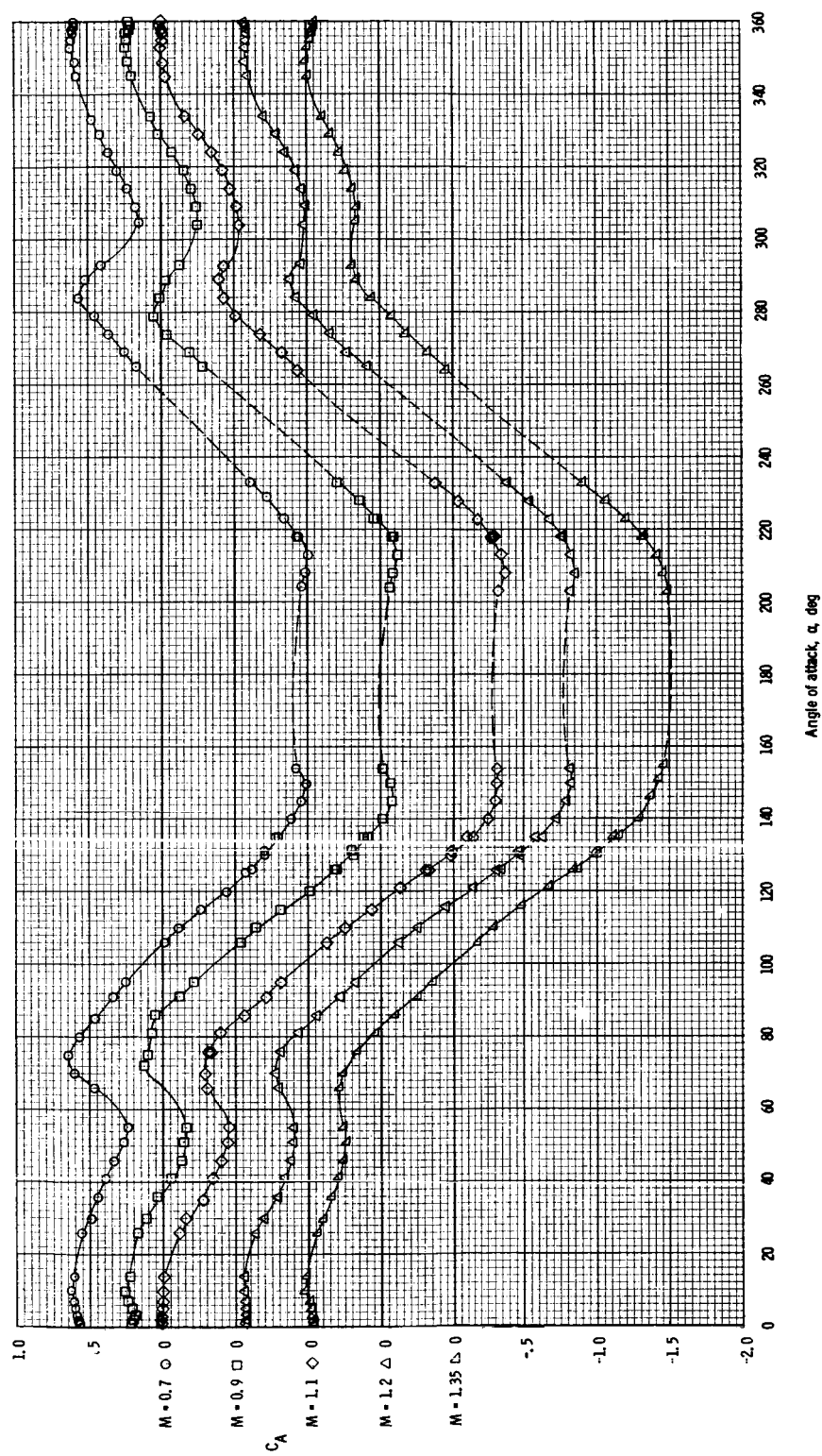
Figure 8. - Continued.

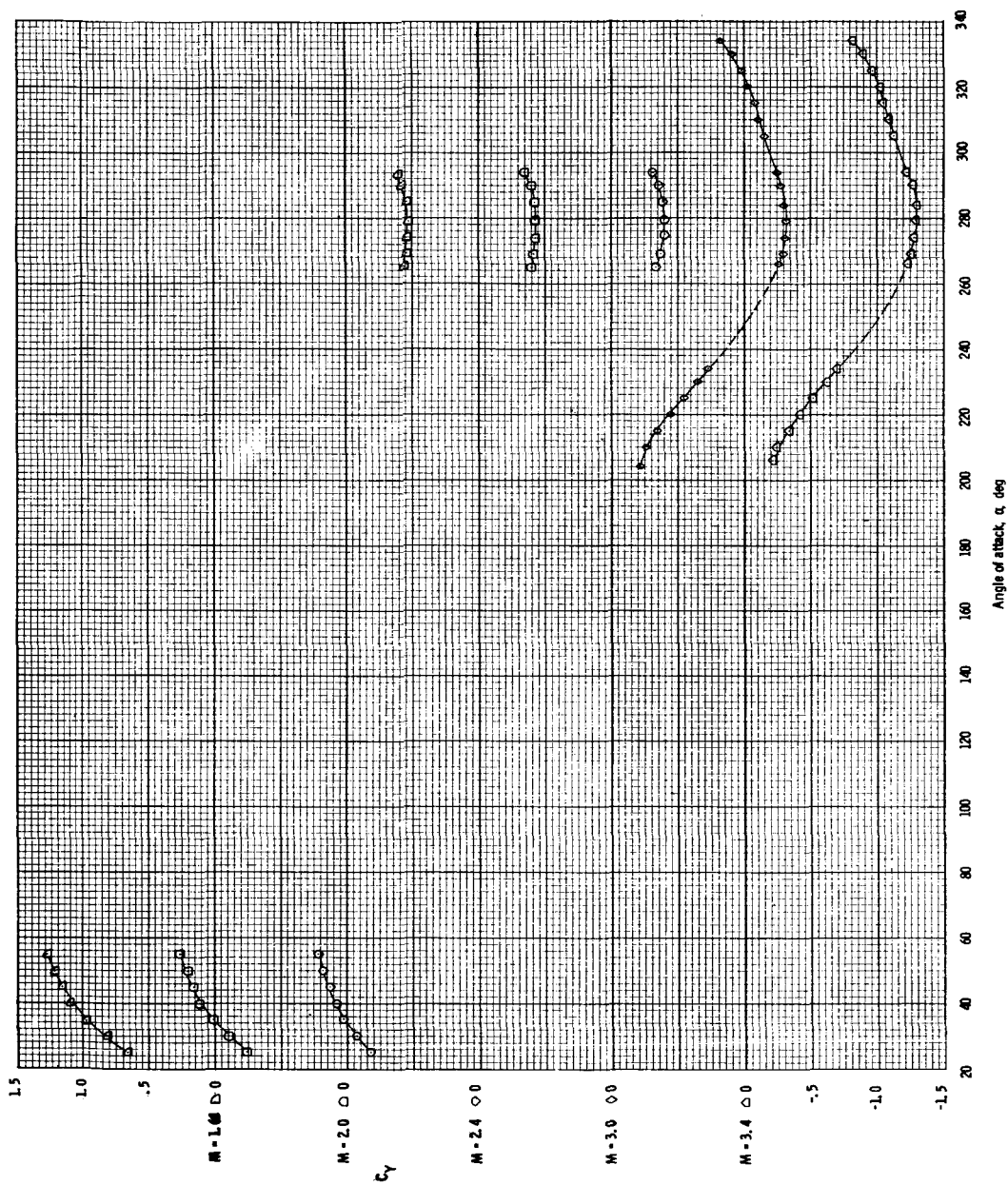(e) Axial-force coefficient at M = 0.7 to 1.35.

Figure 8. - Continued.

47
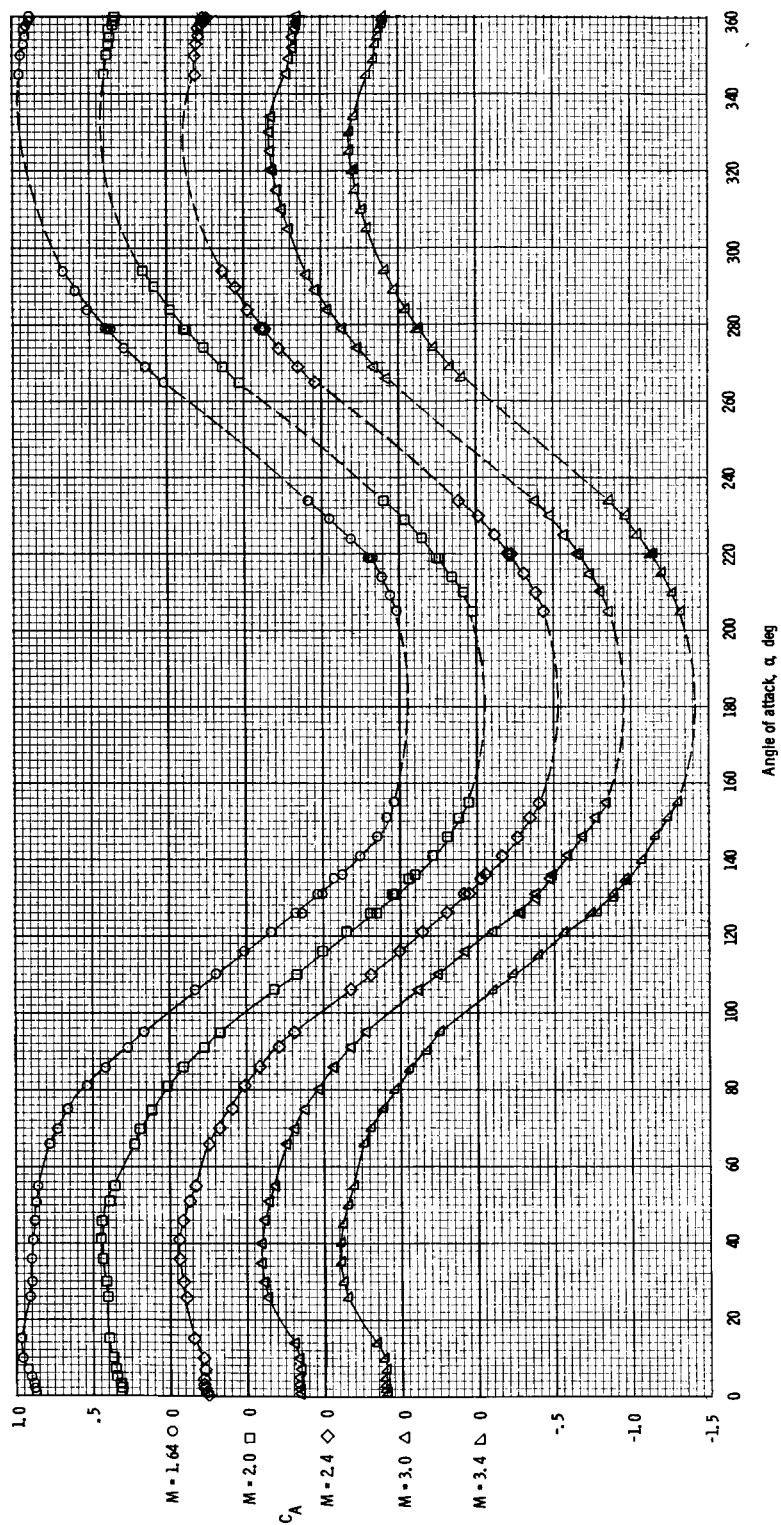
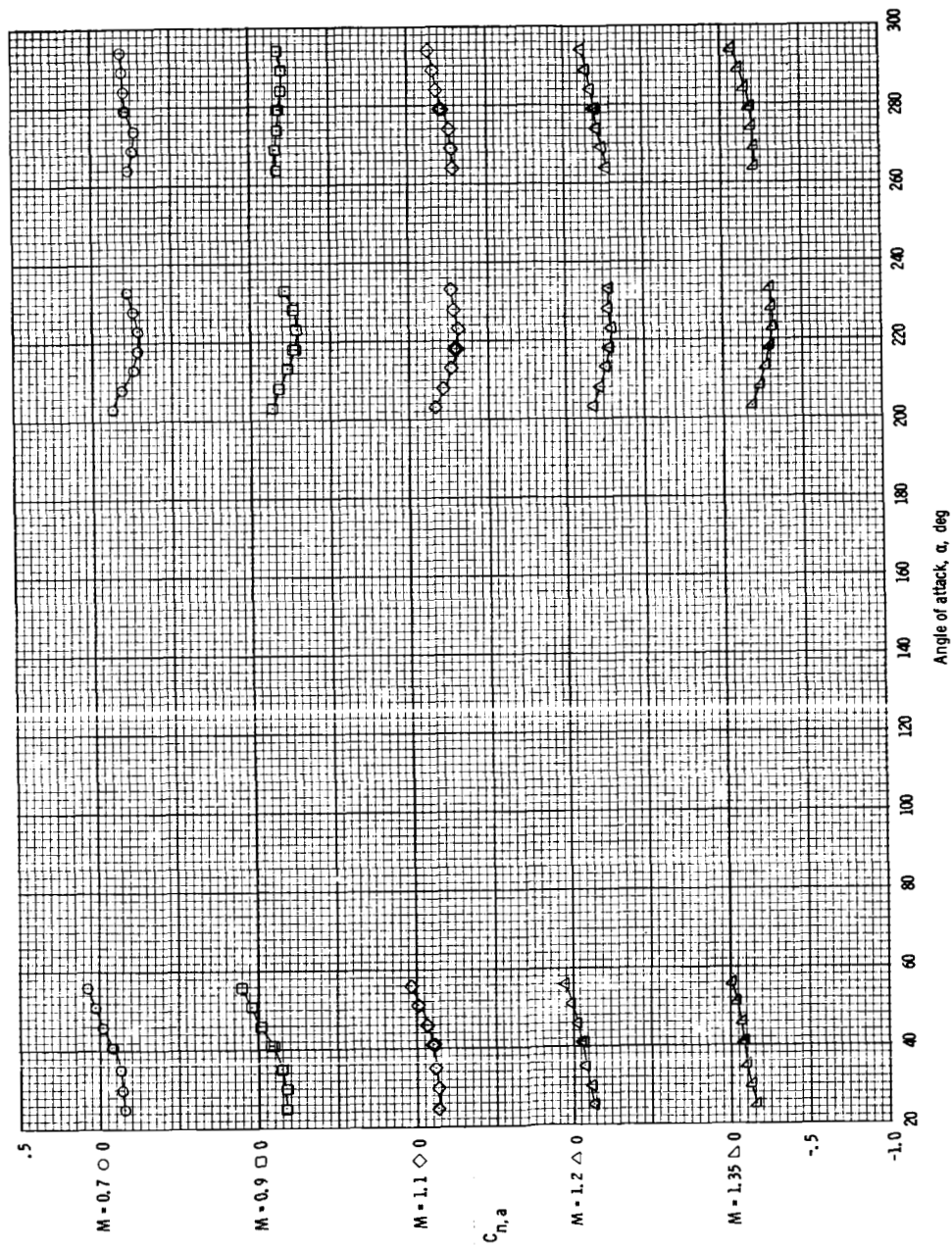(f) Axial-force coefficient at M = 1.64 to 3.4.
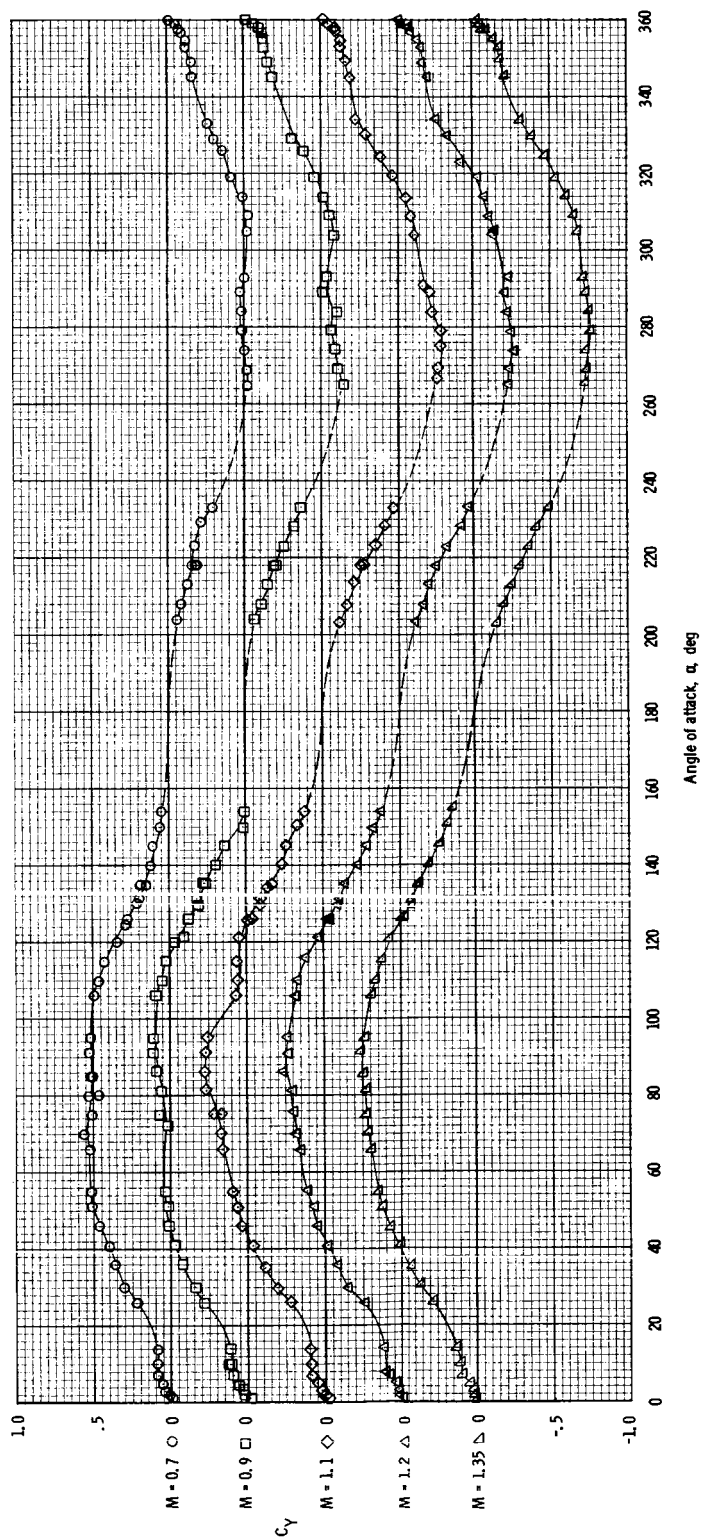
Figure 8. - Continued.

(g) Side-force coefficient at M = 0.7 to 1.35.
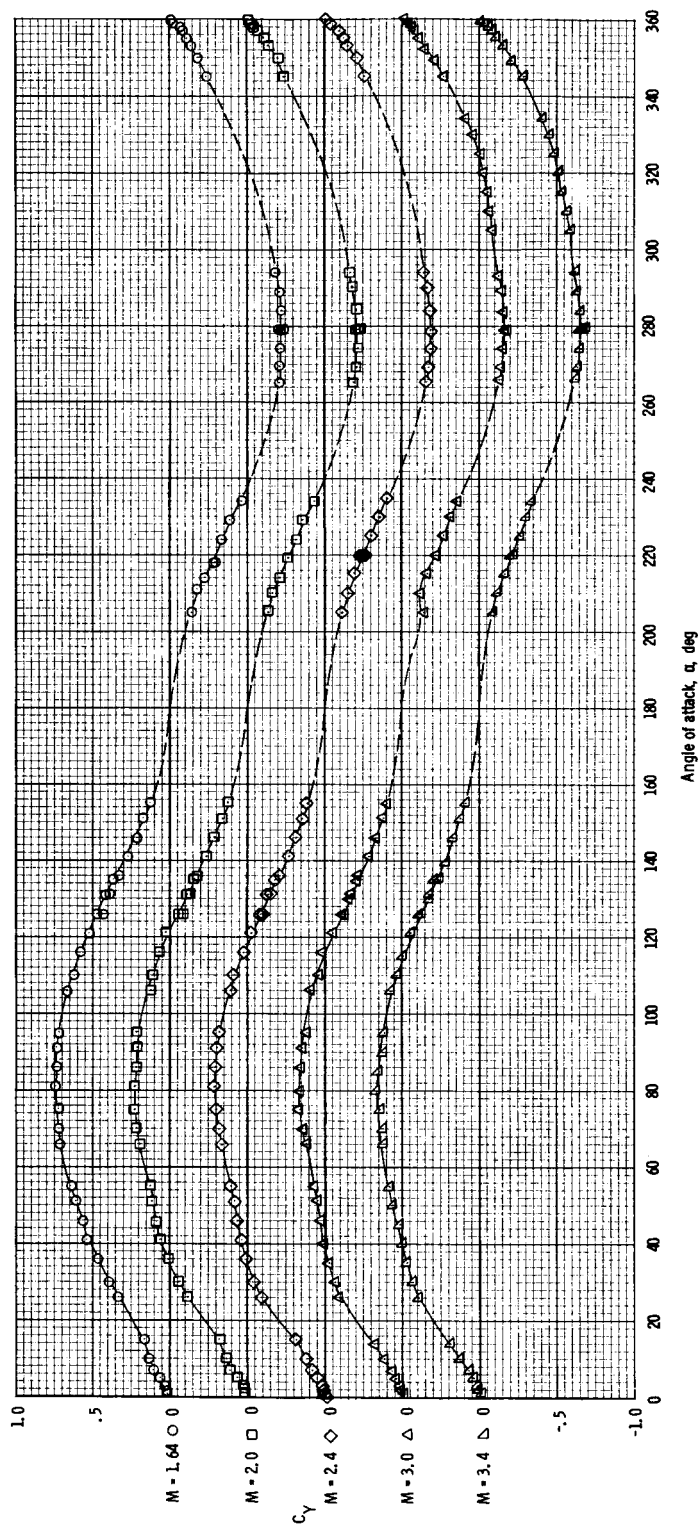
Figure 8. - Continued.
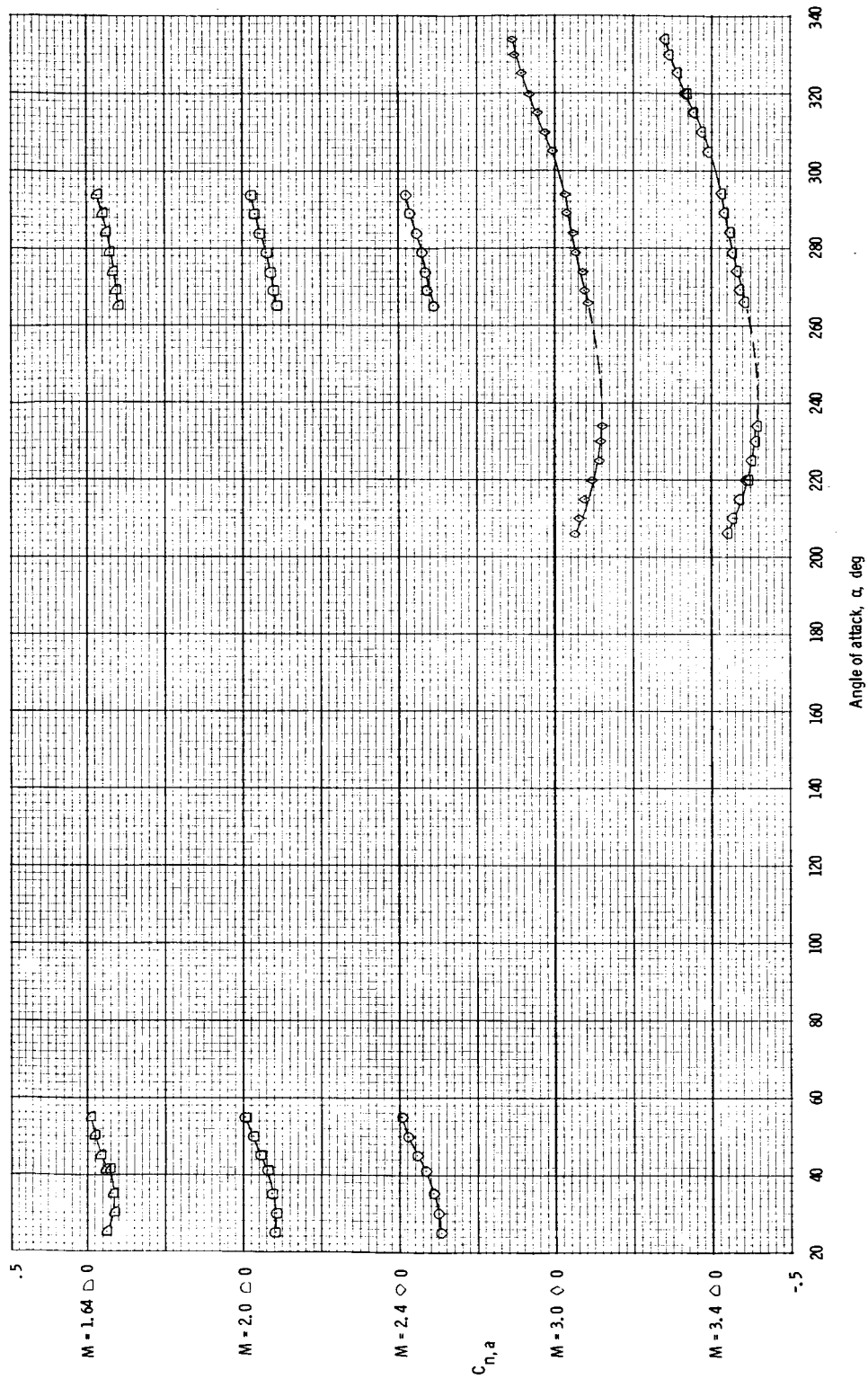
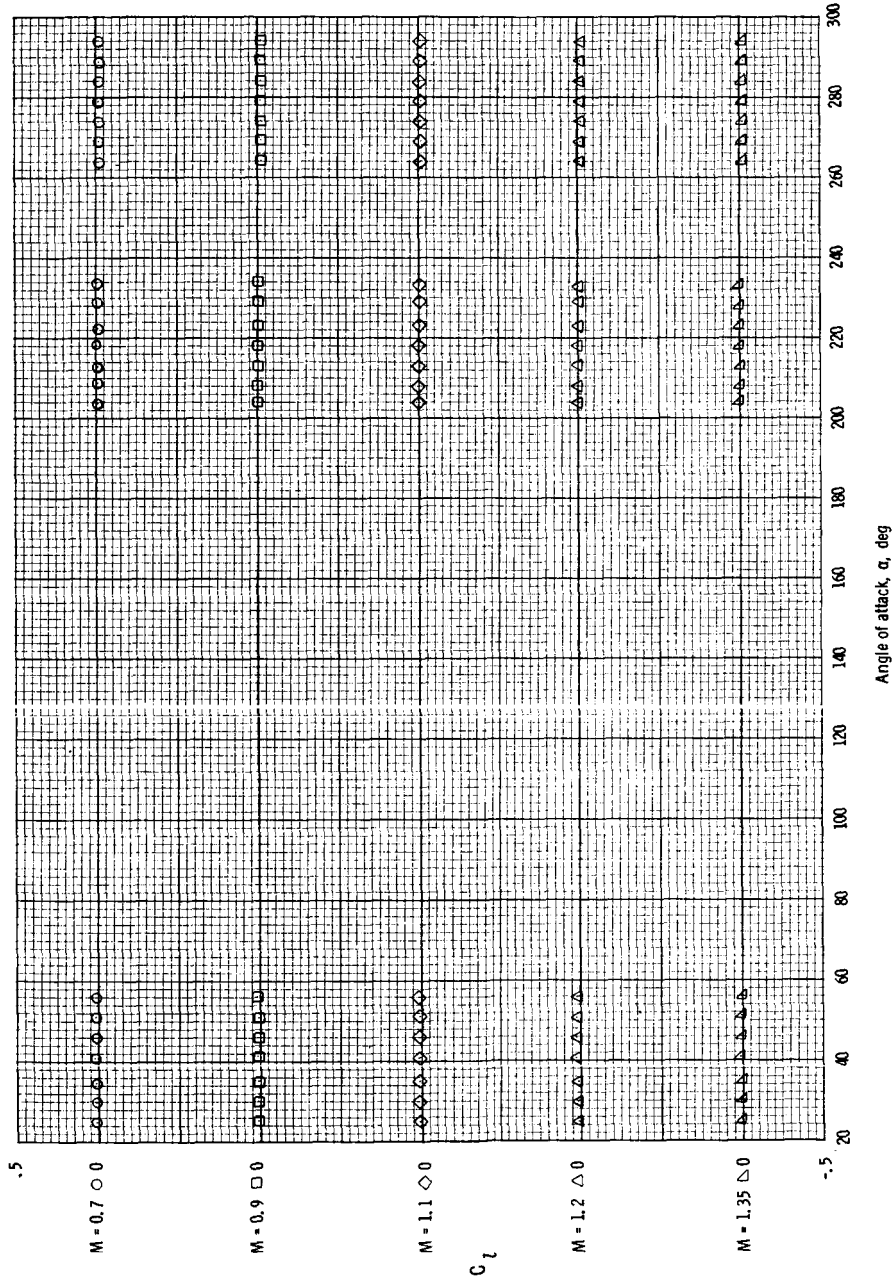(h) Side-force coefficient at M = 1.64 to 3.4.
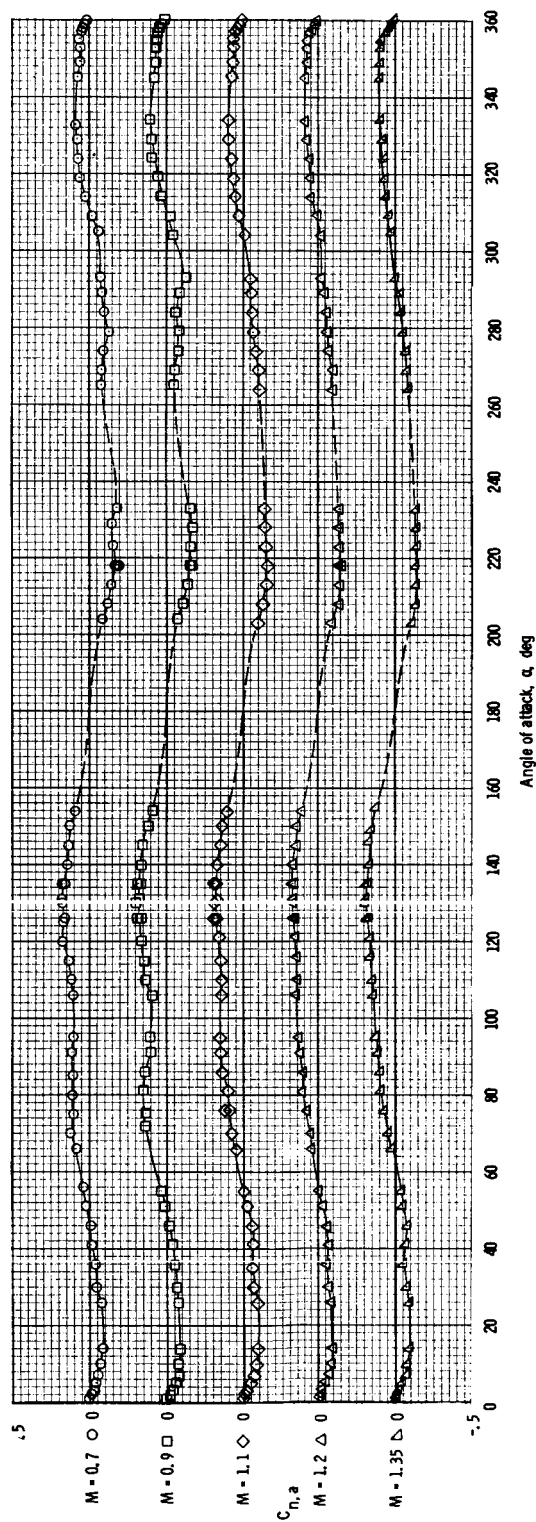
Figure 8. - Continued.

(i) Yawing-moment coefficient at M = 0.7 to 1.35.
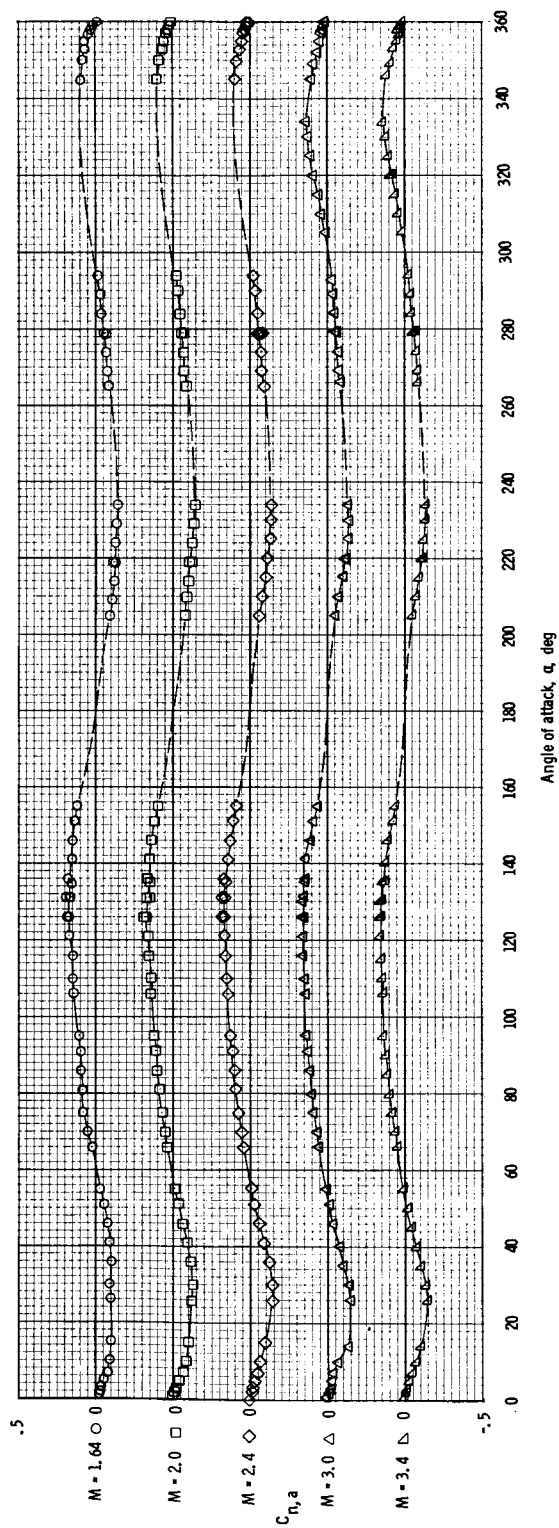
Figure 8. - Continued.

(j) Yawing-moment coefficient at M = 1.64 to 3.4.
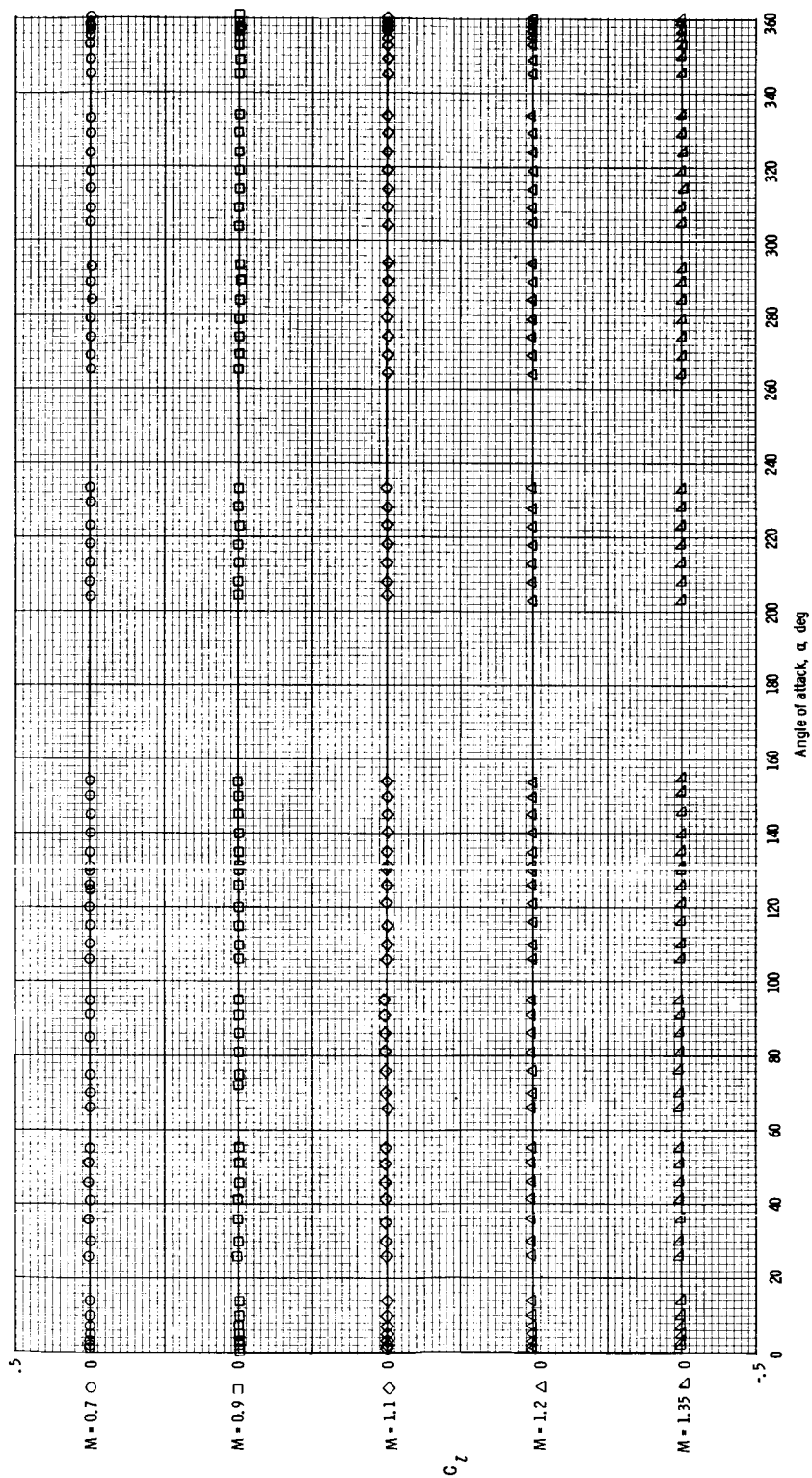
Figure 8. - Continued.

(k) Rolling-moment coefficient at M = 0.7 to 1.35.

Figure 8. - Continued.
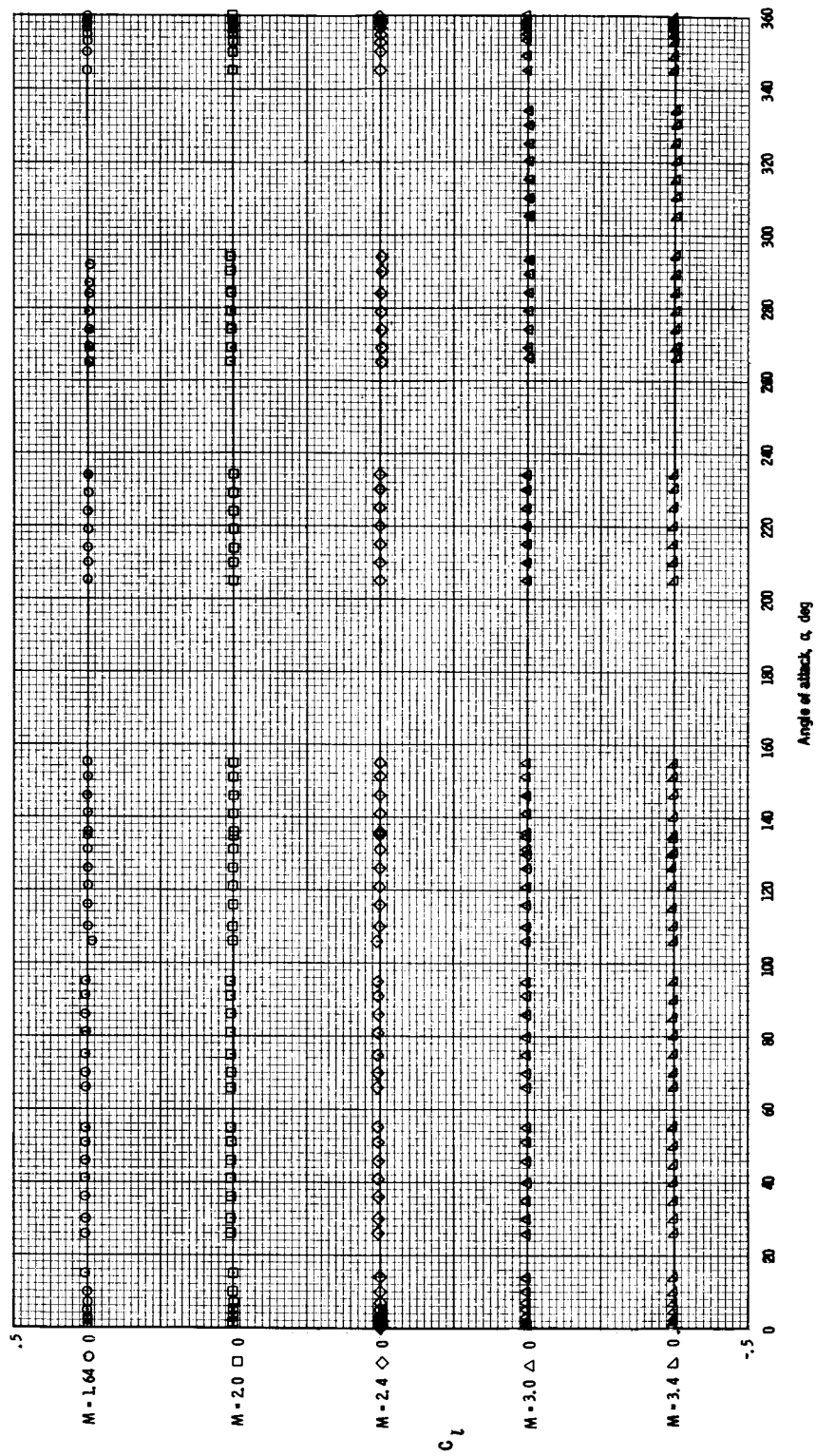
(1) Rolling-moment coefficient at M = 1.64 to 3.4.

Figure 8. - Concluded.
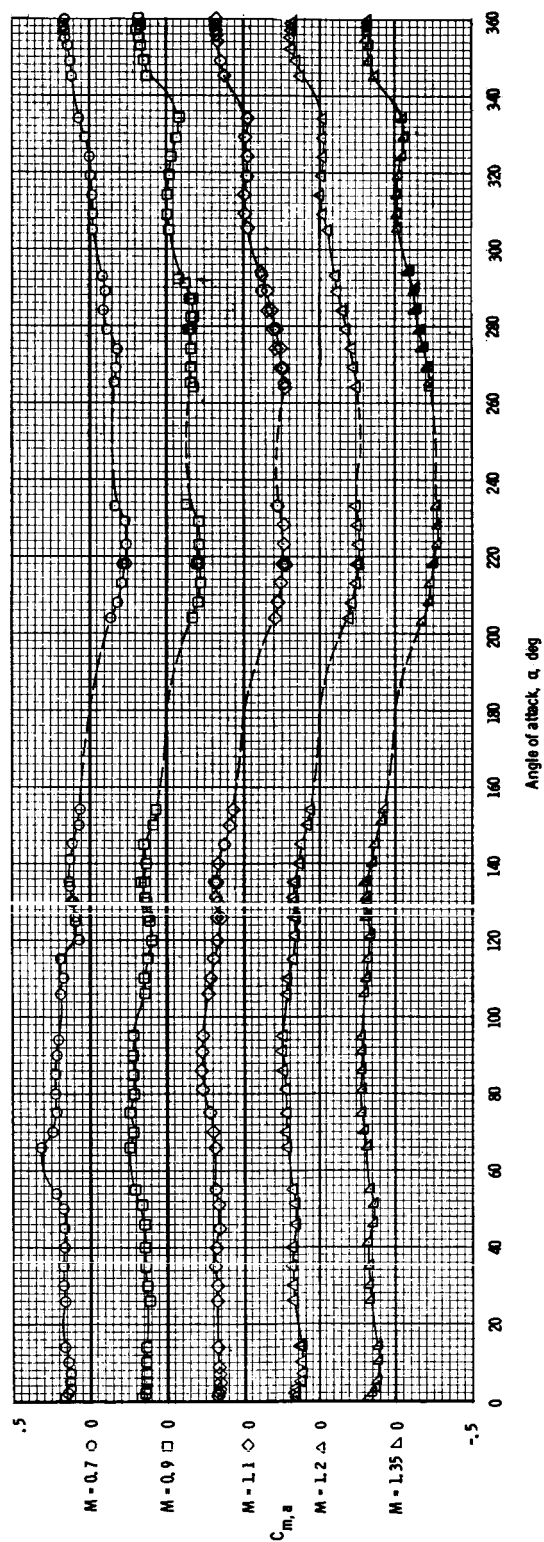
(a) Pitching-moment coefficient at $M = 0.7$ to 1.35.

Figure 9. - Aerodynamic characteristics of the Apollo launch escape vehicle with canard surfaces deployed, at $M = 0.7$ to 3.4, with $\beta = -60°$.

55
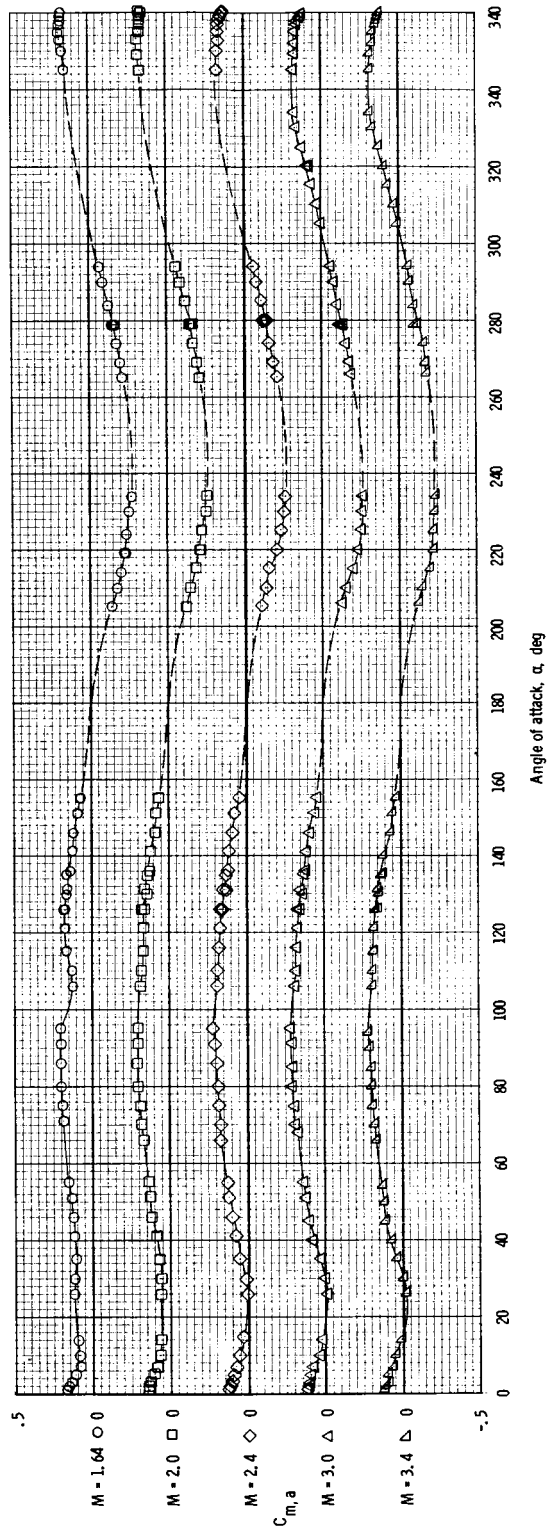
(b) Pitching-moment coefficient at $M = 1.64$ to 3.4.
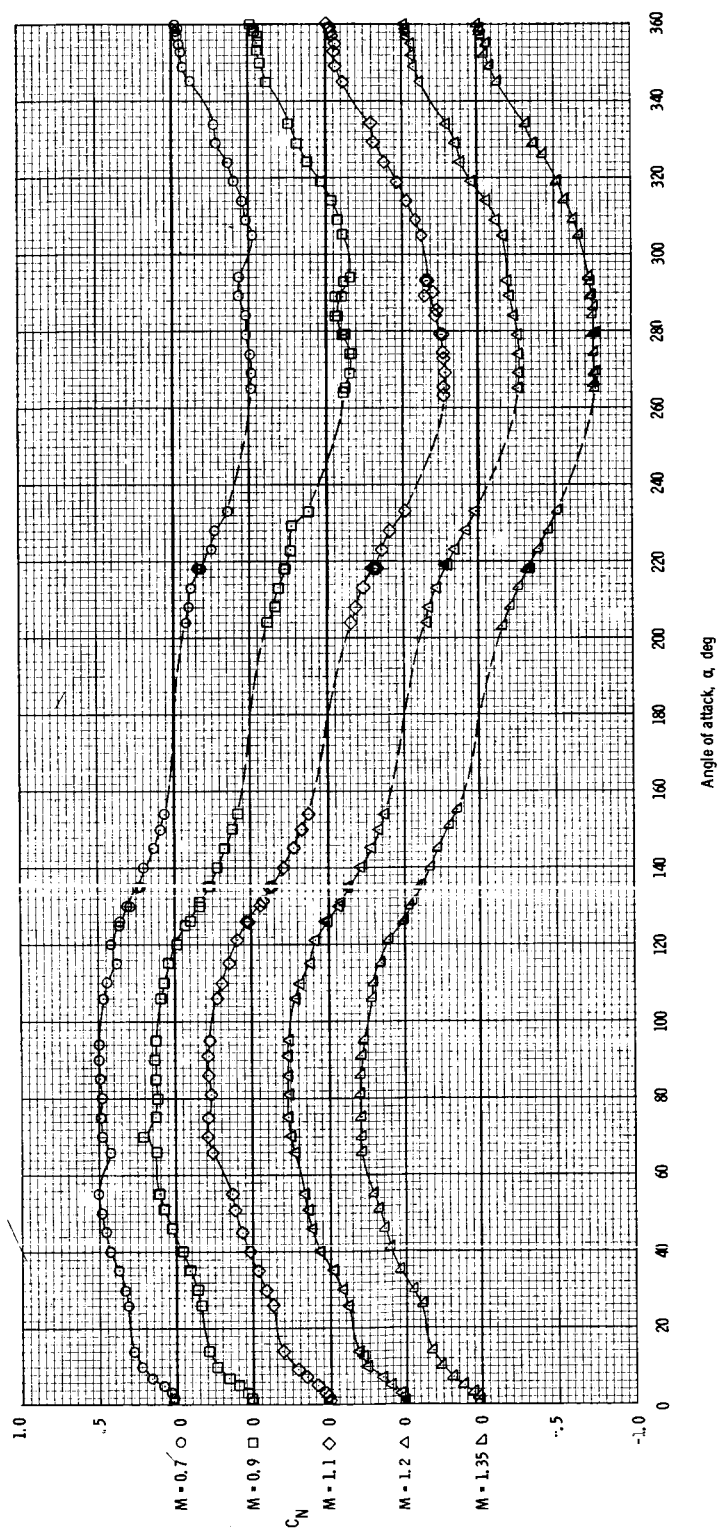
Figure 9. – Continued.

(c) Normal-force coefficient at M = 0.7 to 1.35.
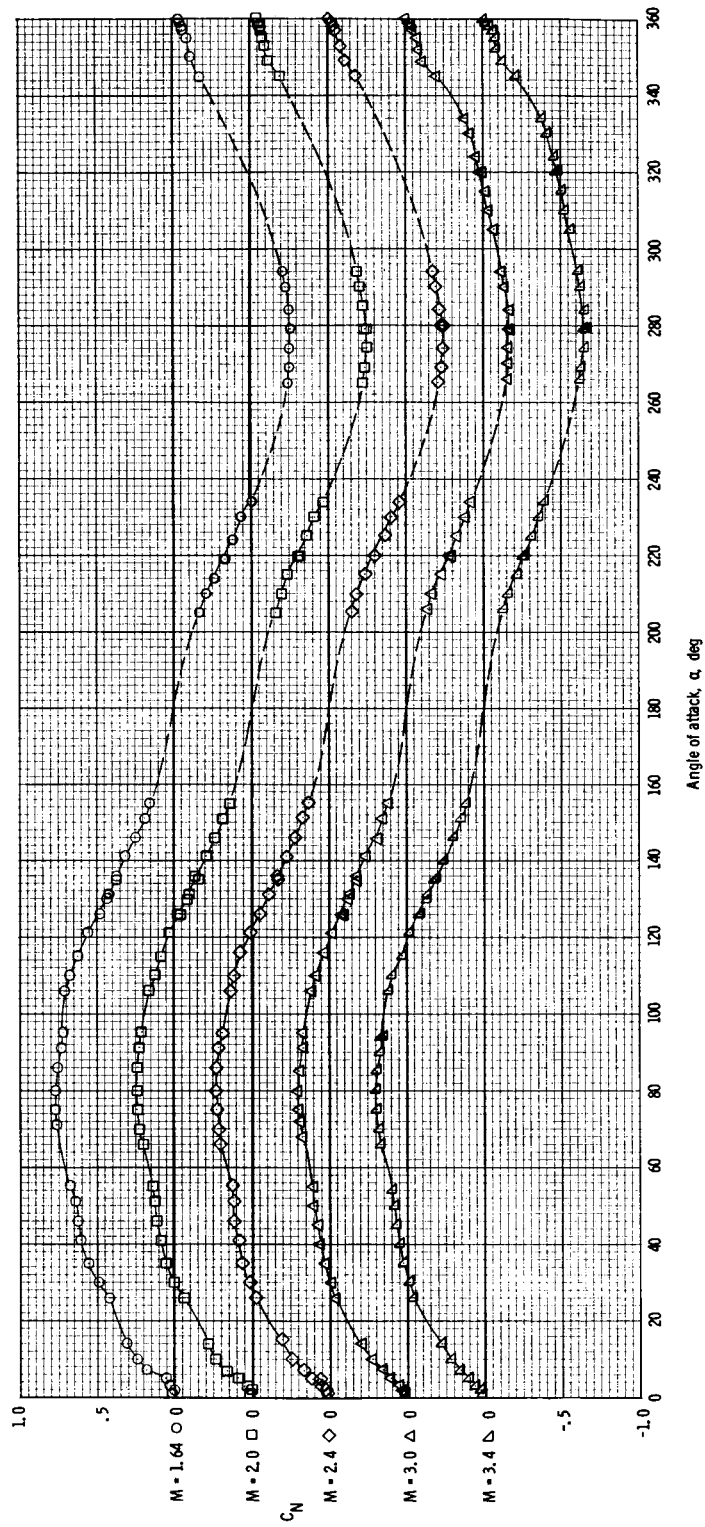
Figure 9. – Continued.

(d) Normal-force coefficient at M = 1.64 to 3.4.
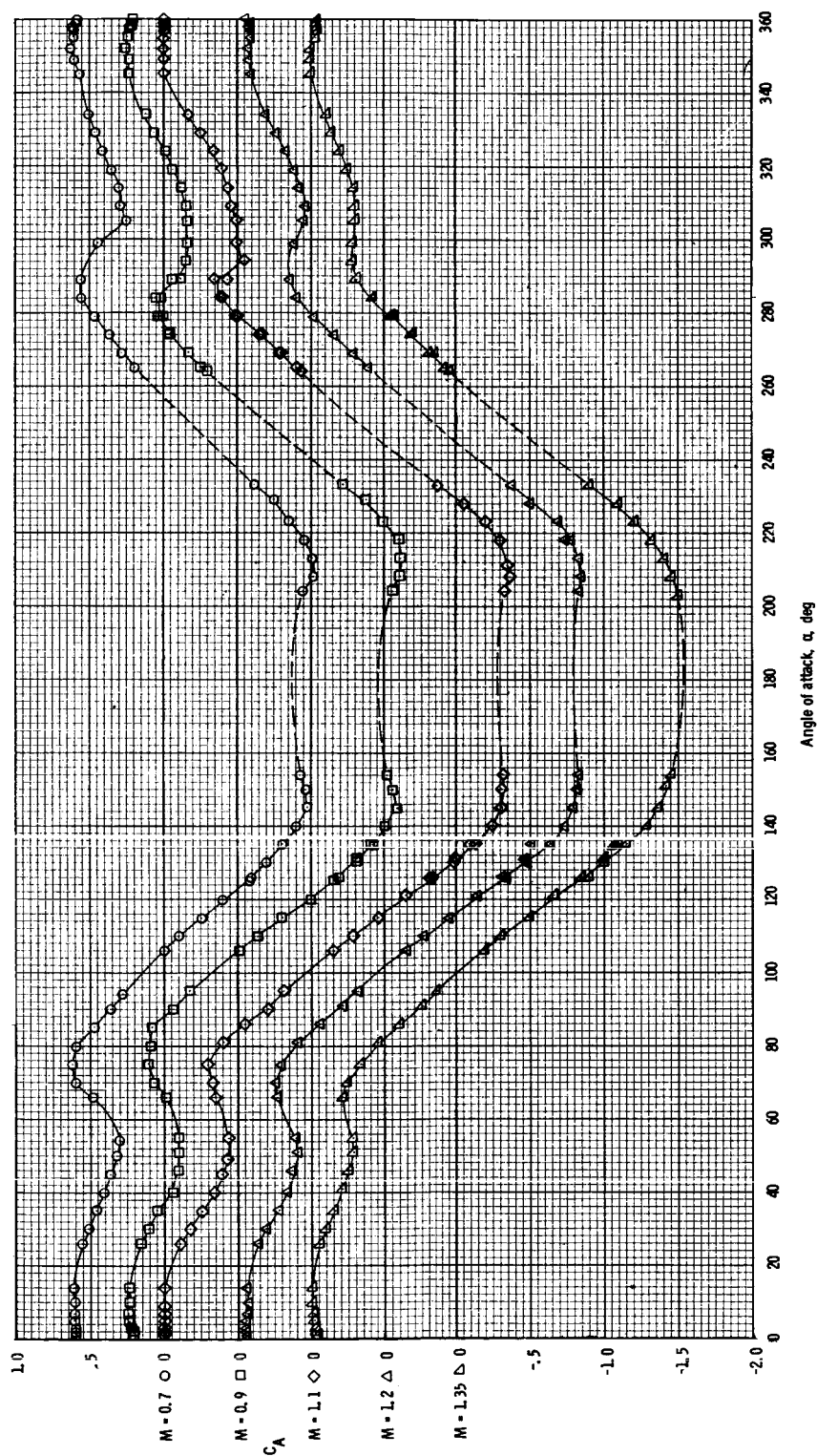
Figure 9. - Continued.

(e) Axial-force coefficient at M = 0.7 to 1.35.
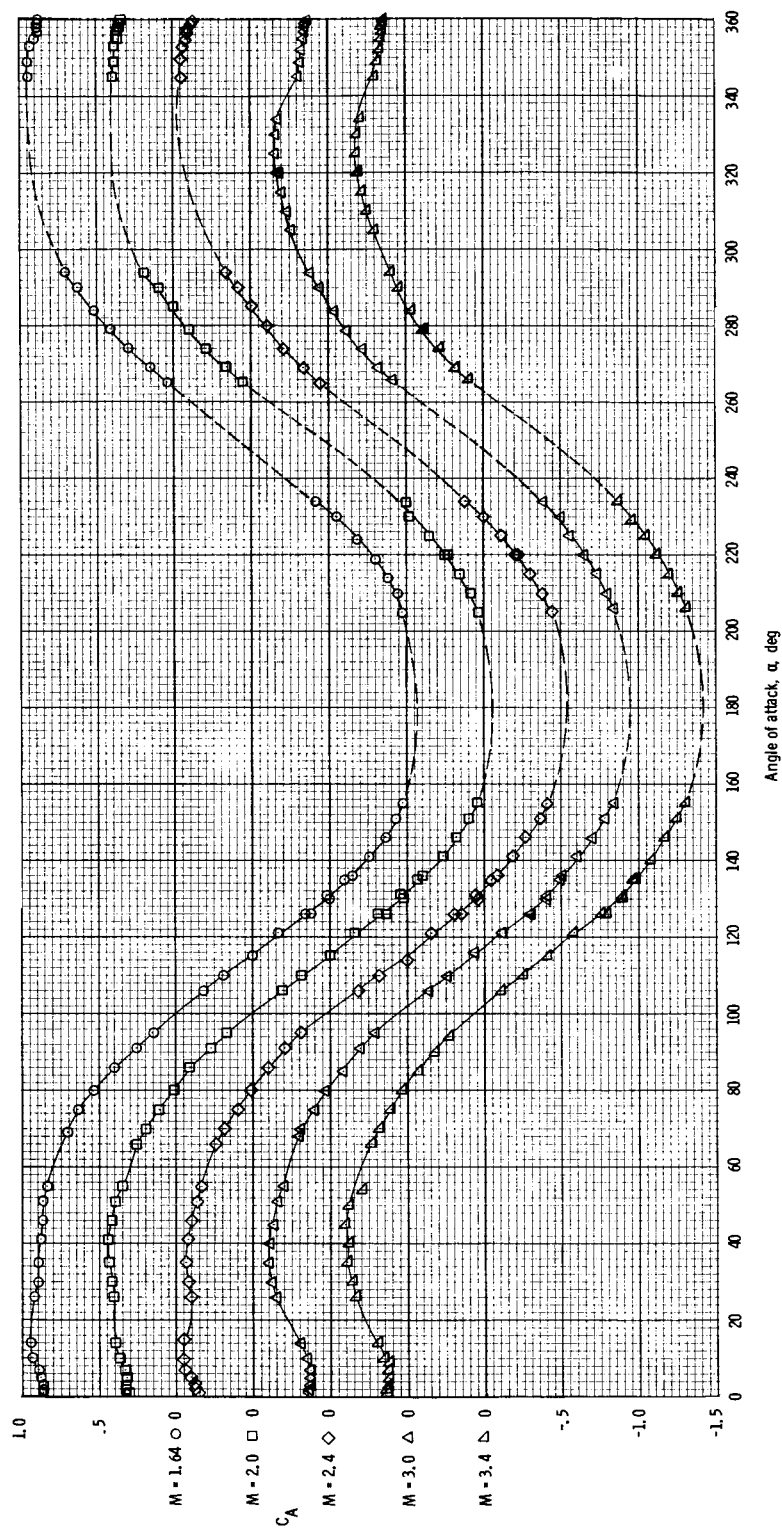
Figure 9. – Continued.

(f) Axial-force coefficient at M = 1.64 to 3.4.
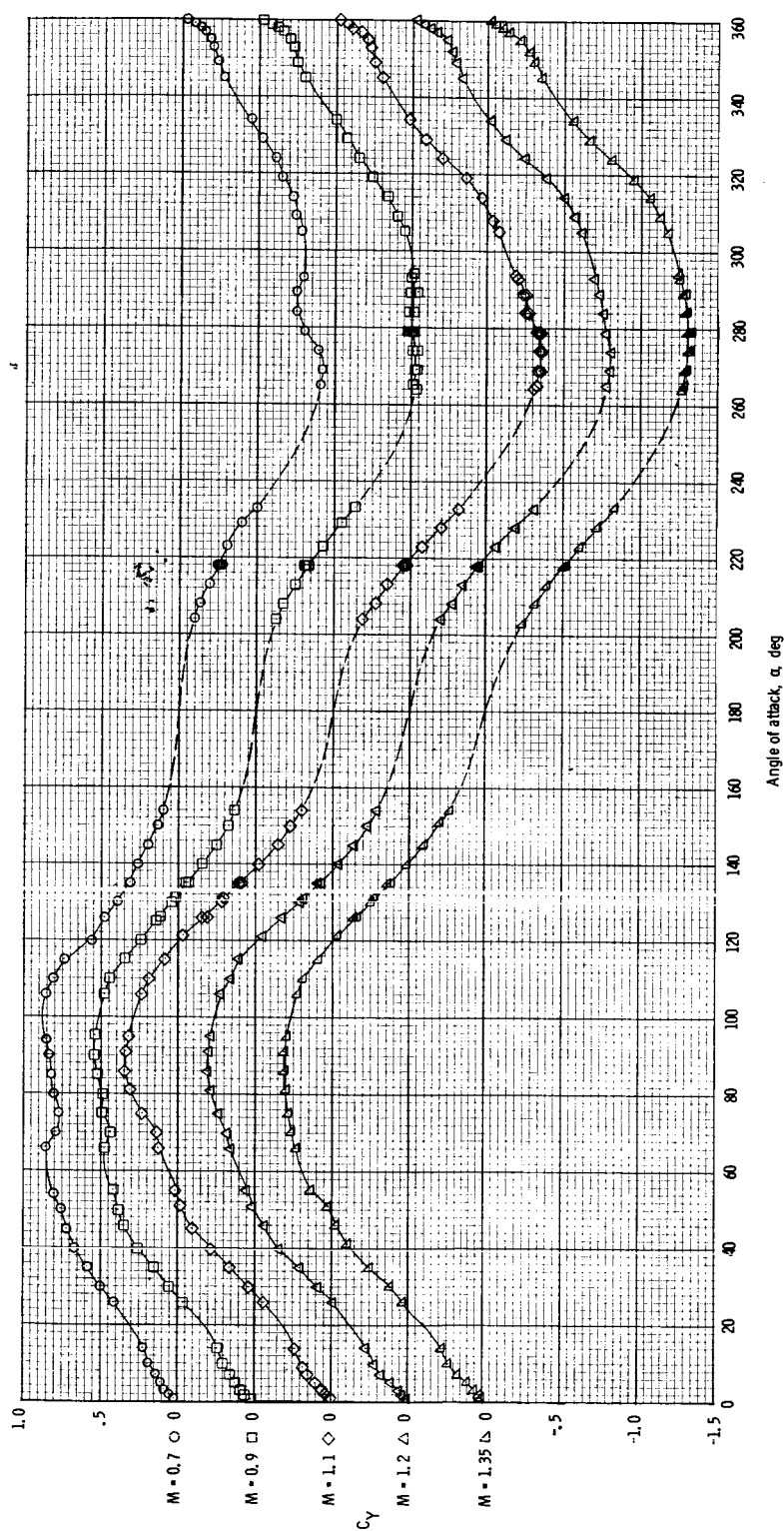
Figure 9. – Continued.

(g) Side-force coefficient at $M = 0.7$ to 1.35.

Figure 9. – Continued.

61
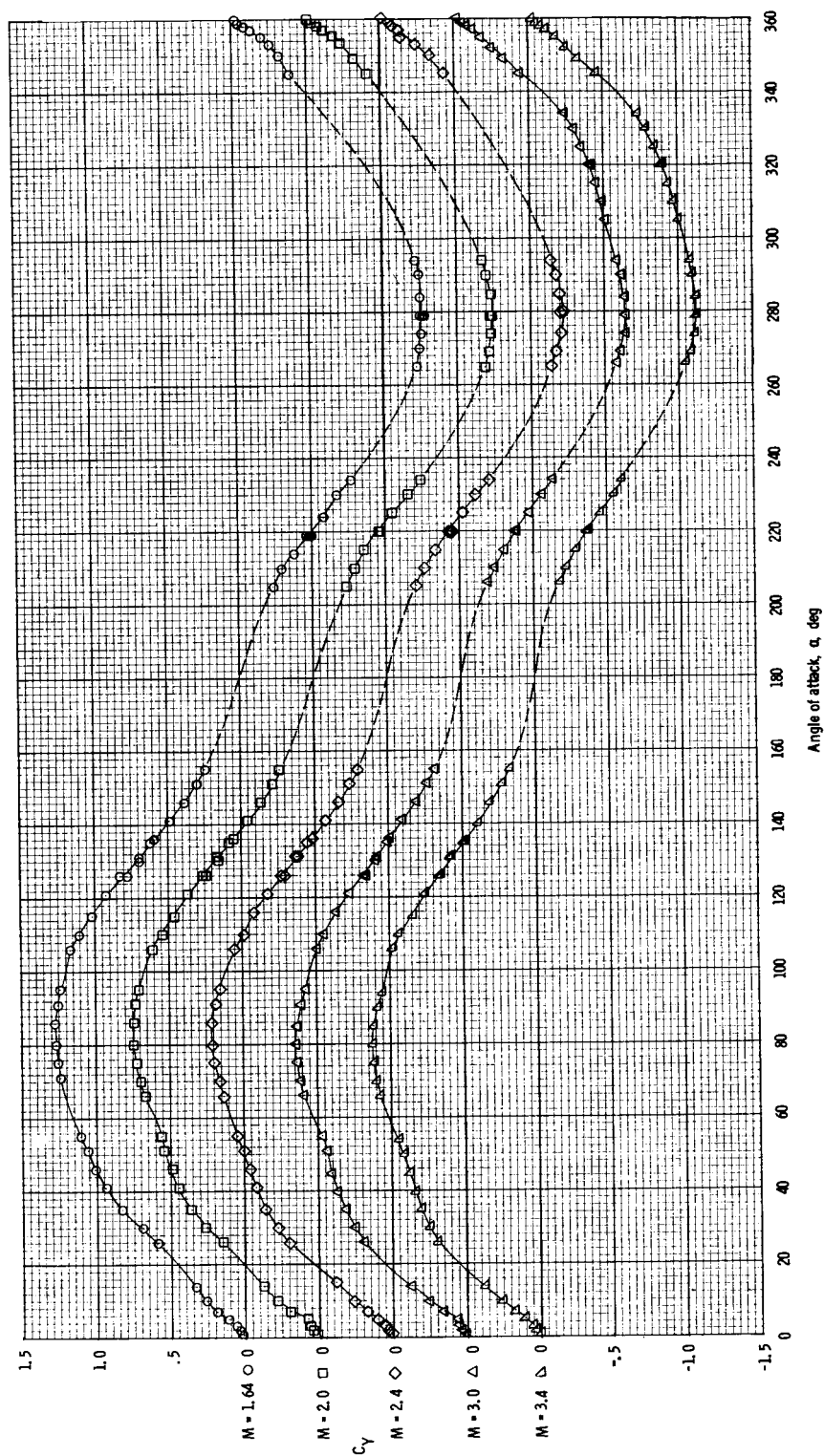
(h) Side-force coefficient at M = 1.64 to 3.4.
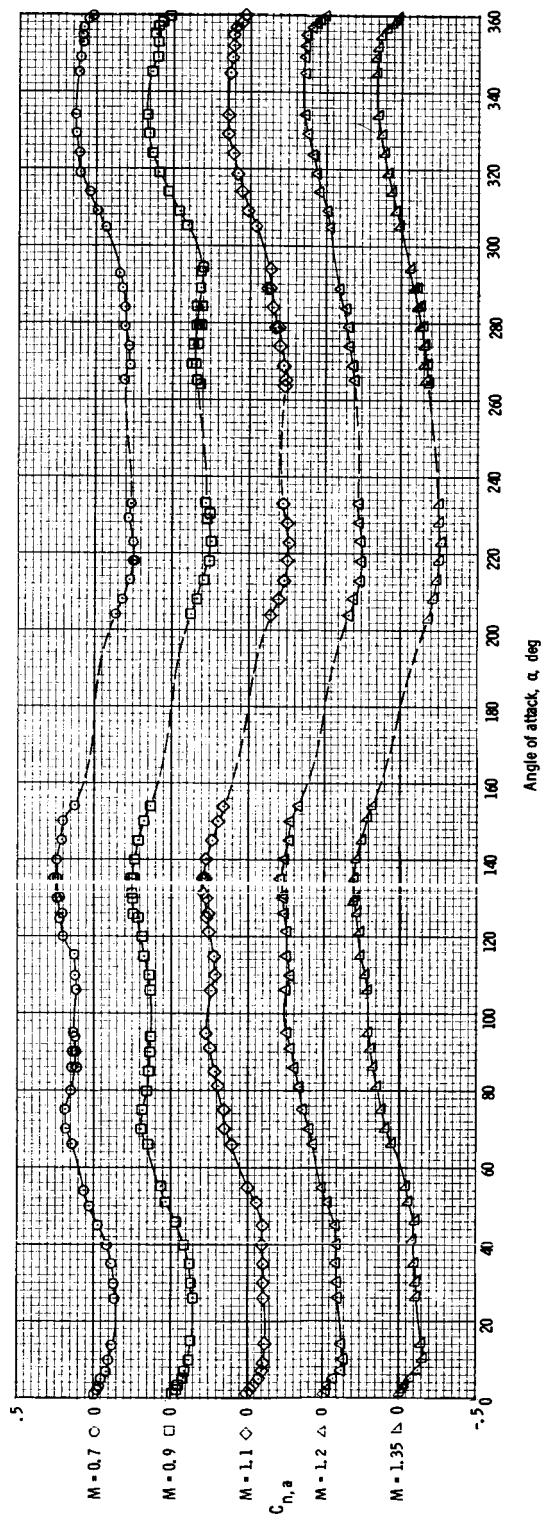
Figure 9. - Continued.
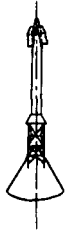
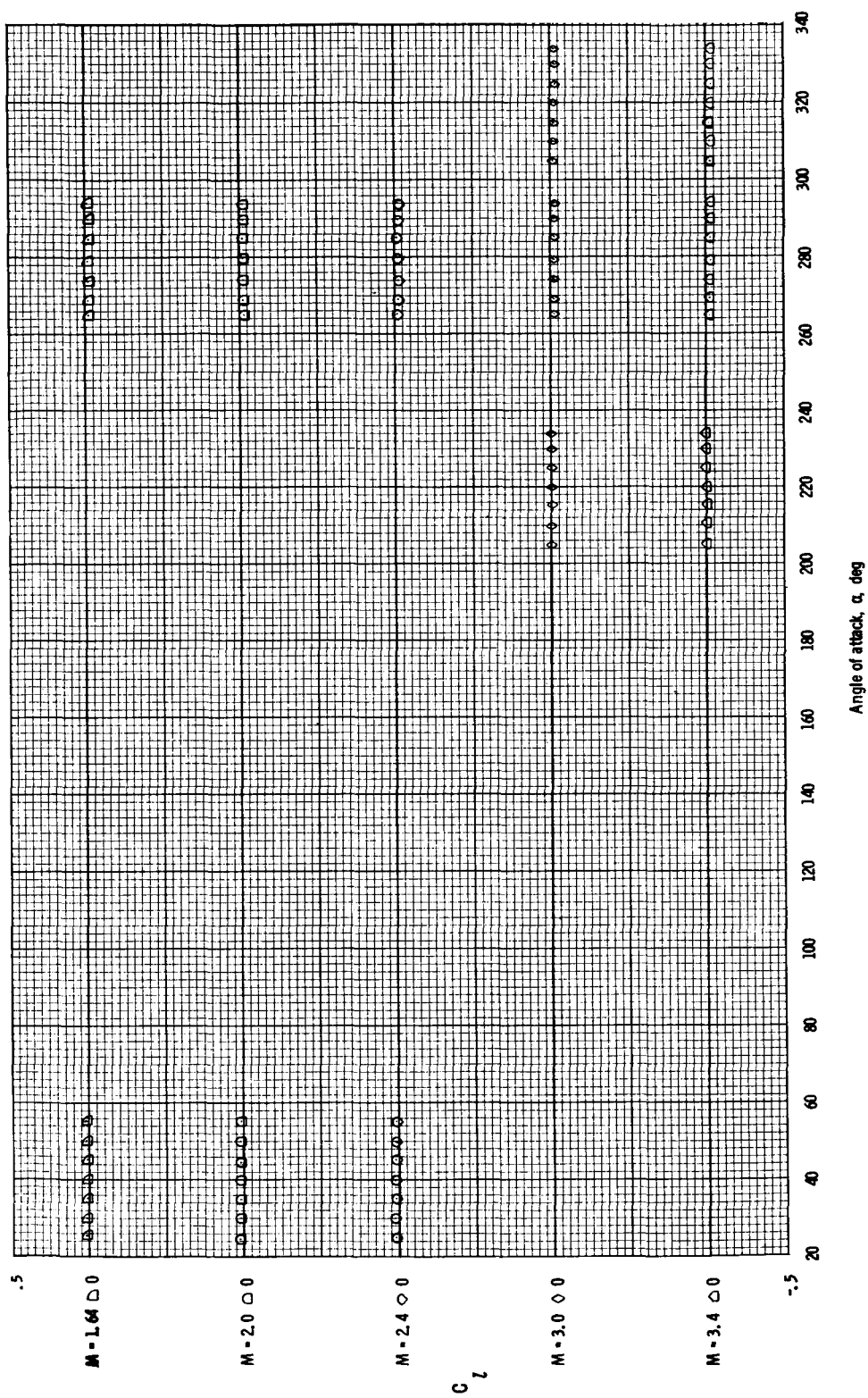(i) Yawing-moment coefficient at M = 0.7 to 1.35.

Figure 9. – Continued.

(j) Yawing-moment coefficient at M = 1.64 to 3.4.

Figure 9. - Continued.

(k) Rolling-moment coefficient at M = 0.7 to 1.35.

Figure 9. – Continued.

65
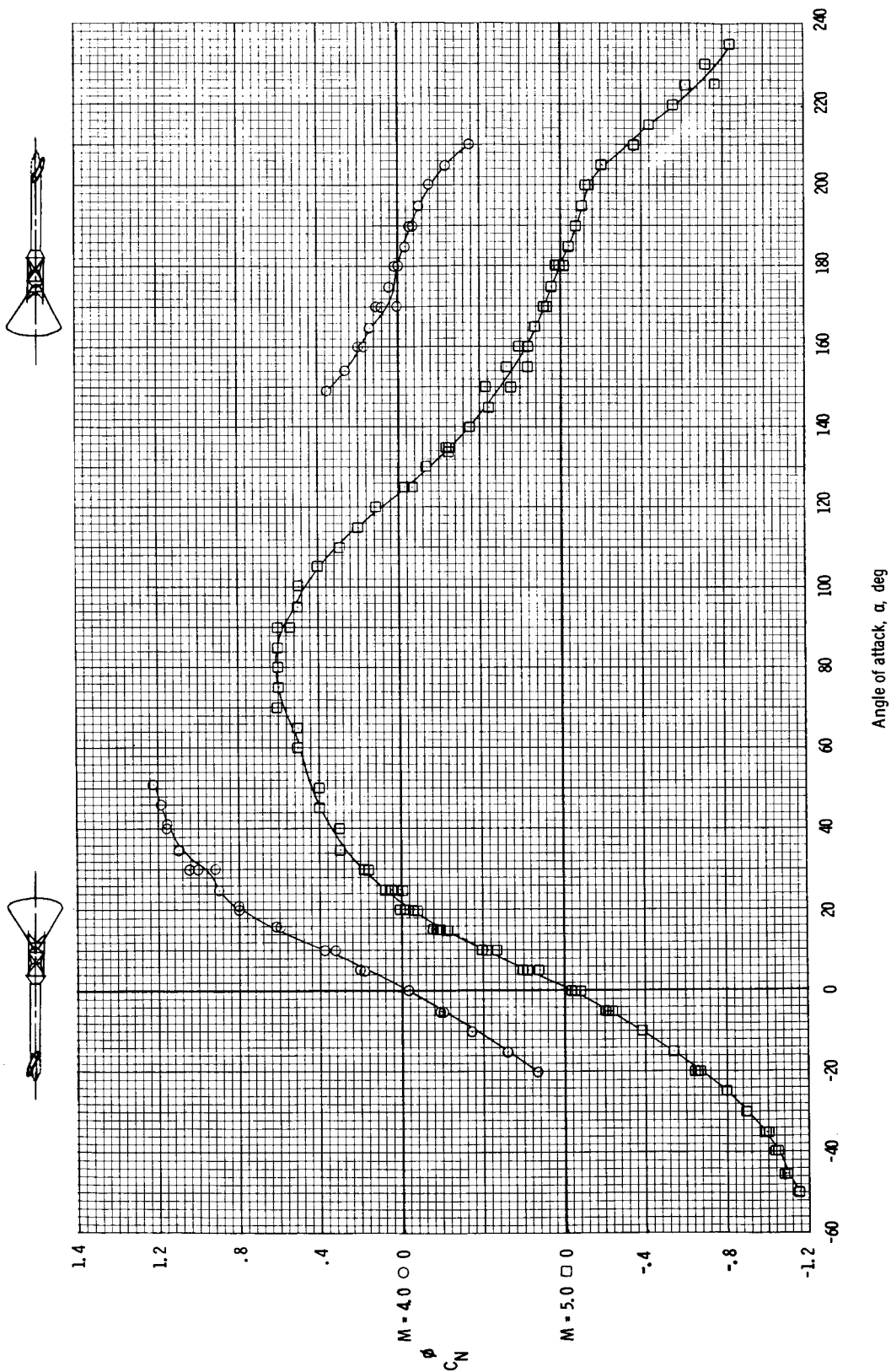
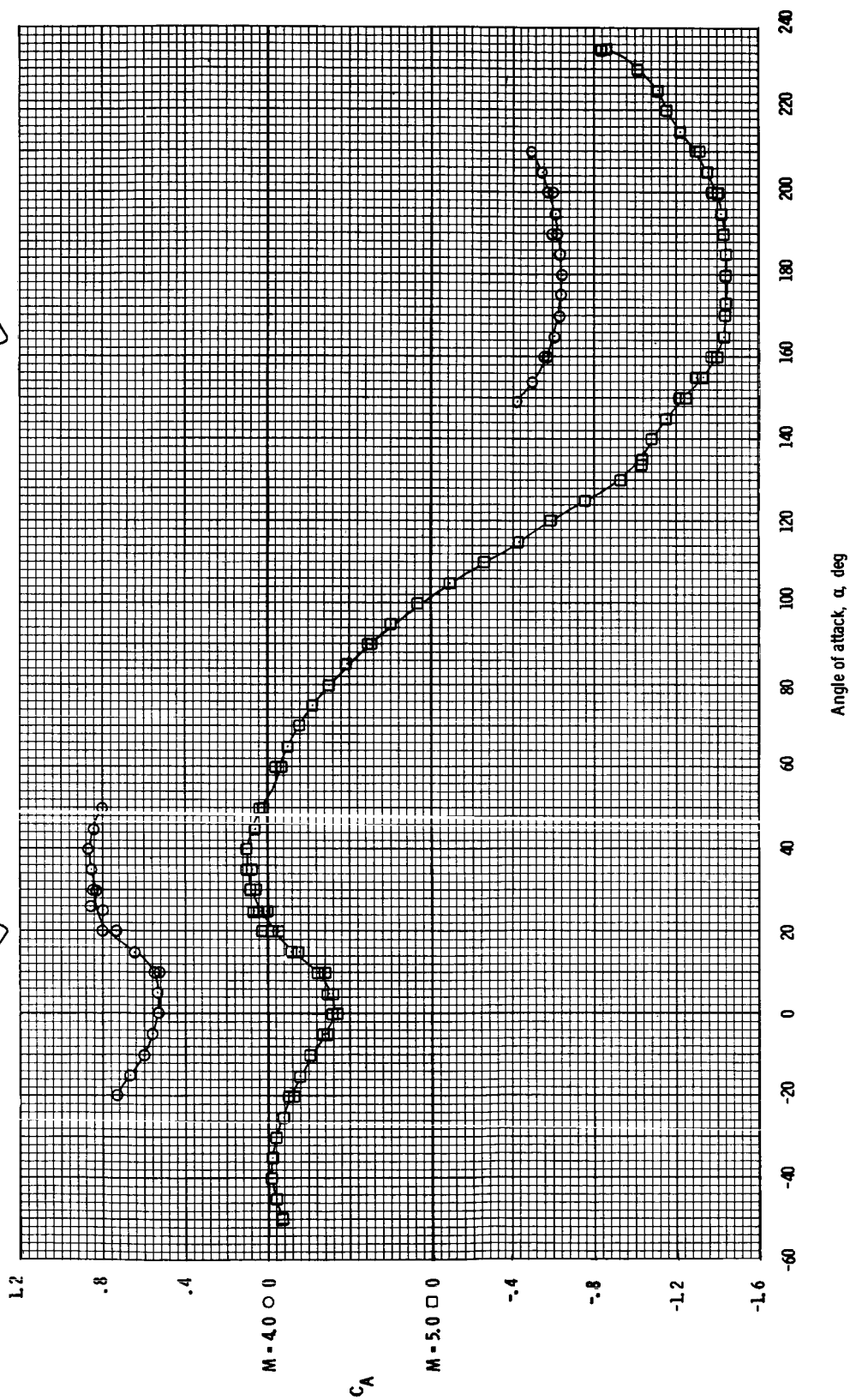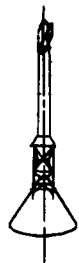(l) Rolling-moment coefficient at $M = 1.64$ to 3.4.

Figure 9. - Concluded.

(a) Pitching-moment coefficient at $M = 0.7$ to 1.35.

Figure 10. – Aerodynamic characteristics of the Apollo launch escape vehicle with canard surfaces deployed, at $M = 0.7$ to 3.4, with $\phi = -90°$.
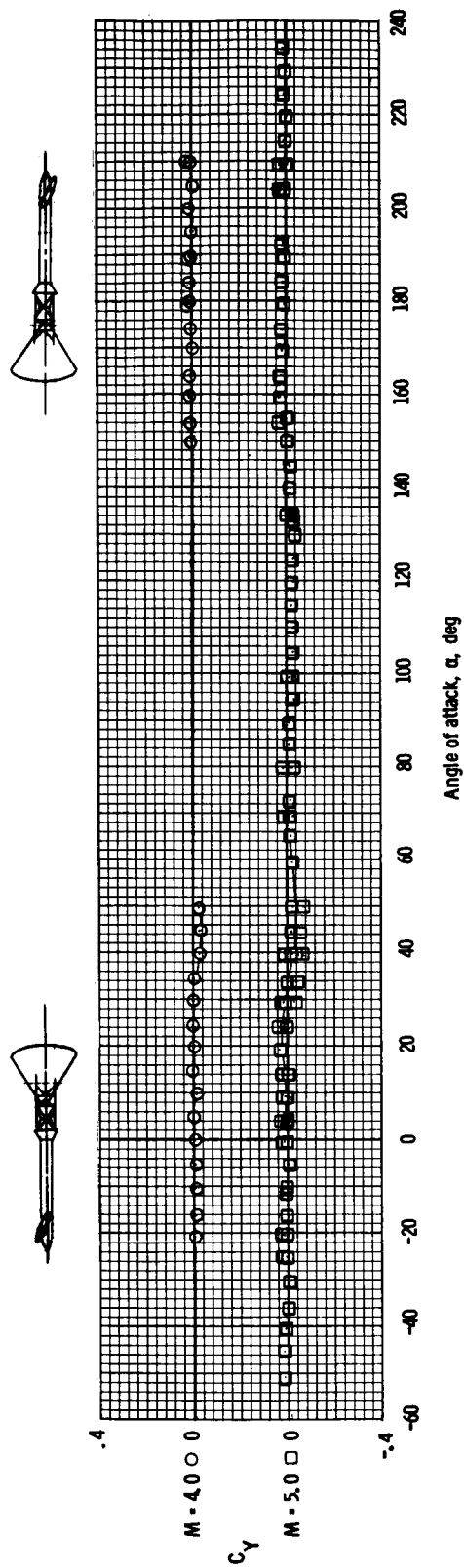
(b) Pitching-moment coefficient at M = 1.63 to 3.4.

Figure 10. - Continued.

(c) Normal-force coefficient at M = 0.7 to 1.35.

Figure 10. – Continued.

(d) Normal-force moment coefficient at M = 1.63 to 3.4.

Figure 10. – Continued.

(e) Axial-force coefficient at M = 0.7 to 1.35.

Figure 10. – Continued.

(f) Axial-force coefficient at M = 1.63 to 3.4.

Figure 10. – Continued.

(g) Side-force coefficient at M = 0.7 to 1.35.

Figure 10. - Continued.

73

(h) Side-force coefficient at M = 1.63 to 3.4.

Figure 10. - Continued.

(i) Yawing-moment coefficient at $M = 0.7$ to 1.35.

Figure 10. – Continued.

(j) Yawing-moment coefficient at M = 1.63 to 3.4.

Figure 10. - Continued.

(k) Rolling-moment coefficient at M = 0.7 to 1.35.

Figure 10. – Continued.

(l) Rolling-moment coefficient at M = 1.63 to 3.4.

Figure 10. - Concluded.
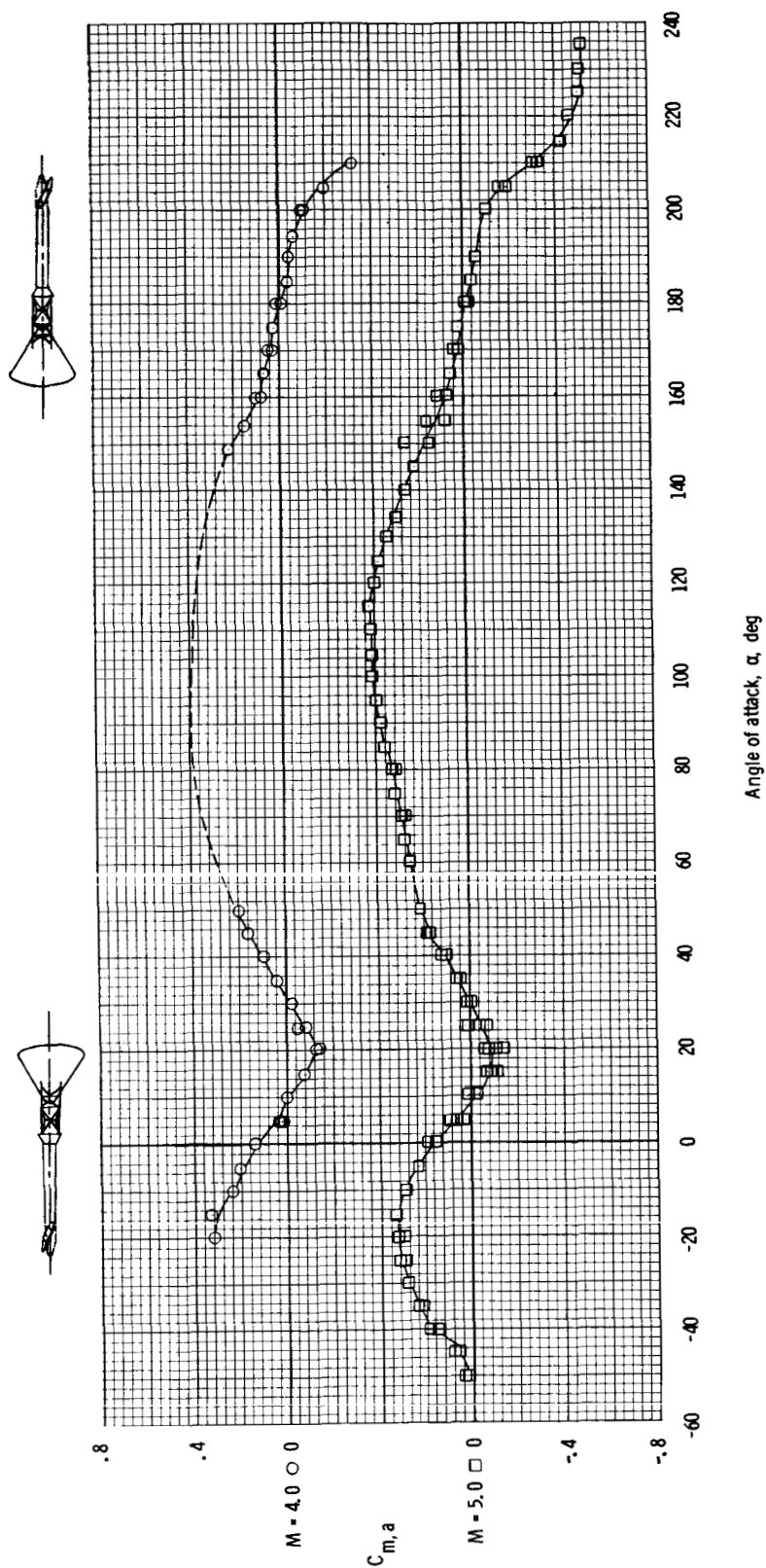
(a) Pitching-moment coefficient.

Figure 11.- Aerodynamic characteristics of the Apollo launch escape vehicle with canard surfaces deployed, at $M = 4.0$ and 5.0, with $\phi = 0°$.

Angle of attack, α, deg

(b) Normal-force coefficient.
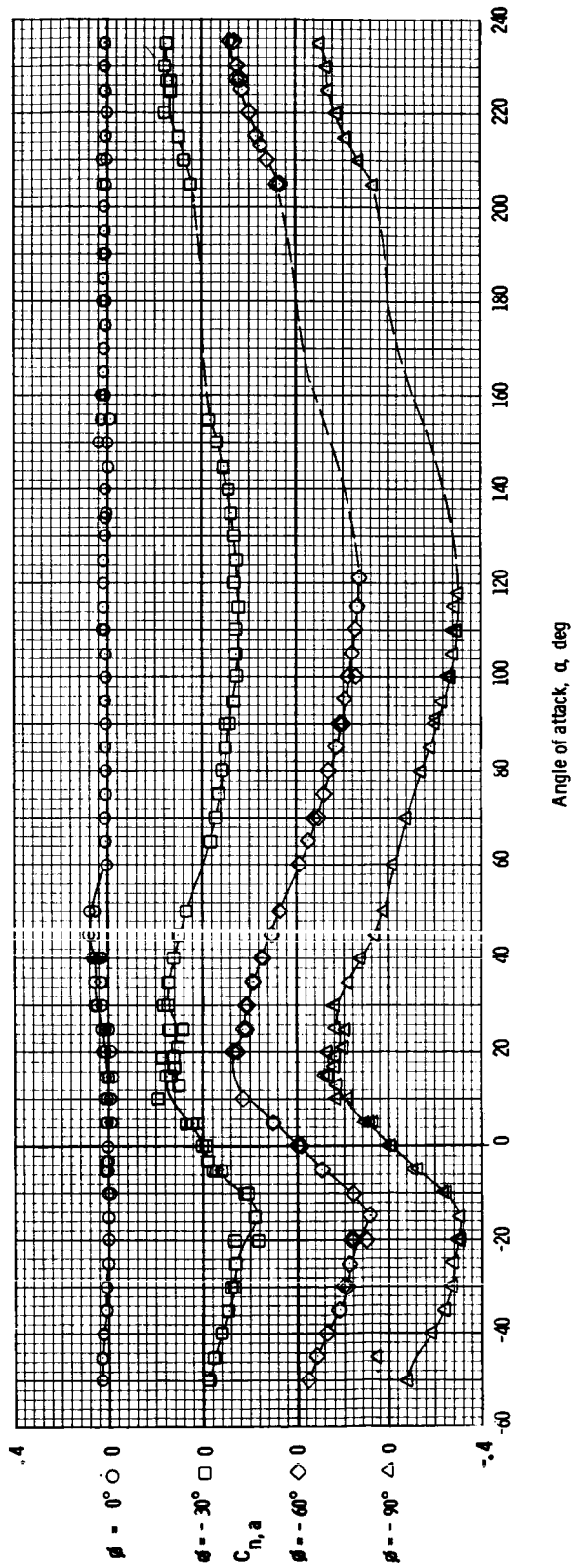
Figure 11. – Continued.

(c) Axial-force coefficient.

Figure 11. - Continued.

(d) Side-force coefficient.

Figure 11. – Continued.
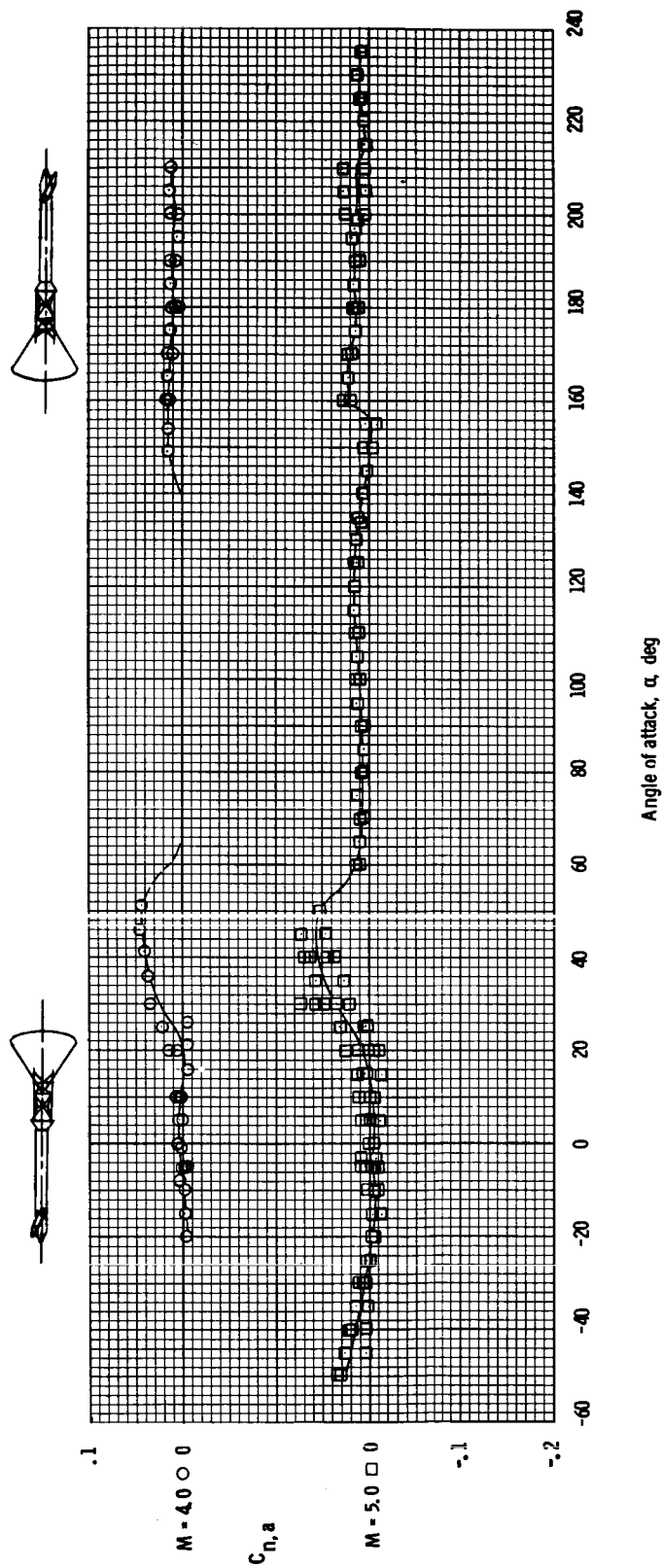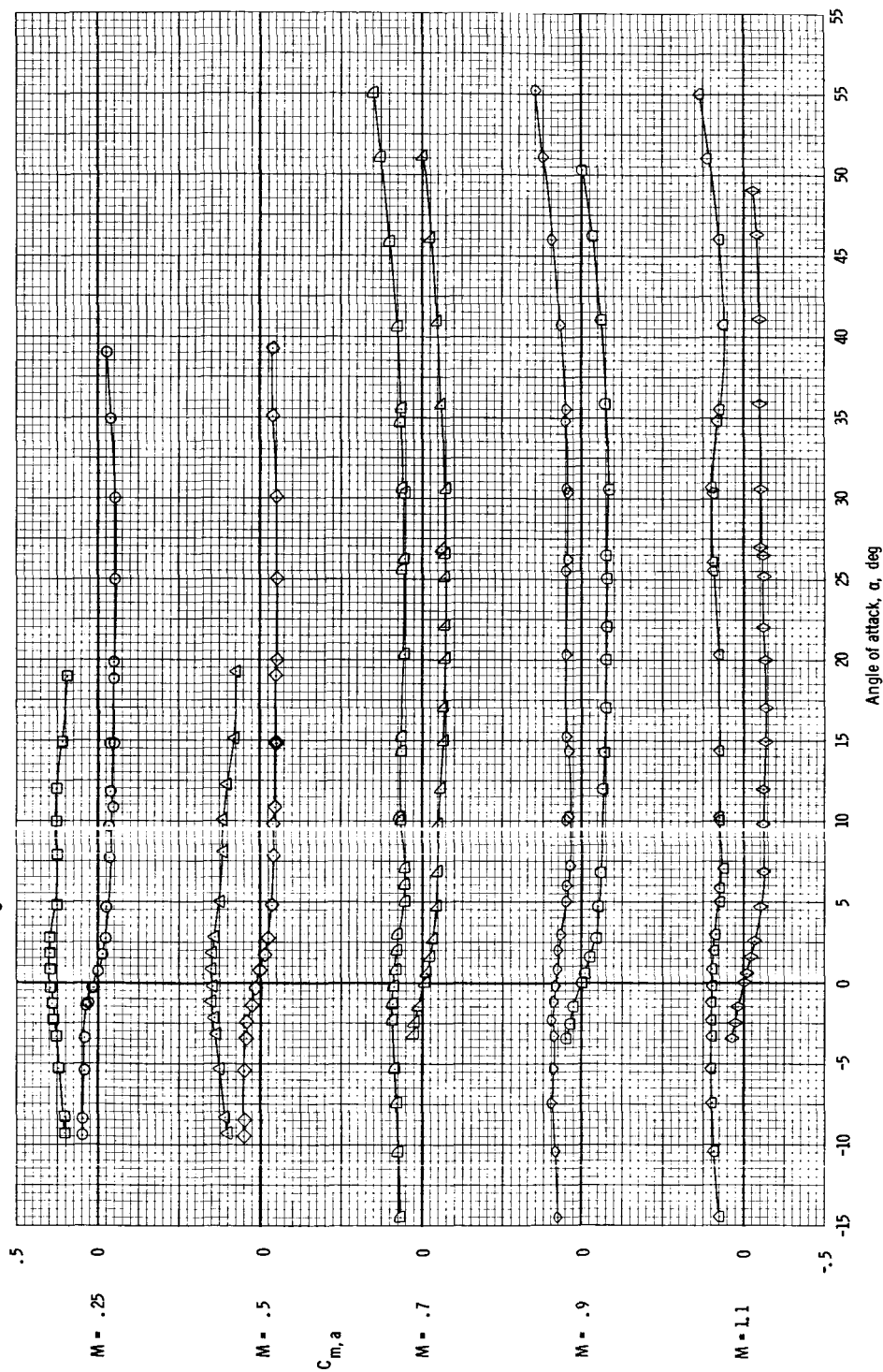
(e) Yawing-moment coefficient.

Figure 11. – Continued.
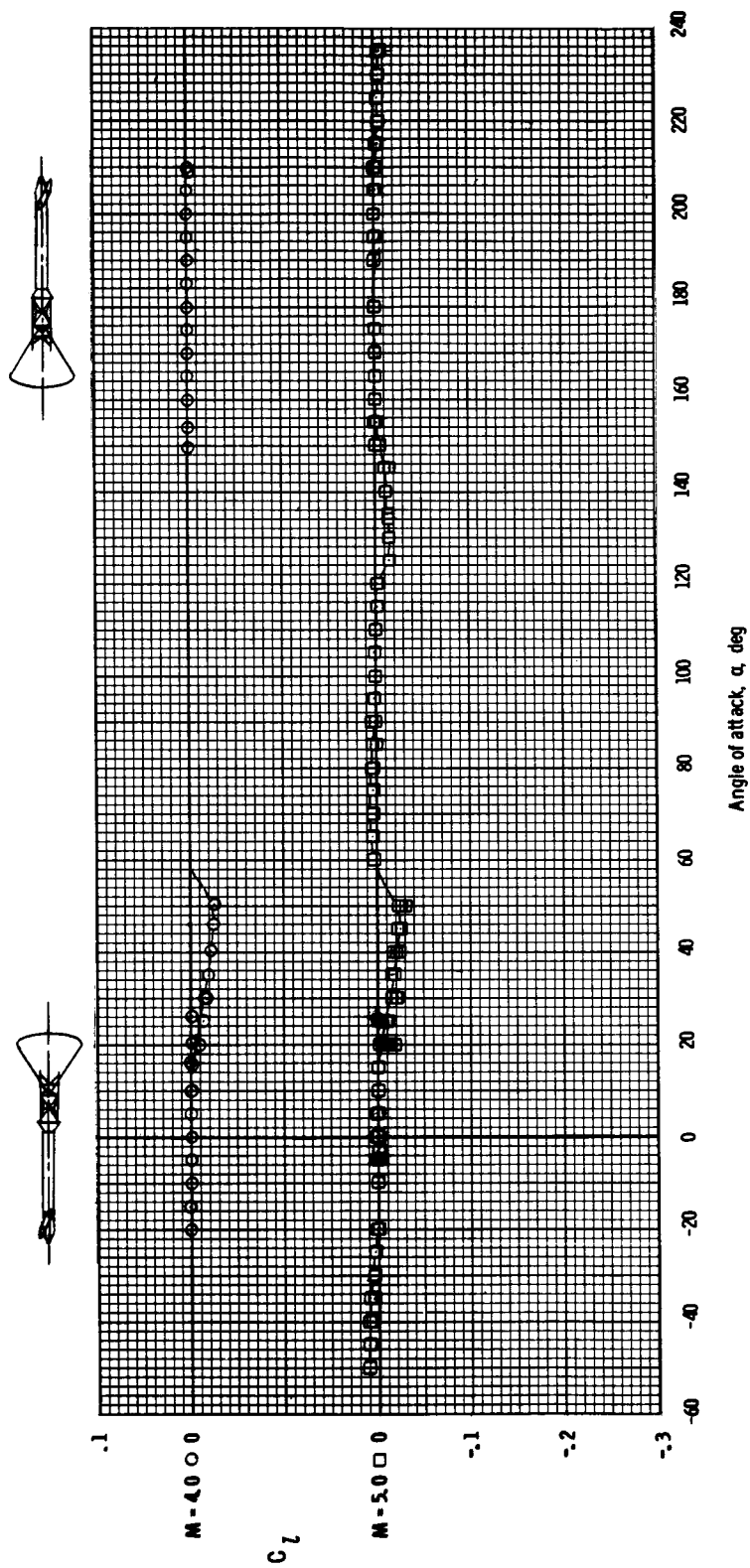
(f) Rolling-moment coefficient.

Figure 11. – Concluded.
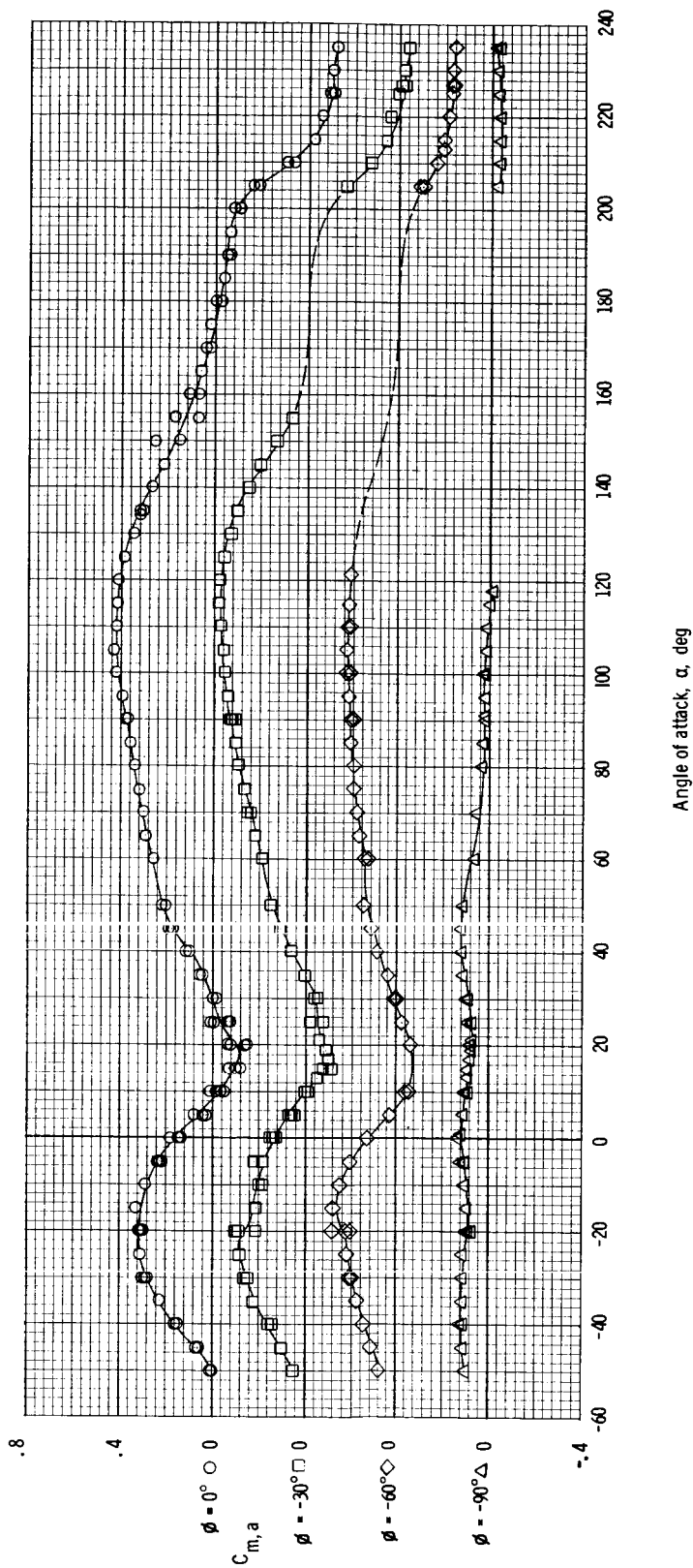
(a) Pitching-moment coefficient.

Figure 12. – Effect of canard roll angle ϕ on the aerodynamic characteristics of the Apollo launch escape vehicle with canard surfaces deployed, at $M = 5.0$.
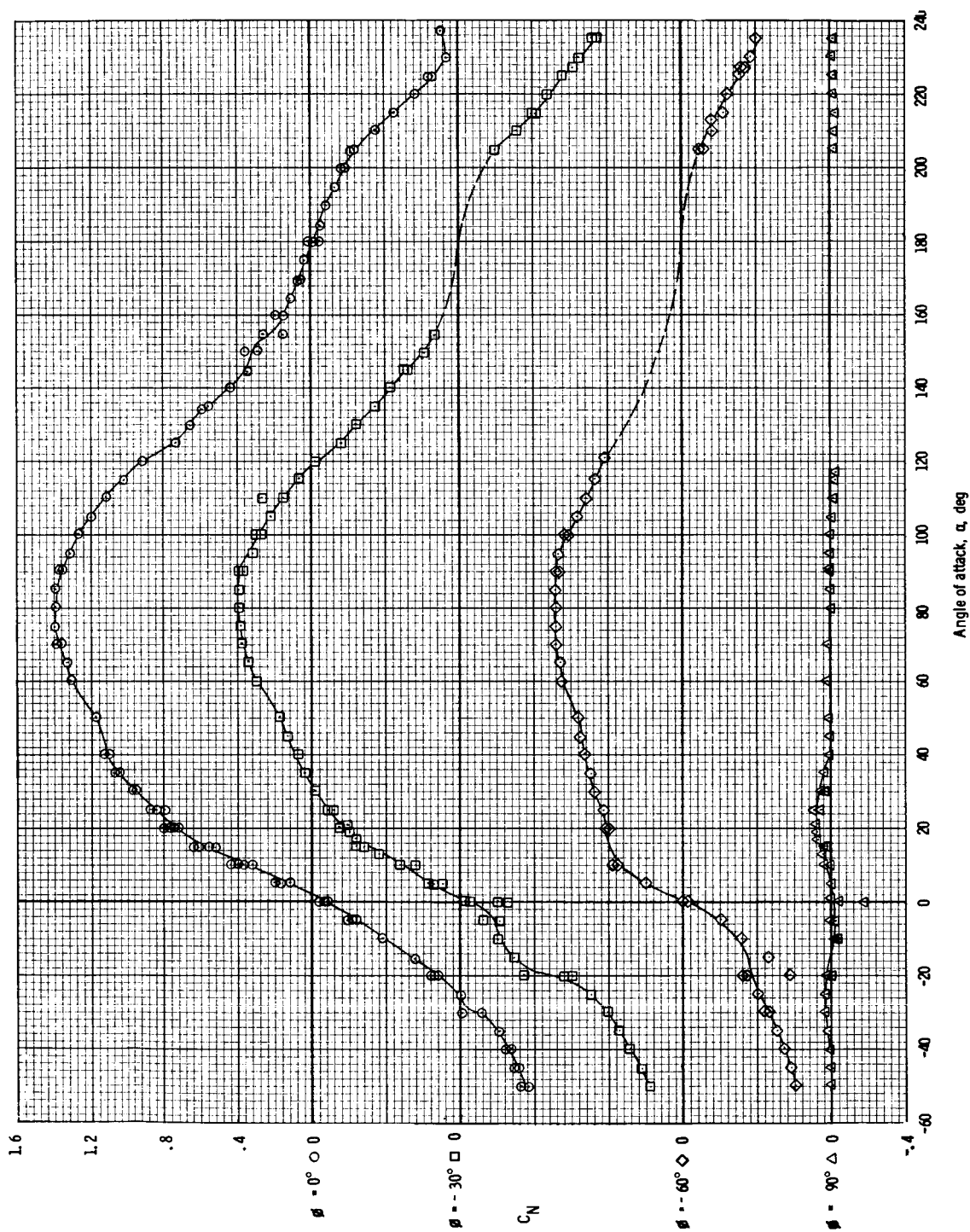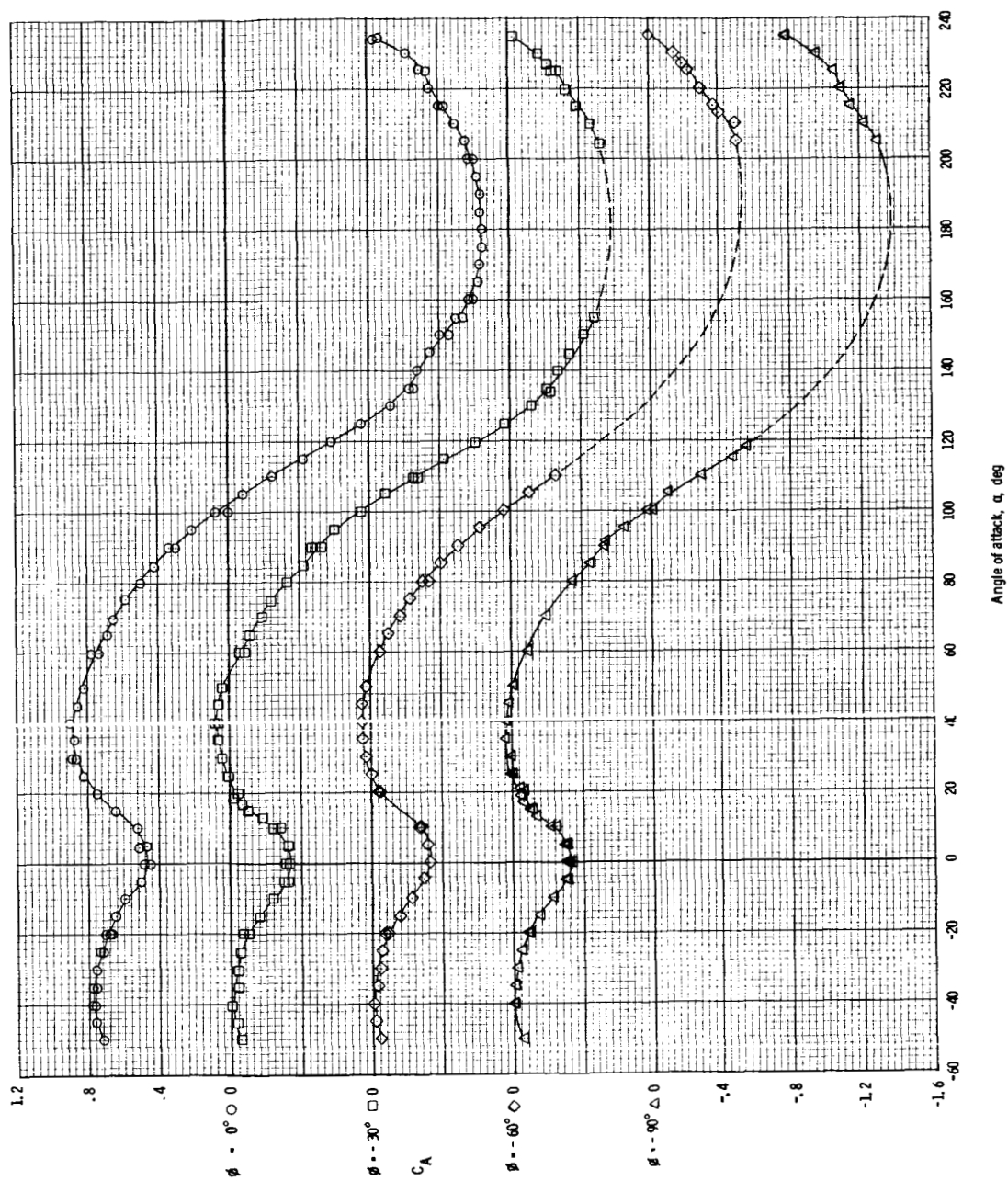
85

(b) Normal-force coefficient.

Figure 12. – Continued.

86

(c) Axial-force coefficient.

Figure 12. – Continued.

Angle of attack, α, deg

(d) Side-force coefficient.

Figure 12. – Continued.

88

Angle of attack, α, deg
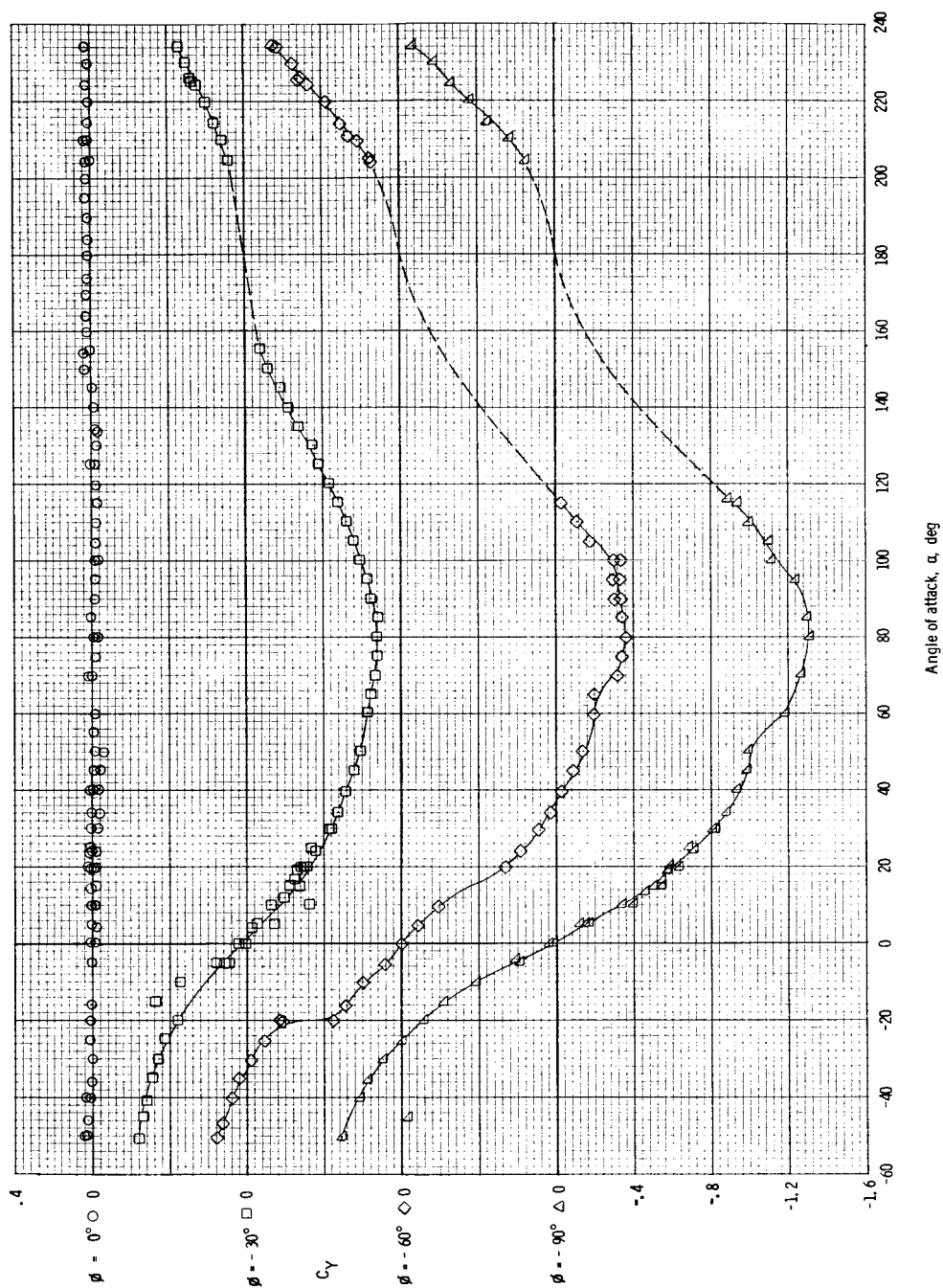
(e) Yawing-moment coefficient.

Figure 12. – Continued.
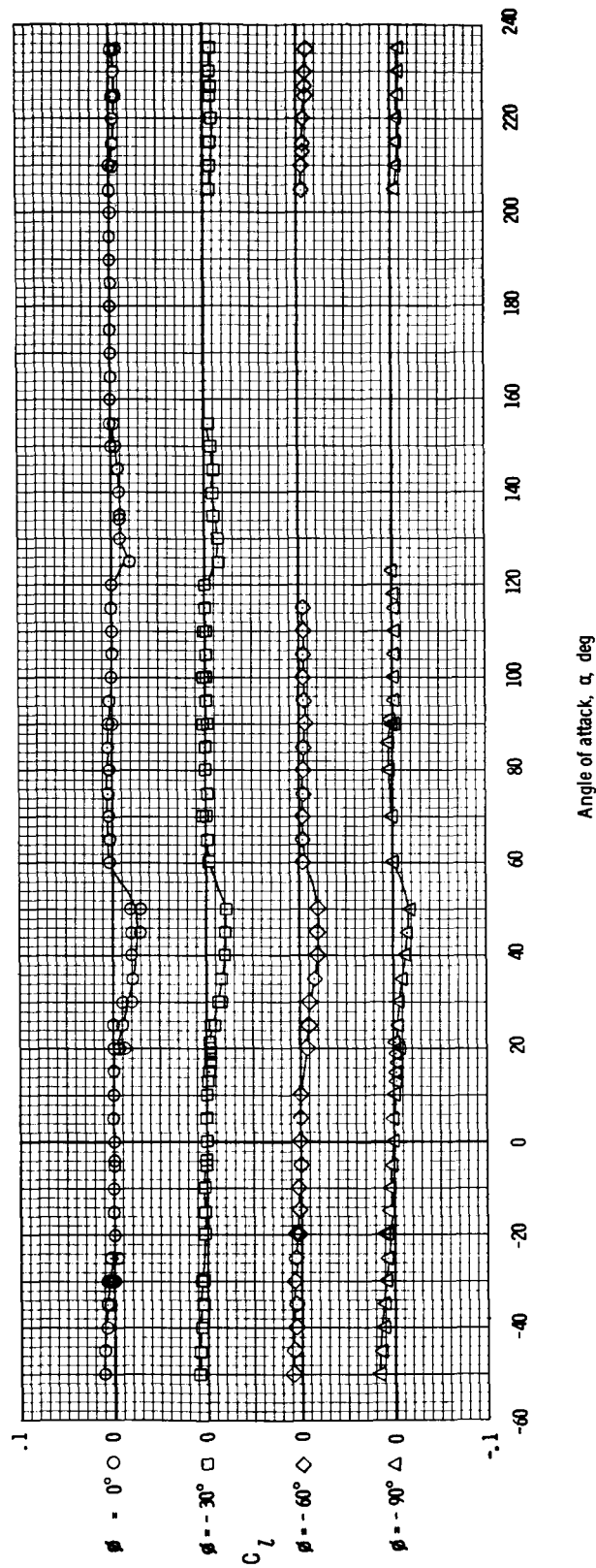
(f) Rolling-moment coefficient.

Figure 12. – Concluded.

(a) Pitching-moment coefficient at M = 0.25 to 1.1.

Figure 13. – Pitching-moment coefficients of the Apollo launch escape vehicle without canards, compared with pitching-moment coefficients of the launch escape vehicle with canards deployed, $\phi = 0°$.
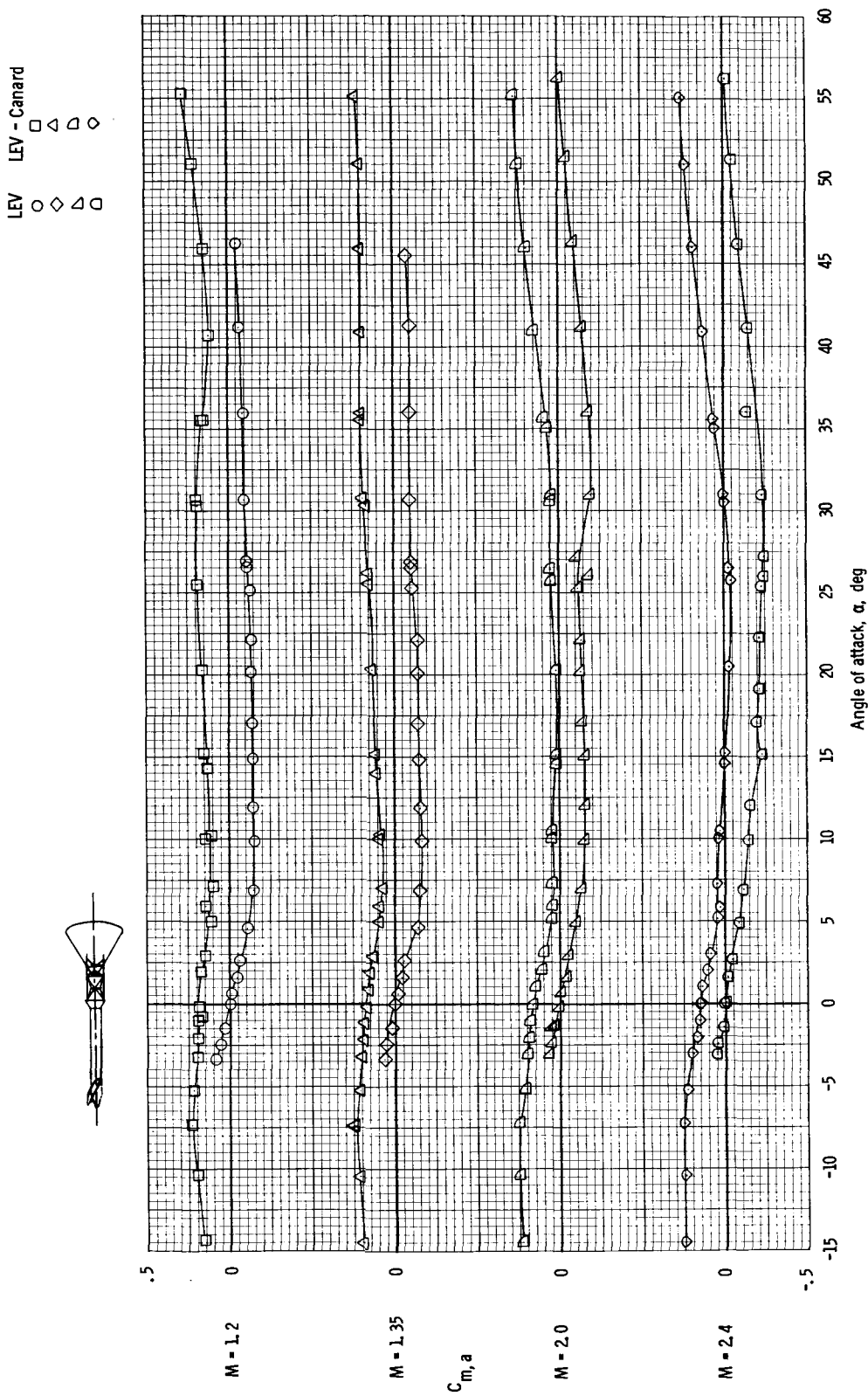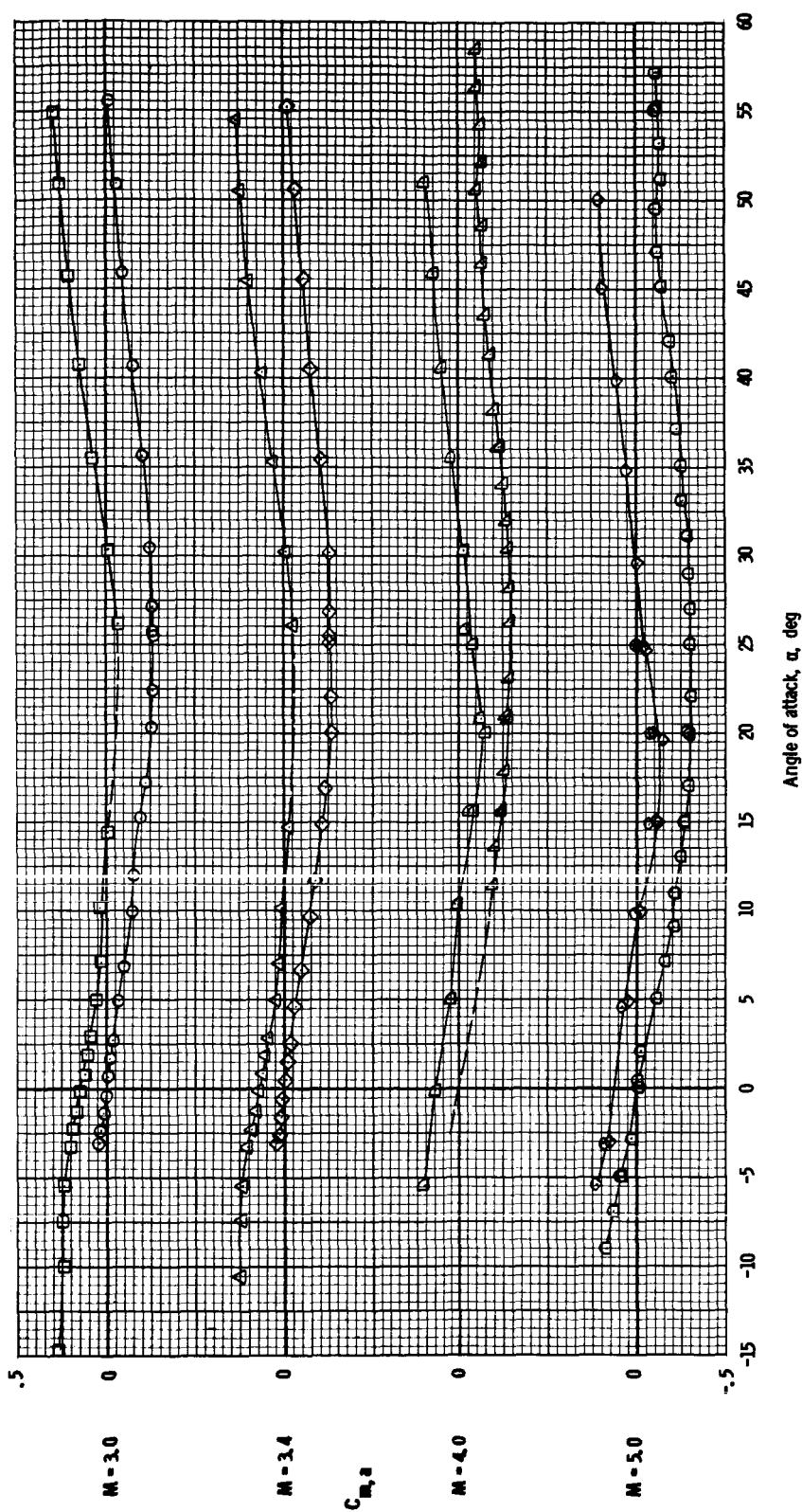
(b) Pitching-moment coefficient at M = 1.2 to 2.4.

Figure 13. – Continued.

(c) Pitching-moment coefficient at M = 3.0 to 5.0.
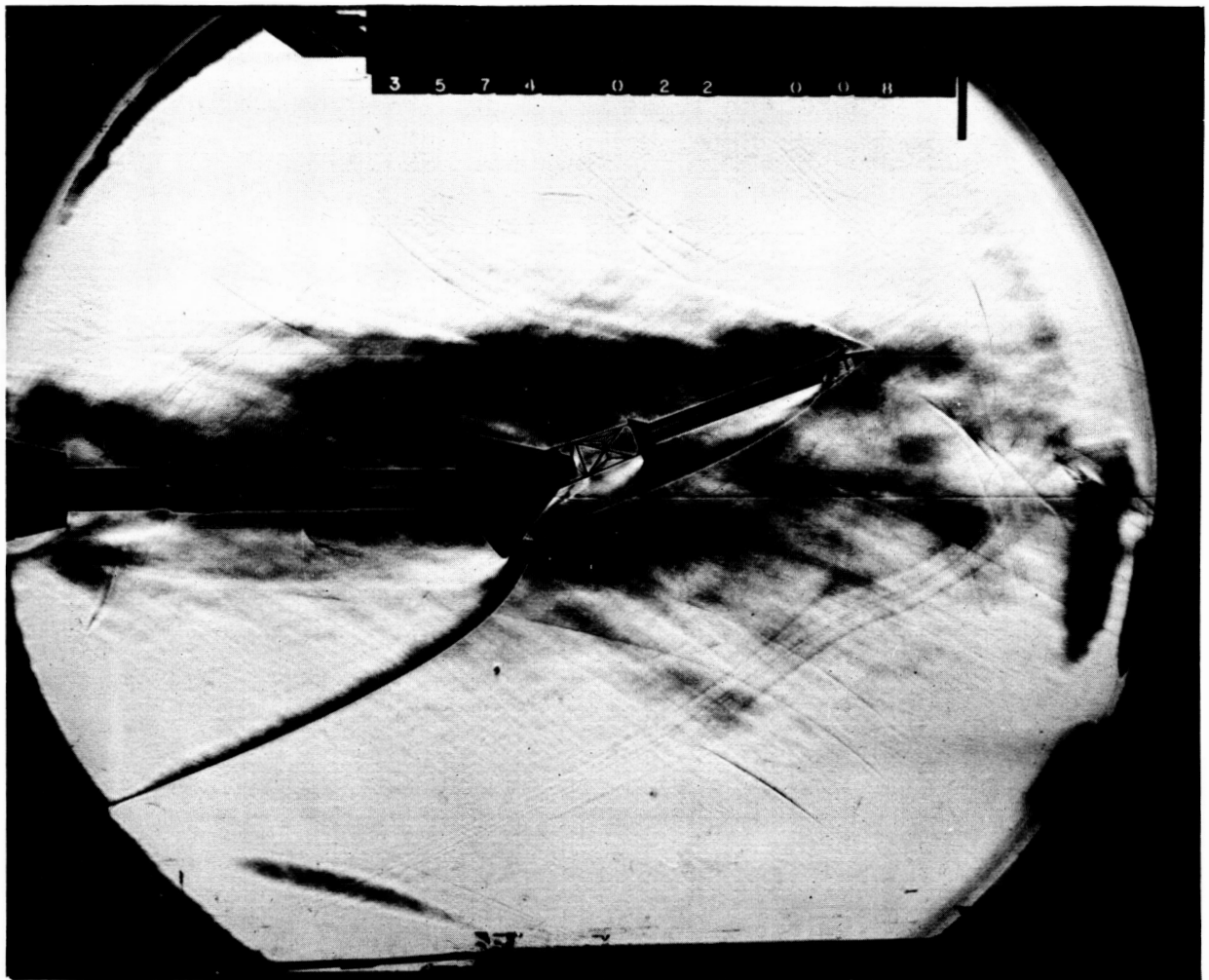
Figure 13. – Concluded.

Figure 14. - Schlieren photograph of the post-abort configuration showing a shock wave impinging on the lower surface of the command module, $\alpha \approx 20°$, M = 5.0.
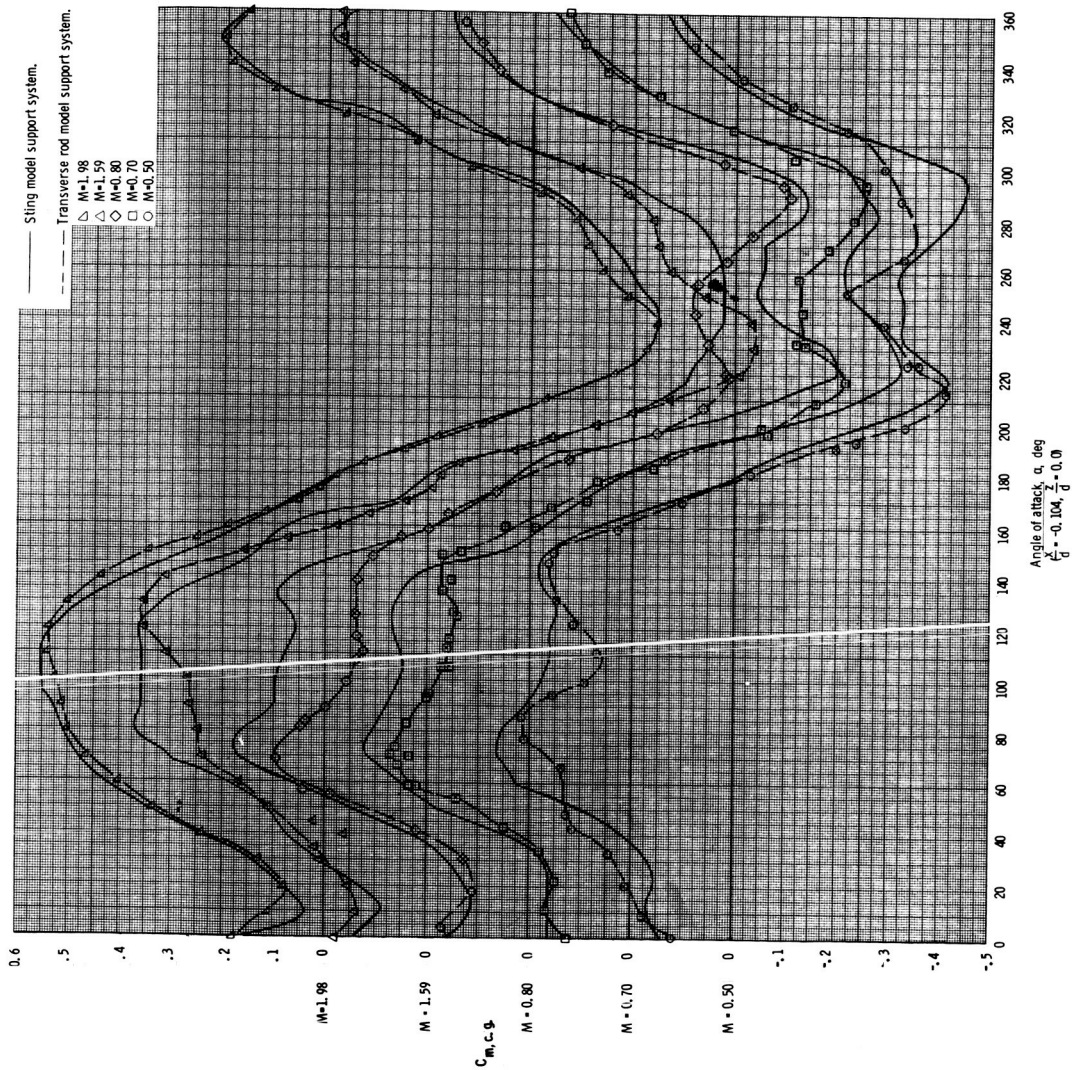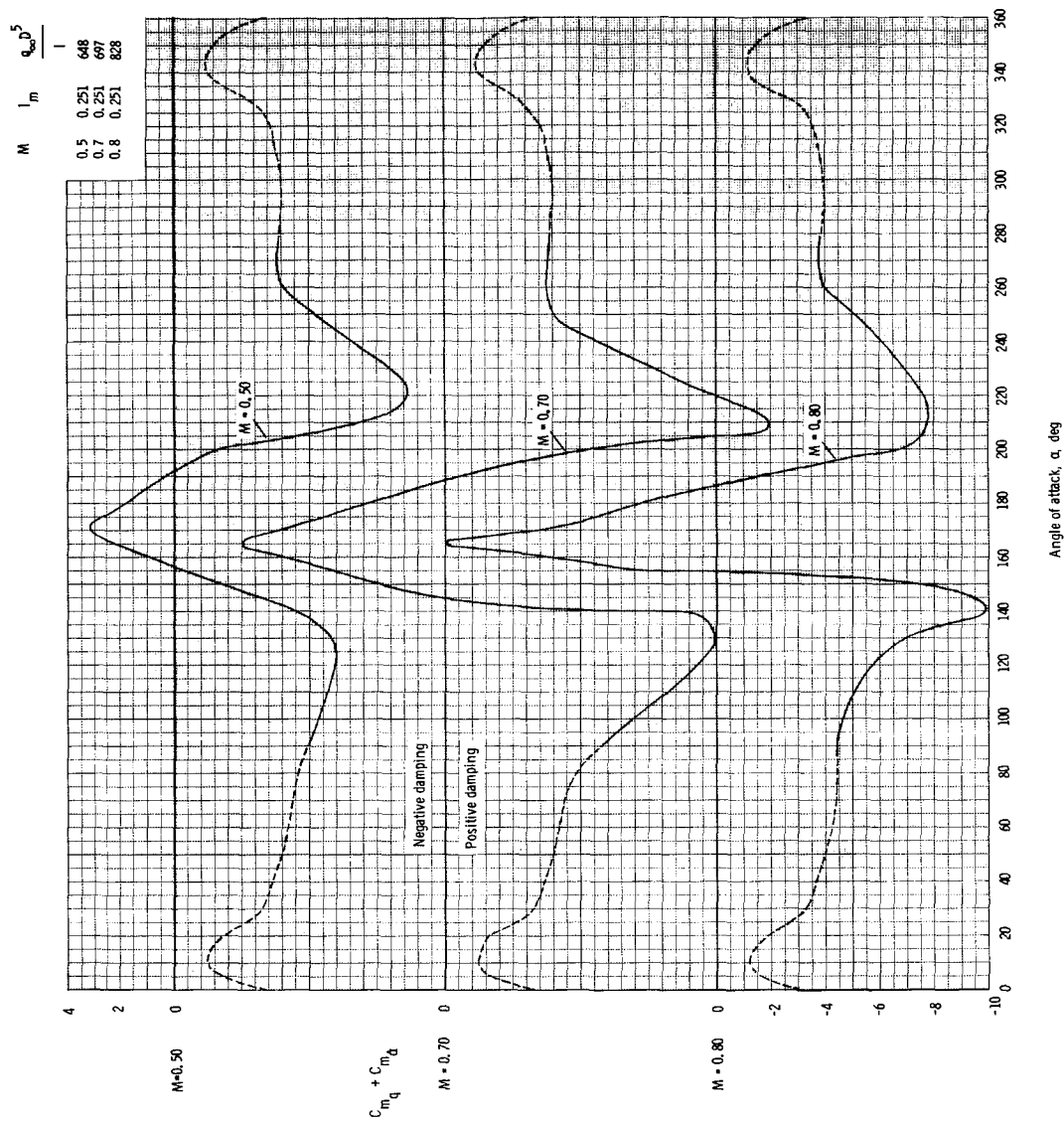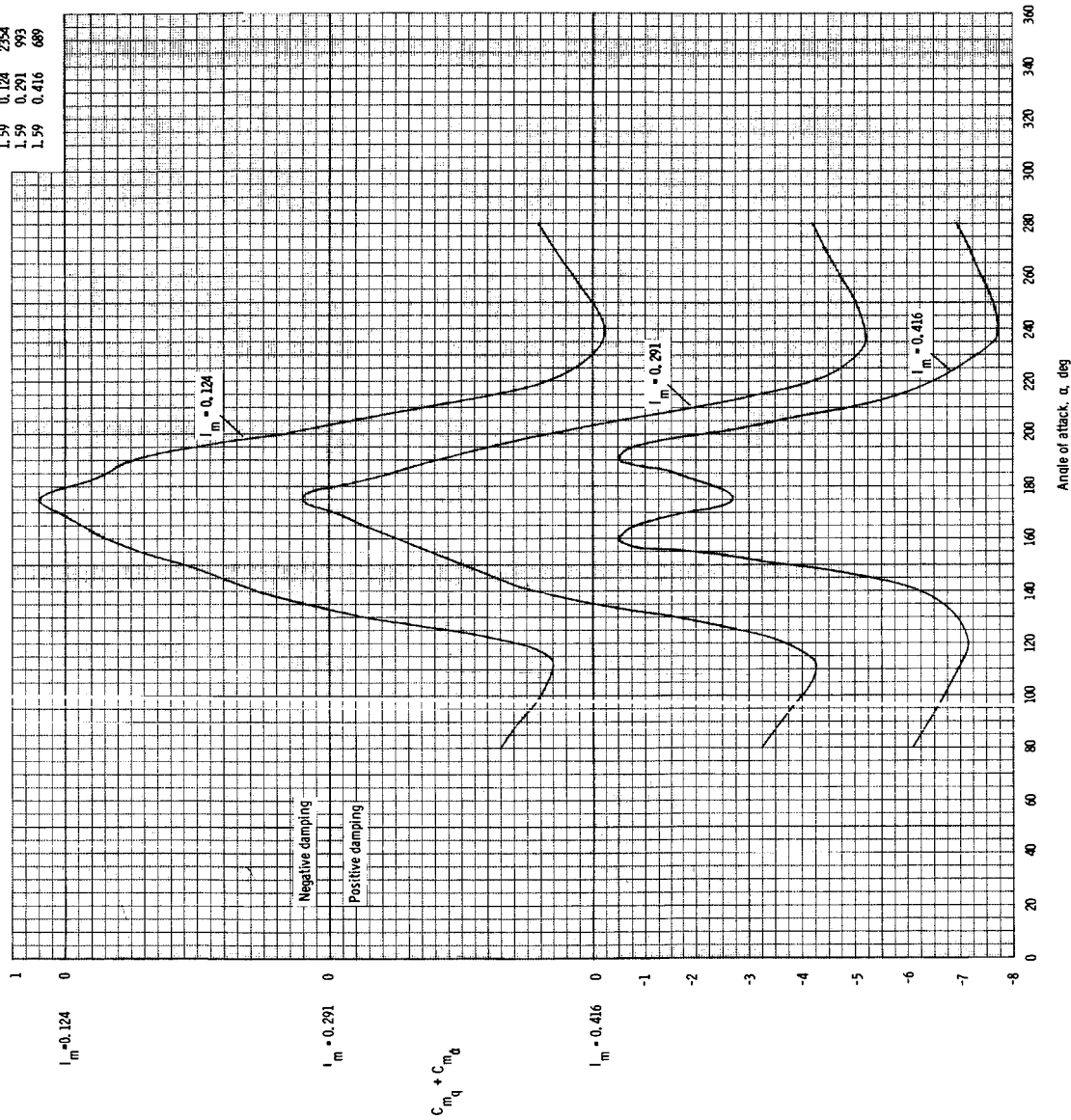
Figure 15. – Static pitching moment for the post-abort configuration, a comparison of data for sting-mounted and transverse-rod-mounted models.

95

(a) M = 0.50, 0.70, and 0.80, with model inertia of 0.251 slug-ft^2.

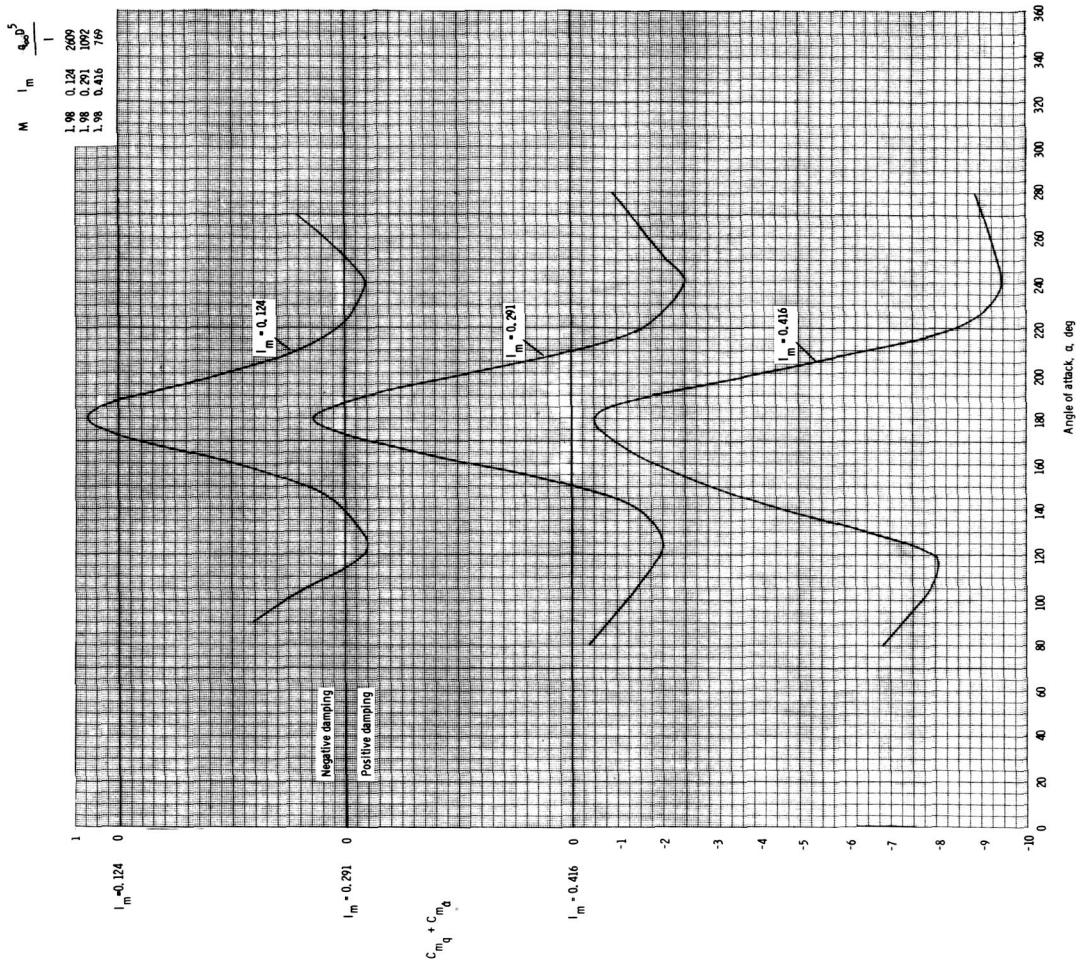Figure 16. - Dynamic stability derivatives for the post-abort configuration.

(b) $M = 1.59$, and model inertias of 0.124, 0.291, and 0.416 slug-ft^2.

Figure 16. -- Continued.

(c) M = 1.98, and model inertias of 0.124, 0.291, and 0.416 slug-ft^2.

Figure 16. - Concluded.